UC Berkeley
UC Berkeley Electronic Theses and Dissertations

Title
THE MECHANICS OF DYNEIN STEPPING AND DIRECTIONALITY

Permalink
https://escholarship.org/uc/item/5qf457d7

Author
Can, Sinan

Publication Date
2018

Peer reviewed|Thesis/dissertation

eScholarship.org Powered by the California Digital Library
University of California

THE MECHANICS OF DYNEIN STEPPING AND DIRECTIONALITY

By

Sinan Can

A dissertation submitted in partial satisfaction of the

requirements for the degree of

Doctor of Philosophy

in

Physics

in the

Graduate Division

of the

University of California, Berkeley

Committee in charge:

Professor Ahmet Yildiz, Chair

Professor Carlos Bustamante

Professor Eva Nogales

Fall 2018

ABSTRACT

THE MECHANICS OF DYNEIN STEPPING and DIRECTIONALITY

by

Sinan Can

Doctor of Philosophy in Physics

University of California, Berkeley

Professor Ahmet Yildiz, Chair

The ability of cytoskeletal motors to move unidirectionally along linear tracks is central to their cellular roles. While kinesin and myosin motor families have members that move in opposite directions, all dyneins studied to date exclusively move towards the microtubule minus-end. The source of dynein's directionality remains as the central unresolved question about the mechanism of its motility. In my doctoral work, I focused on understanding the underlying mechanism of dynein's directional motility along the microtubules in three dimensions. I used a protein engineering approach, guided by all-atom molecular dynamics simulations and high-resolution cryoEM imaging, along with the tools of single-molecule biophysics to dissect the elements of dynein motility. We successfully engineered a plus-end directed dynein for the first time and revealed the mechanism of its directionality. This work has three major outcomes. First, by altering the length of the coiled-coil stalk that connects the dynein motor domain to the microtubule, we controlled the handedness of the helical motility of dynein around the circumference of the microtubule. This experiment showed that the stalk length of native dynein is critical for restricting sideways movement and directing dynein motility along the microtubule axis. Second, we altered the angle and length of dynein's stalk. Remarkably, these modifications reversed the direction by which the linker swings relative to the microtubule and directed the motility towards the plus-end. Finally, similar to native dynein, the plus-end directed mutant maintains its preference to release from the microtubule when pulled towards the minus-end by an optical trap. Our results provide direct evidence for the linker swing model in which the direction the linker swings determines the direction of dynein motility. Our results also rule out the asymmetric release model that the directionality is proposed to be determined by the direction dynein favors for release from the microtubule under tension. Two critical features of dynein's stalk, the length of its antiparallel coiled-coils and two proline residues located at its base, control the directionality by directing the linker swing towards the MT minus-end. Because both features of the stalk are fully conserved in cytoplasmic and ciliary dyneins across species, this mechanism explains the minus-end directionality of all dyneins.

This dissertation is dedicated to my mother, Fevziye Can, who will remain as the most influential person in my life. She always inspires me with her kind heart, teary eyes, and unlimited support. She sacrificed her dreams so that her children can be happy in life.

Acknowledgments

I have learned to push my limits with the help of my high school teacher Hakan Oral in Istanbul. He always led me to achieve higher than I can dream of and taught me that I am the only limit. I learned to be patient and hardworking from him while trying to look at the bright side of the challenging situations and remain positive. His leadership turned to a friendship as I grow older, and his guidance helped dearly to become the person who I am today.

Academically, starting my Ph.D. at UC Berkeley is the greatest milestone in my career. As an international student, I was worried that I may fail to achieve what I aim. Joining the laboratory of Dr. Ahmet Yildiz provided me the environment that I can thrive academically. With Ahmet's guidance, I put myself on a path to become a scientist by asking the right questions and pushing limits of what is possible in terms of scientific techniques as well as my skills. That enabled me to learn many diverse techniques with clear applications that can answer challenging problems. I am very grateful to him for his scientific advising and personal encouragement. I am also very thankful to all the members of the Yildiz Lab, Jigar Bandaria, Vladislav Belyy, John Canty, Alex Chien, Frank Cleary, Mark Dewitt, Mohamed Elshenawy, Yasin Ezber, Luke Ferro, Amanda Jack, Emre Kusakci, Nicole Luk, Peiwu Qin, Sheng-Min Shih, SaraWichner. Among those, I specially thank Yavuz Dagdas, who was more than a colleague to me during my time at Berkeley and I believe he will stay as a lifelong friend.

My deepest thanks go out to my closest friend and loving wife, Sevtap Can. Her endless energy and optimism, constant support and love opened my eye to greater values in life. Her presence made my bad days bearable as we shared the joyful moments. I also thank my parents Fevziye and Metin Can, and my "best" sister Sinem and apologize to them for leaving my hometown so early. I always dream of the days we will spend together.

TABLE OF CONTENTS

Introduction

Cytoskeletal Motors

Eukaryotic cells are presented with the problems of intracellular organization, coordination, and locomotion. To overcome these challenges, cells utilize ATP-driven molecular motors, which transport intracellular components along cytoskeletal tracks. Motor proteins differ in the cytoskeletal track they bind, their directionality and the cargoes they carry. Apart from carrying enclosed organelles to specific locations in cells, some of these motors also apply forces on the filaments causing them to slide and create movement needed for muscle contraction, cell division and ciliary beating.

Different classes of motors have unique structural properties and mechanisms to create unidirectional motility, but the underlying principle is similar: ATP hydrolysis leads to track binding and release under different nucleotide state. This is coupled to conformational changes of a mechanical element of a motor in order to generate force and motility. Specifically, motors cycle among a minimum of four states: binding to the filament, conformational change that creates force, release from the filament, relaxation and rebinding to the filament. Consecutive cycling between these states produces motility and moves the associated cargo one-step a time. Usually, the track binding and motility are controlled by the motor domain and cargo binding is determined by the tail domain of the motor protein.

Cytoskeletal motors are divided into three protein families: Myosin family walks along the actin filaments whereas kinesin and dynein bind to microtubules (MTs). Myosin was the first identified motor protein for its role in muscle contraction. They form long filamentous structures and work in a group by pulling on the same actin filaments. Subsequently, dimeric myosin members were discovered that takes a role in actin-dependent cargo transport. All the myosins except one move towards the plus end of the actin filament[1,2].

Kinesin was first identified in the giant axon of the squid where it carries cargoes away from the cell body by walking towards the plus end of microtubules[3,4]. Kinesin superfamily has more than 15 different subclasses and humans have 40 different kinesin genes[5]. Most of the kinesin have an N-terminal motor domain and walk towards the plus end, except a unique kinesin family, kinesin-14 that has a C-terminal motor domain and walks in the opposite direction[6]. Kinesin and myosin families are structurally similar, indicating a common evolutionary origin.

Dyneins are a family of AAA+ motors responsible for nearly all minus-end directed motility[7] and force generation[8] functions along microtubules. Dyneins are evolutionarily distinct from myosins and kinesins, and are organized into two classes: Cytoplasmic dyneins are responsible for much of the minus-end directed transport of intracellular cargoes and axonemal dyneins produce the force required for ciliary motility. My doctoral work was mainly focused on cytoplasmic dynein, so in the following sections, I will focus mainly on cellular roles, mechanism of motility and force production of cytoplasmic dynein.

Cytoplasmic Dynein

Cellular Roles of Cytoplasmic Dynein

Cytoplasmic dynein (dynein hereafter) interacts with many intracellular pathways.

a. In interphase cells, dynein carries membrane-bound organelles towards the minus-end. Examples of organelles trafficked by dynein include endosomes[9], lysosomes[10], phagosomes[11], melanosomes[12], peroxisomes[13], lipid droplets[14], mitochondria[15] and vesicles from the endoplasmic reticulum[16]. Furthermore, viruses[17], transcription factors[18], aggregated proteins[19], and mRNA containing particles[20] towards the nucleus can be carried by the dynein-dependent transport machinery

b. In neurons, dynein is required for neuronal migration[21], growth[22], and synapse formation[23] and drives retrograde transport towards the cell body[7, 24]. The defects in the dynein motility are linked with degeneration[25] and sensory neuropathy[26] in motor neurons, ALS[27], Alzheimer's disease, lissencephaly, and schizophrenia[28]

c. Dynein also plays important roles in cell division, including orienting astral MTs at the cell cortex[29, 30], maintaining the proper tension and length of the spindle[31-33], focusing the minus ends of MTs into poles[34-36], and regulating the spindle assembly checkpoint activation and appropriate segregation of chromosomes[37, 38].

Architecture of Dynein

The dynein complex (1.5 MDa) is composed of two identical dynein heavy chains and several smaller associated polypeptides[39] (Figure 1). Each dynein monomer contains a C-terminal motor domain and an N-terminal tail domain. Head consists of a catalytically active ring and a microtubule-binding domain (MTBD) that is separated from the catalytic ring by a 10 nm long stalk, an antiparallel coiled-coil. Head has six AAA+ modules (AAA1-6) that form a ring (15nm diameter). Unlike the other AAA proteins, all of the AAA subunits are concatenated into a single polypeptide chain. Only AAA1-4 has a nucleotide-binding motif. AAA1 is responsible for binding and hydrolyzing ATP to power motility[40, 41] and AAA3 functions as a switch to regulate dynein motility and force generation cycle[42-44]. AAA5-6 have only structural roles for the motility such that ATP dependent conformational changes in the linker and ring are translated into motility. The tail domain is involved in dimerization of the heavy chains and contacts the AAA+ domains through a linker region[45-47]. The tail also binds a light intermediate chain (LIC) and an intermediate chain (IC) that is complexed with three light chains (LCs: LC7, LC8 a Tctex)[8, 48, 49].

Surprisingly, in animal cells, a single dynein functions in the cytoplasm, compared to 40 kinesins that perform related function on MTs. This suggests that dynein is repurposed for many of the cellular roles by associated proteins. Indeed, recent studies identified many cargo adaptor proteins that link dynein to its target, either vesicles for cargo transport along microtubules or membrane for microtubule pulling during cell division. These proteins such as BICD2, NUMA, Hook3 and BICDR contain a long coiled-coil domain that is essential for complexing dynein with dynactin and required for the motility of mammalian dynein/dynactin complex. This is in contrast to dynein

from *S. cerevisiae*, which is constitutively active and does not require complex formation for motility, presumably because yeast dynein has a singular function in segregation of nuclei during cell division.

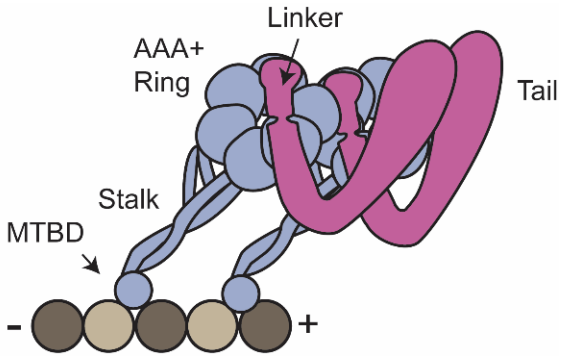

Figure 1: Overview of dynein structure. *The catalytic AAA+ ring is connected to MTBD by an anti-parallel coiled-coil stalk. The linker resides on the face of the AAA+ ring and tail domain is responsible for dimerization and mediating cargo binding*

The Mechanochemical Cycle of Dynein

Within an ATP hydrolysis cycle, an individual head of a typical motor **(1)** binds strongly to their track, **(2)** produces a force-generating conformational change (powerstroke), **(3)** releases from its track, **(4)** performs a recovery stroke and **(5)** rebinds in a specific direction, resulting in unidirectional movement (Figure 2). The AAA+ ring of a dynein monomer lies parallel to the MT and the stalk is tilted towards the plus-end at its base. In the absence of a nucleotide (apo) at AAA1, dynein is tightly bound to MTs and the linker has a straight post-powerstroke conformation, exiting the ring at AAA4. ATP binding to AAA1[50] (yellow) triggers MT release through a shift in the registry of a coiled-coil stalk[40, 51] and the linker undergoes the priming stroke[46, 47, 52]. At this pre-powerstroke conformation, the linker is bent by a flexible hinge towards the middle of the ring and exits the ring at AAA2. Linker swing is aligned with the MT long-axis and moves the MTBD towards the minus-end. After ATP hydrolysis, the dynein head re-binds to MT and releases the inorganic phosphate (Pi). In the ADP bound state, the linker undergoes a force generating powerstroke[53] by moving back to its straight conformation[46, 47, 52]. This pulls the cargo towards the minus end (black arrow). After ADP release, dynein returns back to the apo state for the next cycle.

The Stepping Mechanism of Dynein

Single molecule tracking methods provide enough spatial and temporal resolution to detect individual steps taken by motor proteins. Fluorescent imaging and optical trapping techniques were used to understand the stepping characteristics of individual heads such as the step size and the stepping pattern. The step sizes are expected to follow the periodicity of the filaments and can be measured by labeling of individual heads with fluorescent molecules. Collection of enough photons can result in a nanometer resolution to distinguish individual steps along the filament. Kinesin is shown to take 8 nm steps with a highly regulated pattern where almost exclusively the rear head takes a step forward with few backward and sideways stepping. During my doctoral work, I have shown that one way of ensuring that pattern is based on a “gating” between heads

where only the rear head can bind to ATP and takes a step forward. This will be presented in the last part of this thesis.

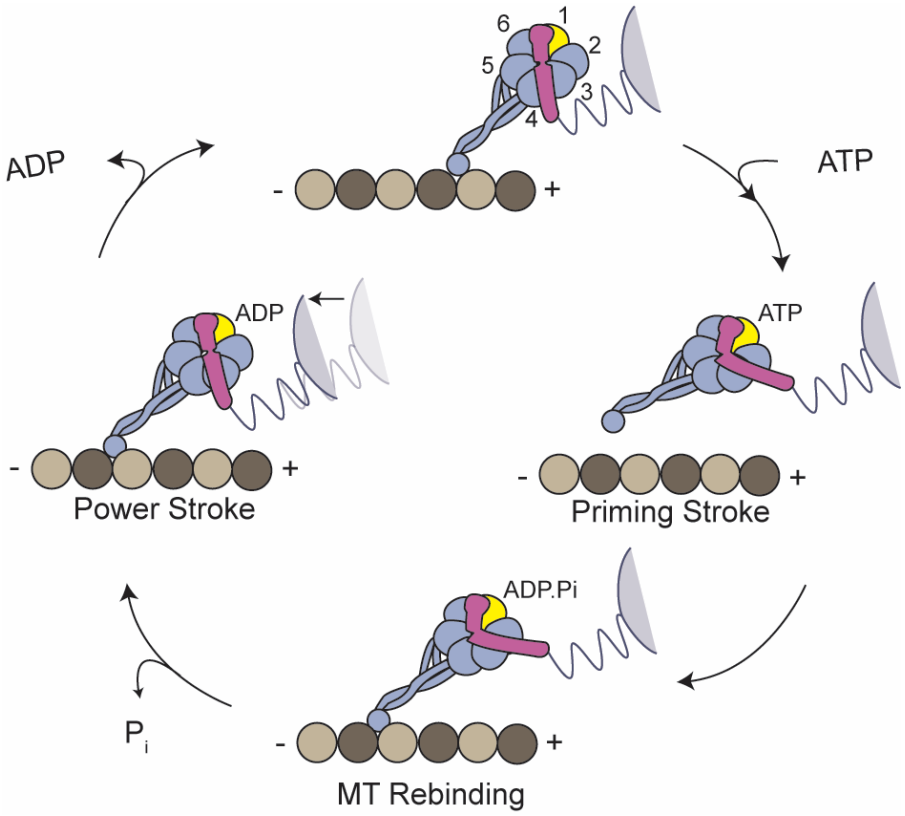

Figure 2: Dynein's mechanochemical cycle

Recent studies on the motility of *S. cerevisiae* and *Dictyostelium* dynein[51] revealed how a dynein dimer moves along MTs. Two-color fluorescent imaging studies where each head is labeled with a different color showed that unlike kinesin[54] and myosin[55, 56], in which the heads are coordinated[57-59] to walk hand-over-hand[54, 60, 61], dynein moves processively by uncoordinated stepping of its two heads[62, 63]. In other words, each head of the dynein is able to release from MT and move forward on its own, while the partner head serves as a tether to prevent dissociation from the track. Only one active head is enough for the motility further suggesting that each head can move independently from its partner. Dynein advances most frequently in 8 nm steps, although longer as well as sideways and backward steps are observed[64]. The stepping pattern of mammalian dynein complex with adapter proteins is still not studied to date. It is possible that the adapter proteins control the stepping characteristics by changing the step size, rate and percent of backward stepping during dynein motility.

Force Generation of Dynein

The mechanism of dynein's force generation and response to external load has been studied using single-beam optical tweezers. In these assays, micron-sized polystyrene beads are sparsely coated

with dynein motors, trapped with a focused laser beam and positioned over a surface-immobilized microtubule. When dynein starts walking along a microtubule, it carries the bead away from the trap center until a restoring force applied by the trap (increases by displacement of the bead) stalls dynein movement. These fixed-trap assays are frequently used to measure the maximal force generation of single motors. Under the force-clamp mode, motor stepping is tracked at nanometer precision under average external force applied by the trap.

Optical trapping studies of yeast cytoplasmic dynein showed that a full-length dynein stalls at ~3.5 pN load [65] and persists at the stalling position for up to a minute [65, 66], much longer than the stall time of kinesin-1 [67]. On the other hand, mammalian dynein alone can only produce ~2 pN force, mainly because it is not a constitutively active protein without the adapter proteins. Addition of BICD2 and dynactin activates the complex and increases force production to ~4.3 pN[68].

Interestingly, the motor can be forced to walk backward either in the presence or absence of ATP [65, 66]. The force-velocity relationship of dynein indicated that the backward stepping rate of dynein is insensitive to force while the forward stepping rate increases with force in the forward direction [65]. This is opposite to myosin V where increasing the hindering force increases its backward stepping [69].

DNA-tethered bead assays [70] were used to study the force generation of a single head in the context of a walking dynein dimer. These assays suggested that the two heads of a dynein dimer share the load, each producing ~1.5 pN load. Therefore, dynein can be modeled as two elastically linked monomers [65], rather than a cyclic machine, such as kinesin-1. Majority of the force is being produced in the microtubule-bound state [65], consistent with the powerstroke model [52]. The priming stroke of the linker of unbound head stalls at 0.5 pN load, suggesting that this conformational change may provide a weak bias towards the minus end for the stepping head [65].

Directional Movement Towards the Microtubule Minus End

The ability of cytoskeletal motors to move unidirectionally along linear tracks is central to their cellular roles. While kinesin and myosin motor families have members that move in opposite directions, all dyneins studied to date exclusively move towards the microtubule minus-end. The source of dynein's directionality remains as the central unresolved question about the mechanism of its motility. There are two current models. Structural studies proposed that ATP-dependent swinging motion of the linker domain moves the stepping head towards the minus end[52, 71, 72]. According to this model, a conformational change that moves the head towards the minus head after it is released from the MT. This is consistent with the uncoordinated stepping of the heads, which showed that each head can move forward independent of the other[62, 63]. In order for this model to work, the head must be relatively rigid in the microtubule unbound state, so that the priming stroke can move the MTBD towards the minus end.

The asymmetric release model proposes that faster release of dynein when pulled towards the minus-end[66, 73, 74] creates a net bias in minus-end directionality. Consistent with this model, an engineering study[75] that replaced dynein's MTBD with actin-binding proteins. In these studies, the chimeric motors move processively along actin filaments and direction of motility can be reversed by altering the asymmetric release property of the actin-binding proteins. These studies suggested

that unidirectional motility does not require pointing of the priming stroke towards the minus-end but the chimeras can work as a directional ratchet.

The source of dynein's directionality remains as the central unresolved question about the mechanism of its motility. During my doctoral work, I successfully engineered a plus-end-directed dynein for the first time and revealed the mechanism of its directionality by using protein engineering, molecular dynamics/modeling, cryoEM, and single-molecule imaging and force spectroscopy. This work also presents an effective strategy to manipulate the mechanics and directionality of dynein motility, which provide unique advantages in the design of new molecular machines for future applications in biotechnology.

Single Molecule Biophysics Approaches to Study Motor Proteins

Studies of molecular motors have been greatly aided by the advancement of single molecule imaging and manipulation techniques. Traditional bulk biochemistry assays average the readout from large number molecules and are not applicable to measure the translocation and force production of molecular motors. In comparison, single molecule techniques are ideally suited to monitor the activity of individual motors in real time at nanometer and piconewton sensitivity to probe the molecular architecture, conformational dynamics, stepping, force generation and function of these motors (Figure 3). During my Ph.D., I utilized two major techniques to study dynein mechanism in vitro: Single fluorescent particle tracking and optical trapping.

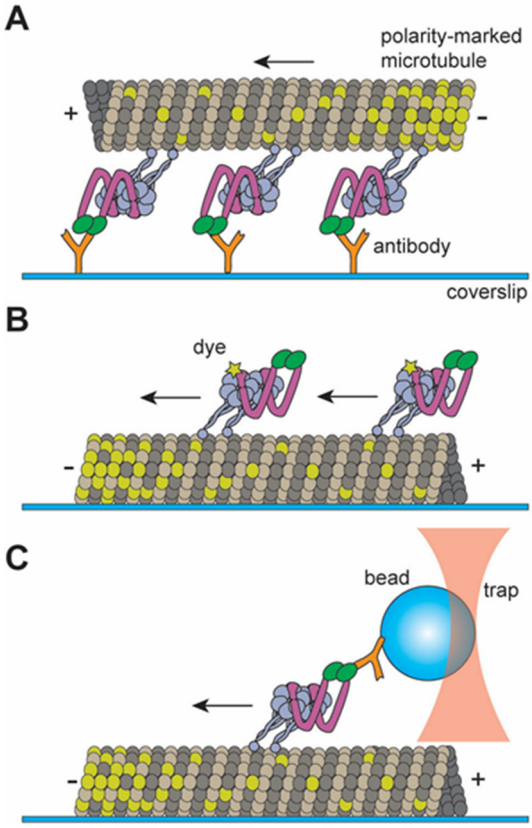

Figure 3: Single molecule techniques to study dynein motility. *a) MT gliding assay: Dynein molecules are immobilized to a coverglass through their tail. Polarity marked MTs were used to determine the*

direction of motility. b) Single molecule motility assay: Motility of single fluorescently-labeled motors can be studied on surface immobilized MTs. c) Optical tweezers: Polystyrene beads are sparsely coated with a motor and trapped with a focused laser beam. Optical trap is used to measure the force production of single molecules, and to determine microtubule release rate and the step size of motors under constant forces.

Single Molecule Fluorescent Imaging

Fluorescence imaging provides sensitivity required to image single molecules due to the spectral shift in emitted light in comparison to the excitation light. Organic dyes are ideal to study motor proteins due to the site-specific labeling, high signal to noise ratio and their small size. Early versions of organic dyes were not either stable or bright enough for high resolution studies of motor stepping. With the development of brighter and more photostable fluorophores, advanced imaging methods, and sensitive cameras, single molecule studies of motors advanced significantly over the past two decades.

The most commonly used imaging technique for motors is total internal reflection fluorescent TIRF) microscopy. In this method, excitation light is total internally reflected at the glass/water interface. This generates an evanescent field at the coverslip surface that decays within 100 nm depth of solution. The evanescent field is used to excite the fluorophores near the surface, while eliminating the signal from Raman scattering of water and freely floating fluorescent molecules in the solution. TIRF is ideal for single molecule motility assays, because MTs can be immobilized at the glass surface and motility of single fluorescently-labeled proteins can be detected at near-optimum sensitivity.

Single particle tracking reveals the directionality, velocity, run length and landing rate of motors on MTs. For these experiments, linear density of the motors on a MT must be reduced to less than one molecule per μm, because the resolution of conventional light microscopy is limited by the fundamental limit of diffraction. Particles that are smaller than $\lambda/2NA$ (λ is the wavelength of used light and NA is the numerical aperture of the objective) are seen as the diffraction limited spot. For visible light, this corresponds to a spot 200-300 nm in full width at half maximum. Because the size of the diffraction limited spot is much larger than the actual size of a motor (8-40 nm), this limit causes an overlap between adjacent motors at high densities and these motors cannot be readily resolved by conventional methods.

Although diffraction limit is a major challenge for resolution of multiple light emitting objects, position of a single fluorescent object can be determined by arbitrarily high precision. In an aberration-free imaging system, center of the diffraction limited spot represents the position of a dye. The center can be determined by calculating the centroid or fitting the spot to a two-dimensional Gaussian. Error in localization can be reduced by collecting more photons in a given frame. The error corresponds to the standard error of the mean ($\sigma/\sqrt{N}$, σ is the standard deviation of the Gaussian, or one half of the spot diameter, N is the number of photons collected) to localize the center of the Gaussian fit to the collected light. For a visible light, this corresponds to ~10^4 photons to achieve 1 nm precision. Advancements in the organic dyes and recently synthesized quantum dots can emit enough photons at that localization precision for hundreds of frames before they photobleach and this allows precise tracking of motors to study their stepping behavior.

Another critical limitation for the step detection is the temporal resolution. Motor proteins can move as fast as 10 μm/s. Even though EM-CCD or CMOS cameras can collect a full frame at 1 ms temporal resolution, the collected photon count per frame reduces as the frame rate is increased. As a result, the signal from a fluorophore limits the temporal resolution. This challenge can be addressed by slowing down the motor in limiting ATP concentration such that multiple frames at nanometer precision can be collected between consecutive steps of a motor.

Optical Trapping

Molecular motors carry large cargos and pull on microtubules and organelles in order to perform their cellular function. Some of the cellular functions require the ability of the motors to produce large forces and work under tension. Single molecule manipulation techniques have been successfully implemented to measure force generation of single motors, and tension affects their velocity, stepping and directionality. One of the most commonly used manipulation methods is optical trapping, which measures piconewton forces and nanometer-scale displacements that molecular motors generate along their associated filaments at millisecond resolution. Optical tweezers also have the capability to apply calibrated forces to specific domains of a motor and put different geometrical constraints on a motor's conformation for a deeper understanding of its mode of action.

Optical trapping is achieved by focusing a powerful infrared beam on glass or latex beads. These beads are sparsely coated with a protein of interest using antibody-antigen or biotin-streptavidin linkage. Specifically, there are two regimes that trapping can be achieved. If the trapped object size is comparable to the wavelength of the focused light, it acts as a lens such that change in the momentum of the light exerts a force on the object. If the object is smaller than the wavelength of the trapping beam, dipole effects come into play. By changing the position of the laser beam, the position of the bead can be controlled.

The force applied to the system acts as a Hookean spring, $F = -kx$ within the linear range of the trap (typically ±150 nm away from the trap center). The trap stiffness (k) can be controlled by the size of the bead or the laser power. To measure forces between 0.5-25 pN, we typically use beads of sizes around 0.5-2 μm diameter and trap these beads using 10-50 mW 1,064 nm focused laser beam.

Optical trapping can be utilized in several ways to study the mechanism of force production. The fixed trap assay is used to measure the stall forces of motor proteins. In this assay, the trap is held stationary as the motor walks along the surface-immobilized filament. Resistive force by the trap increases linearly as the motor moves the bead away from the trap center. The stall force is defined once the protein reaches the maximum distance that it can walk under the resistive pull of the trap. This is determined to measure the maximum work a motor can generate during its motility.

Force-feedback controlled assays are used to study how load affects the motility and mechanics of motor proteins. In this assay, the trap position is updated fast enough so that the distance between bead and trap positions stay constant, causing the motor to walk under constant force. This method allows us to study the direction, velocity and stepping of motors under a wide range of forces applied in assistive and resistive directions.

Another common usage of optical trapping is to measure the force-dependent release rate of motors from the filaments. Especially for the cellular roles of motors that require large forces or long tracking distances, it is critical to stay bound to the filament. Furthermore, motors may act as a ratchet against thermal fluctuations if the release is asymmetric, that is releasing faster towards one side of the filament compared to the other. In this assay, beads are sparsely coated with a monomeric motor and brought near a surface immobilized MT using optical trap. The trap is oscillated back and forth between two positions on a MT in a square wave pattern. The bead normally follows the trap when it does not interact with a MT. However, when a single motor on the bead binds to a MT, the bead is unable to follow the trap to the next position due to the bound motor. In this state, the trap exerts a constant force on the motor until the motor releases from the MT. The bead-trap separation reveals the direction and magnitude of applied force and duration at which motor stays bound to a MT reveals the release rate at a given magnitude and direction of force. This assay directly measures the release rate of a head over a large range of forces (0.5-12 pN) exerted toward either end of MT.

Bidirectional Motility of Cytoplasmic Dynein Around Microtubules

The work presented in this chapter was published in the following paper: Bidirectional helical motion of cytoplasmic dynein around microtubules written by Sinan Can, Mark A. Dewitt and Ahmet Yildiz. ***eLife*** (2014)

Abstract

Cytoplasmic dynein is a molecular motor responsible for minus-end-directed cargo transport along microtubules (MTs). Dynein motility has previously been studied on surface-immobilized MTs in vitro, which constrains the motors to move in two dimensions. In this study, we explored dynein motility in three dimensions using an MT bridge assay. We found that dynein moves in a helical trajectory around the MT, demonstrating that it generates torque during cargo transport. Unlike other cytoskeletal motors that produce torque in a specific direction, dynein generates torque in either direction, resulting in bidirectional helical motility. Dynein has a net preference to move along a right-handed helical path, suggesting that the heads tend to bind to the closest tubulin binding site in the forward direction when taking sideways steps. This bidirectional helical motility may allow dynein to avoid roadblocks in dense cytoplasmic environments during cargo transport.

Introduction

Cytoskeletal motors transport a wide variety of intracellular cargos by processively moving along linear tracks. These motors do not always follow a linear trajectory. Rather, they generate torque perpendicular to their direction of motion, resulting in helical movement relative to the filament. Such helical motion was first observed in a filament gliding assay in which surface-immobilized *Tetrahymena* axonemal dynein motors rotated MTs about their principal axes while translocating them [76]. Helical movement of cargoes has subsequently been demonstrated for several members of the myosin and kinesin superfamilies[77-81].

Cytoplasmic dynein is the primary MT minus-end directed motor responsible for diverse cellular processes in cargo transport, nuclear positioning and cell division[82]. Despite its importance, key aspects of dynein's mechanism remain unclear, including whether or not the motor can produce torque. In contrast to kinesin-1, which follows a single protofilament track[83, 84], dynein takes frequent sideways steps [64]. However, the full trajectory of dynein motors in three dimensions (3D) remains unknown, because the motors are sterically prevented from moving around the circumference of surface-immobilized MTs.

Results

To track dynein motility in 3D, we constructed MT "bridges" [80] (Figure 4a), which allow unconstrained motion between the protofilaments. The bridges were constructed by suspending a tetramethylrhodamine (TMR)-labeled MT between two large (2 μm diameter) polystyrene beads, immobilized on the surface. These beads were densely coated with a chimeric protein containing the dynein MT binding domain (MTBD) that stably binds to MTs [72, 85]. Multiple dynein motors

were linked to a 0.5 µm diameter bead (referred to as cargo) and were brought in the proximity of the MT bridge with an optical trap. When the motors bound to the MT, the cargo bead was released from the trap and its motion recorded with bright-field microscopy (Figure 4b). The *xy* position of

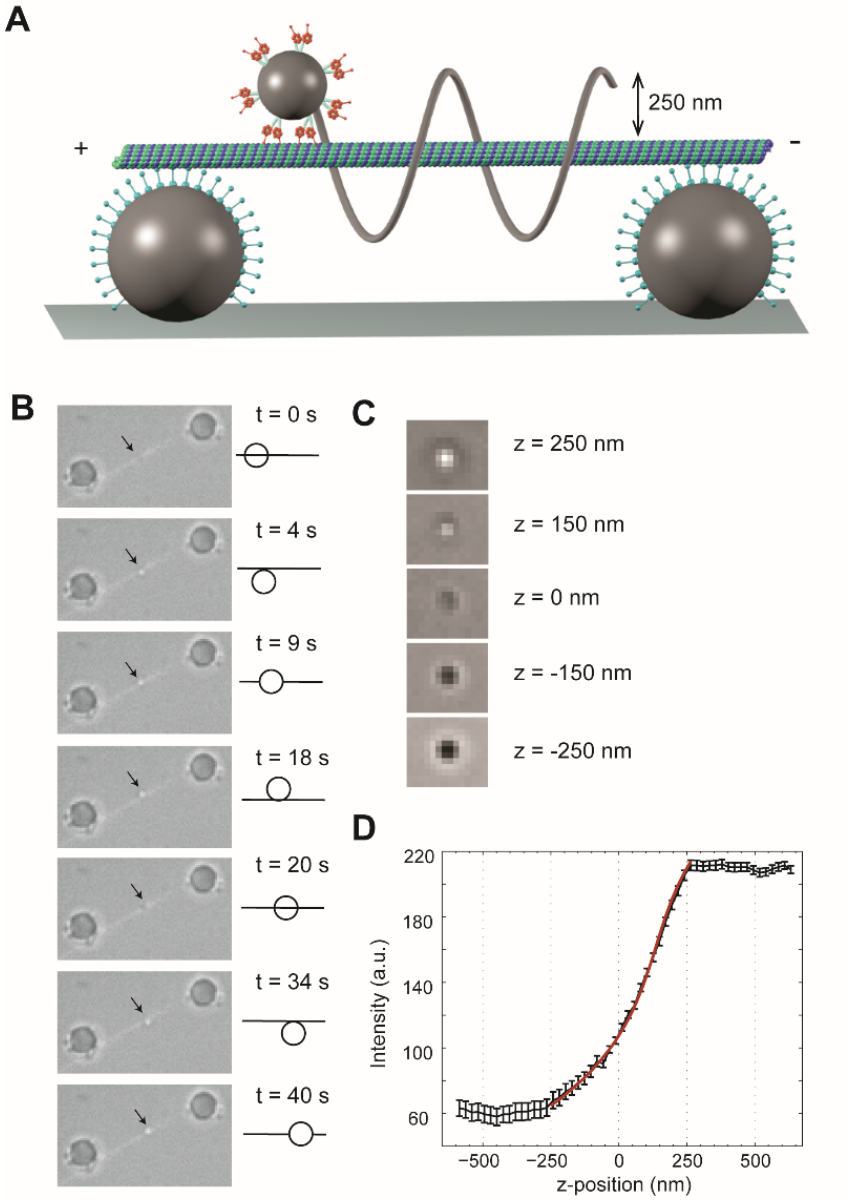

Figure 4: 3D tracking of dynein-driven transport along MT. *(**A**) Schematic representation of the experimental geometry (not to scale). The MT suspended bridge is formed by attaching an MT (green) to the surface-immobilized beads (gray) that are coated with a chimeric protein containing the dynein MTBD. A 0.5 µm diameter cargo bead is coated with multiple dynein motors and trapped by a focused laser beam (not shown) for placement of the bead on the bridge. The bead center is expected to be separated by ~250 nm from the MT. (**B**) Movement of a GST-Dyn$_{331kD}$ coated bead along an MT bridge (left). The fluorescent image of the MTs has been superimposed onto the bright-field images. The bead moves in a left-handed helical manner along the MT. The schematic on the right represents the side view for the orientation of the bead relative to the MT. (**C**) Bright-field image of the cargo-bead in different z positions shows that the z position of the bead relative to MT can be determined by its appearance. Images are taken at z = -250nm,*

*-150nm, 0nm, +150nm, +250nm. (**D**) The averaged intensity of a 0.5 µm diameter bead under a brightfield illumination at variable z positions. The averaged intensity from 20 beads increases as the bead is moved from -250 nm to +250 nm in the z-direction relative to the image plane. The red curve represents a fit to a third order polynomial (R^2 =0.998). The z position of a motor-coated bead was calculated from the calibration curve. Error bars represent SEM.*

the cargo was determined by a two-dimensional Gaussian tracking algorithm. The *z* position was determined by changes in the intensity of the bead center, allowing us to track bead movement in 3D (Figure 4c,d, Figure 5).

We initially tested the robustness of our experimental geometry using human kinesin-1 motors, which follow a single protofilament [83, 84]. Because the handedness of the MTs varies based on the number (11-14) of protofilament tracks [86], we polymerized tubulin with a non-hydrolyzable GTP analog (GMP-CPP). 96% of GMP-CPP MTs are made of 14 protofilaments and have a left-handed supertwist with 6,400 ± 1,000 nm pitch [86]. The average velocity of kinesin-driven beads was 541 ± 23 nm/s (mean ± SEM, N =10), comparable to the speed of single motors [59]. We observed that kinesin-1 coated beads traveled along GMP-CPP MTs with a left-handed helical motion with a pitch of 6,500 ± 400 nm (mean ± SEM, N = 6) similar to the helicity of 14 protofilament MTs. The results are also consistent with the reported values of kinesin-1movement on GMP-CPP MTs (5,700 – 7,900 nm pitch, left-handed) using alternative geometries [80, 87].

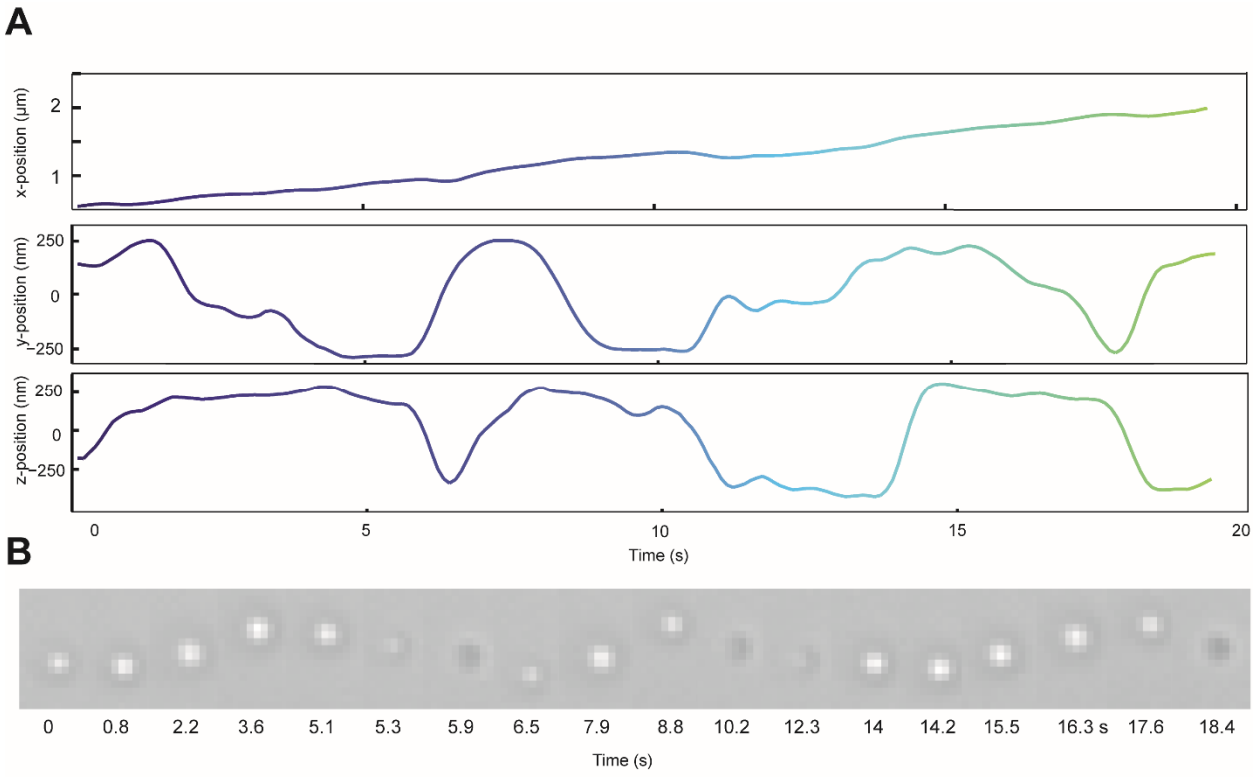

Figure 5: Movement of a GST-Dyn$_{331kD}$ coated bead along an MT bridge. *(**A**) First 20 seconds of the 3D trace for dynein motility along MT plotted in x, y and z directions as a function of time. (**B**) The brightfield image of the bead shows the changes in the position and intensity of the bead as a function of time.*

Helical Movement of Dynein Dimers

We next investigated the helical motility of cytoplasmic dynein. We used a tail-truncated yeast dynein artificially dimerized with glutathione S-transferase (GST-Dyn$_{331kD}$), which has similar motile properties to full-length dynein [64]. The motors were fused to GFP at the N-terminus and attached to cargo beads coated with anti-GFP antibodies. At 1 mM ATP, dynein-coated beads moved in helical trajectories with a pitch of 591 ± 32 nm (mean ± SEM, 67 rotations, 15 beads, Figure 6a,b,c). This rotation corresponds to a sideways movement to a neighboring protofilament (6 nm) for every 5 tubulin dimers (48 nm) in the forward direction. Unlike axonemal dynein and kinesin motors, which primarily rotate along their tracks in only one direction [76, 80], beads coated with cytoplasmic dynein exhibited both left- and right-handed helical movement on MTs (N = 67 rotations, Figure 6a,b,c) The speeds of left- and right-handed movements along the helical path (79 ± 4.7 nm/s and 89 ± 17 nm/s, mean ± SEM, respectively) were statistically indistinguishable (t-test, p = 0.28). Bidirectional helical movement was also evident from traces of single beads, which occasionally switch direction during a run (4 out of 67 rotations, Figure 6d). In contrast, reversal of bead motility along the MT axis was never observed.

We next investigated the helical motility of a full-length yeast cytoplasmic dynein [64]**.** The motors were fused to GFP at the N-terminus and attached to cargo beads coated with anti-GFP antibodies. Dynein-coated beads moved in helical trajectories with a pitch of 500 ± 36 nm (mean ± SEM) and exhibited both left- and right-handed helical movement. The speeds of left- and right-handed movements along the helical path (42 ± 11 nm/s and 43 ± 10 nm/s, mean ± SEM, respectively) were statistically indistinguishable (t-test, p = 0.21). Similar to GST-Dyn$_{331kD}$, beads driven by full-length dynein occasionally switch direction during a run (8 out of 33 rotations). Unlike GST-Dyn$_{331kD}$, which has a net preference for left-handed helical movement (75%), full-length dynein has a net preference for right-handed helical movement (58%, t-test, p = 10^{-5}). This difference may be related to GST dimerization, in which the heads are oriented differently relative to the MT surface.

The pitch of dynein rotation is much shorter than the supertwist of the GMP-CPP MTs (~6,400 nm), suggesting that helical motility of dynein is independent from the helicity of the MT track. To verify this, we repeated the assay with GST-Dyn$_{331kD}$ on taxol-stabilized MTs, which contain a mixture of 12 (77%) and 13 (11%) and 14 (2%) protofilaments [83]. Out of 34 rotations, 68% were left handed and 32% were right-handed. On average, the pitch of helical movement was 607 ± 50 nm (mean ± SEM) similar to that of GMP-CPP MTs (t-test, p = 0.77). The results demonstrate that our findings are not an artifact of the MT polymerization method.

To test the possibility that bidirectional rotation can be driven by a rotational tug-of-war between dynein motors (i.e. some motors strictly rotate in a right-handed helix and the others rotate in the opposite direction), we tracked individual GST-Dyn$_{331kD}$ motors labeled with a quantum-dot on MT bridges (Figure 7). The average run length of single motors on MT bridges was 1.5 ± 0.7 μm (mean ± SD, N= 10), which is similar to that measured on surface-immobilized MTs [64]. The velocity of single dimers was 64 ± 8 nm/s (mean ± SEM N = 10), similar (t-test p= 0.12) to that of cargo beads carried by multiple dimers (80 ± 10 nm/s, N = 15). The traces of single motors show high variability along the perpendicular axis of MTs and switch directions in their sideways

movement more frequently than the beads carried by multiple motors (Figure 7). These results excluded rotational tug-of-war.

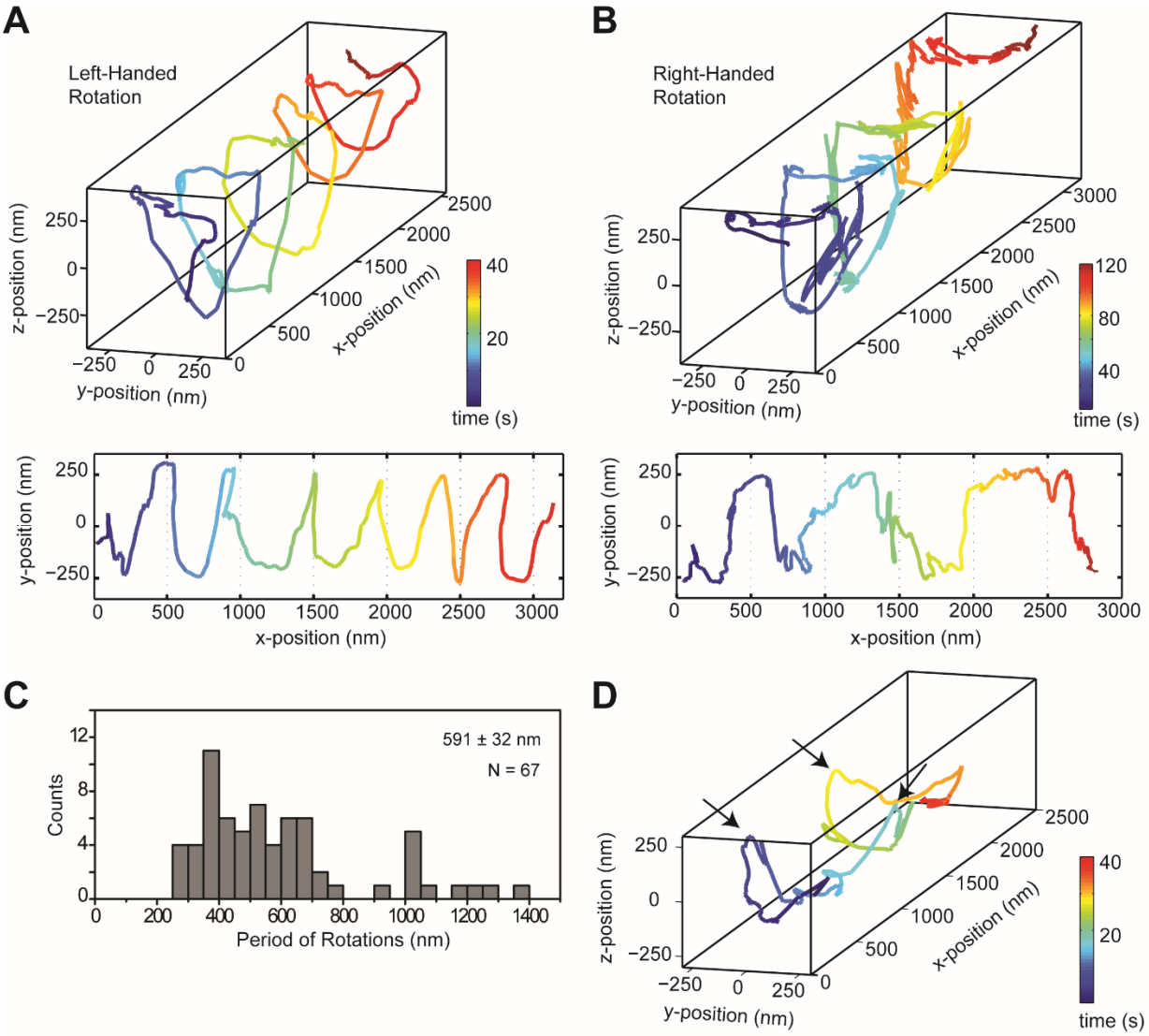

Figure 6: Dynein moves in both left- and right-handed helical paths along MT bridges. *(**A-B**) (Top) Representative three-dimensional trace of a cargo bead driven by GST-Dyn$_{331kD}$ motors shows left- (A) and right-handed (B) helical motion. (Bottom) Two-dimensional projections of the traces shown at the top. (**C**) Histogram of observed pitches per complete rotation. The average pitch is 591 ± 32 nm (mean ± SEM). The average pitch of the left-handed movement (546 ± 42 nm, SEM, N = 32) was shorter (t-test, p = 0.01) than that of the right-handed movement (749 ± 81 nm, SEM, N = 10). (**D**) Change in handedness of rotation during the transport of a cargo bead. An example trace shows that a cargo bead initially moves along GMP-CPP MTs with a right-handed helical motion. At around t = 10 s, the bead reverses its helical motion for half of the period. At t = 20 s, the bead switches back to right-handed rotation and takes another half turn around the MT. Finally, at t = 25 s, the bead resumes left-handed helical motion until it disassociates from the MT. Arrows show the transitions from one type of helical motion to the other.*

Helical Movement of Dynein Monomers

We next tested the possibility that the relative orientation of the two motor domains in a dimer can influence the handedness of helical motion. To eliminate the contribution of interhead orientation, we used a cargo bead coated with monomeric Dyn331kD, which is not processive on its own [64]. We observed that multiple monomers were able to drive processive motility of cargo beads at 61 ± 6 nm/s (mean ± SEM), consistent with the ability of multiple non-processive kinesins or myosins to drive processive motility [88, 89].

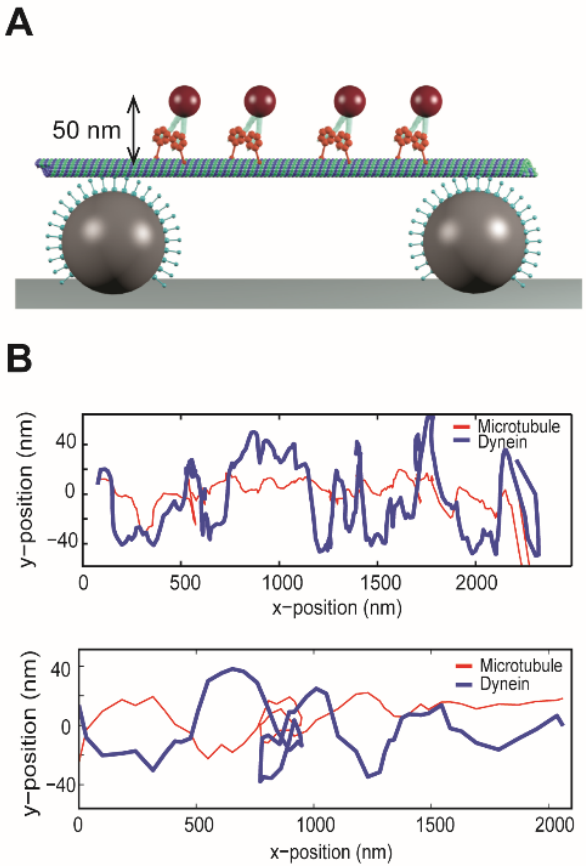

Figure 7: Single dynein motors show high variability and frequent switches direction of their sideways movement. *(A) Schematic representation of quantum-dot labeled single dynein motors on the MT bridges (not to scale). The expected amplitude of rotations is ~50 nm. (B) Two example traces show a 2D projection of dynein motors along the MT, using fluorescent tracking. MT filaments remain nearly straight between the bridges (persistence length is 5.2 mm) and oscillate due to the thermal fluctuation. The red trace represents ±35 nm fluctuation of the MT bridge in the perpendicular axis, determined by the position of a quantum dot stably bound to MT. The red trace was subtracted from the traces of quantum dots attached to single dynein motors (blue trace). Single motors do not show signs of regular helical movement.*

The trajectories of beads driven by dynein monomers (Figure 8) also displayed a helical component. The average pitch (579 nm ± 38 nm, 57 rotations, 11 beads) was similar to that of GST-Dyn331kD (t-test, p = 0.78) and higher than full-length dynein (t-test, p = 0.16). The majority (59%) of the rotations were right-handed in monomers, similar to full-length dimers (N-1 two proportion test, p = 0.47). The speeds of left- and right-handed movements along the helical path (66 ± 10 nm/s and

57 ± 6 nm/s, respectively) were statistically indistinguishable (t-test, p = 0.18). The results show that right-handed preference of dynein for helical movement is not strictly due to interhead orientation of a dimer.

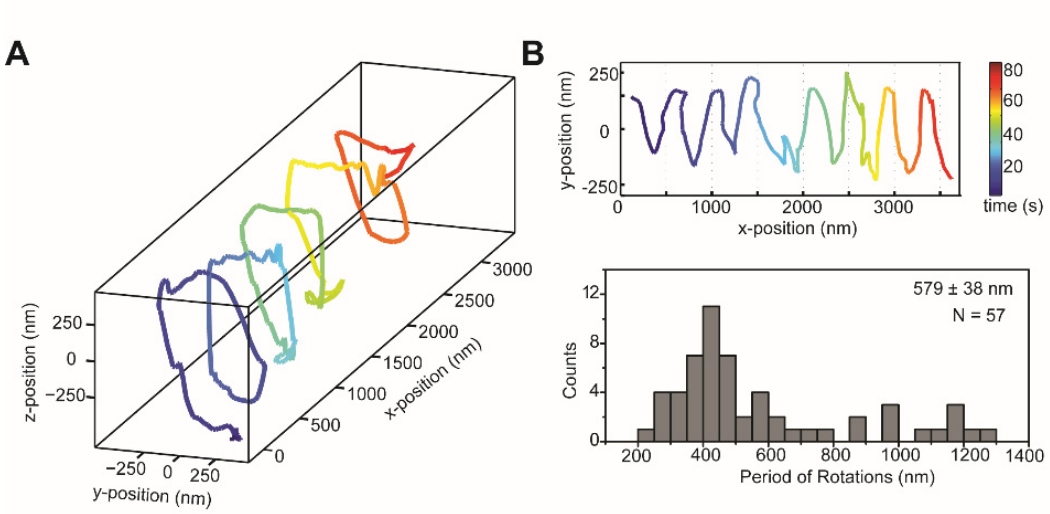

Figure 8: Dynein monomers prefer to move in a right-handed helix. *(A) Representative three-dimensional trace of a cargo bead driven by monomers shows right-handed helical motion.* ***(B)*** *(Top) Representative two-dimensional trace for monomeric Dyn_{331kD}. (Bottom) Histogram of the periods of rotations shows that the average pitch is 579 ± 38 nm (mean ± SEM). The average pitch of the left-handed movement (658 ± 92 nm, SEM, N = 17) was longer (t-test, p = 0.05) than that of the right-handed movement (490 ± 40 nm, SEM, N = 24).*

Discussion

In this study, we showed that cytoplasmic dynein moves along MTs in a helical trajectory with a pitch of ~500 nm. Single dynein dimers move along microtubules by taking frequent sideways steps [64], whereas multiple dynein dimers persistently move in a helical pattern with a net preference for a right-handed rotation. What is the molecular basis of this preference? Kinesin-1 monomers are believed to move to the closest possible site on the microtubule which stays on the left of the previous binding site [84]. However, kinesin-1 dimers move strictly forward due to a short neck linker that constraints off-axis stepping [80]. In dynein, monomers may prefer to attach to the nearest tubulin binding site towards the MT minus end, favoring to step towards right (Figure 9a). In the case of a dimer, the heads are attached to neighboring protofilaments and the leading head prefers to be on the right side at 30˚ relative to the trailing head [62, 63]. This orientation would favor the trailing to take a rightward step, resulting in a net rightward bias (Figure 9b).

In contrast to the other motors studied to date, dynein can move along both left- and right-handed helical paths. The molecular basis of the switches in helical directionality remains unclear. The irregular stepping pattern of individual motors rules out the possibility of rotational tug-of-war. Instead, we propose that the helical pattern of bead movement may be determined by the conformations of dynein motors associated with the MT track. It is likely that dyneins that are

bound in sufficiently close proximity to other dyneins experience steric exclusion effects. If a bead is carried by motors which are oriented such that one is bound immediately forward and to the right of the other, the tubulin binding sites ahead and to the right of the trailing head will be obstructed. Therefore, these motors may prefer to step to the left, and the entire cargo will eventually trace out a left-handed spiral. The number and orientation of the motors that are simultaneously in contact with the MT may change over the course of a recording. Individual dynein motors have 1,400 nm run length [64], indicating that motors on the bead detach and reattach during a processive run of a cargo bead. These may alter the orientation of the MT-bound motors, resulting in the reversal of helical directionality during a processive run (Figure 9), as occasionally observed.

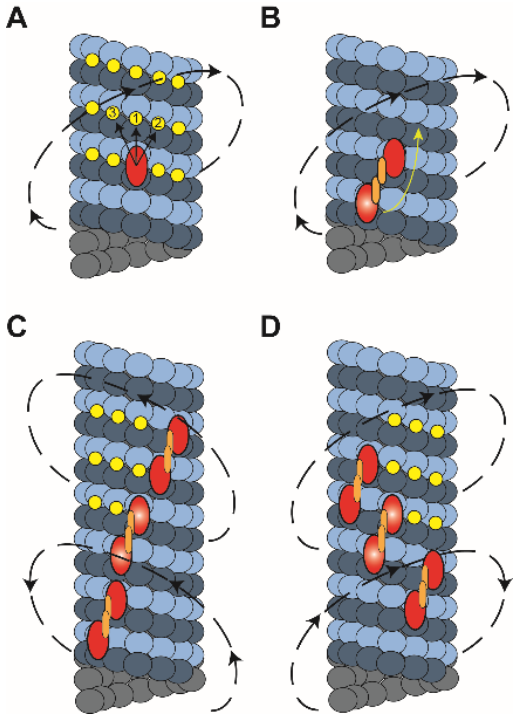

Figure 9: A model for the helical movement of cytoplasmic dynein. *(**A**) Top view of a monomeric dynein (red oval) stepping toward the MT minus end (arrows). The yellow circles represent the putative binding sites for the highlighted dyneins. The closest available binding sites are numbered from 1-3. The nearest (8 nm) binding site is along the same protofilament (1). The binding site on the right (2) has a shorter distance (9.3 nm) than the one in left (3, 10.8 nm), resulting in a tendency to step rightward. (**B**) A dynein dimer prefers to orient on a MT with the leading head positioned on the right of the trailing head. The trailing head prefers to step rightwards to orient on the right-hand side of its partner when it is positioned in the lead. (**C**) When multiple dimers carry a cargo bead, helical directionality may be affected by the number and orientation of the motors associated with an MT track. In this orientation, tubulin binding sites to the right for the motor in the middle may be obstructed for the motor in the lead. This results in a tendency to move in a left-handed helical pattern. (**D**) Due to the finite run length of dynein motors, MT-associated motors dissociate and new ones attach to the track. Changes in the orientation of MT-bound motors, switch the directionality of helical movement.*

Inside cells, the MT surface is crowded with associated proteins, which act as roadblocks during the transport of intracellular cargos [90]. Furthermore, the intracellular space is crowded with large structures, such as vesicles and organelles. The ability of molecular motors to produce torque as well as axial force may allow the motors to switch protofilaments and avoid these obstacles. In cells, the same MT track is used for both plus- and minus-end directed transport. Sideways movement may prevent traffic jams on MTs. *In vitro* assays have shown that dynein can bypass roadblocks whereas kinesin-1 stalls when it encounters an obstacle and eventually releases [91]. Bidirectional helical movement can provide additional flexibility to dynein to transport cargos in dense cellular environments.

Methods

Protein Preparation

S. Cerevisiae strains expressing mutant forms of cytoplasmic dynein (*Dyn1*) gene were generated by homologous recombination. Proteins were expressed and purified as described [64].

MTs polymerized under 10 mM paclitaxel contain a mixture of 12, 13 or 14 protofilaments. In MTs with 13 protofilaments, the protofilament long axes align with the MT long axis, whereas MTs with 12 and 14 protofilaments have a right-handed supertwist with 4 μm pitch and left-handed supertwist with 6,400 nm pitch, respectively [86]. GMP-CPP MTs were grown for 3 hours at 37°C from a 50 μL BRB80 buffer (80 mM PIPES pH 6.9 with KOH, 1mM $MgCl_2$, 1mM EDTA) solution supplemented with 5 μM tubulin (80% unlabeled porcine tubulin, 20% HiLyte 647 labeled porcine tubulin (Cytoskeleton)), 1 mM GMP-CPP and 2 mM $MgCl_2$. Assembled MTs were pelleted at 40,000 *g* with Beckman Ti 102.1 rotor and resuspended in 60 μL BRB80 buffer. The average length of HiLyte 647 labeled MTs was 15 μm.

Labeling Beads with Antibodies

Carboxylated polystyrene beads were coated with anti-rabbit polyclonal GFP antibodies (Covance). The beads were initially pelleted and resuspended in the activation buffer (100 mM MES, 100 mM NaCl, pH 6.0). Carboxyl groups on the surface of the bead were functionalized with amine reactive groups via EDC and sulfo-NHS (Pierce) crosslinking for 30 minutes at room temperature. The beads were then washed with phosphate buffer saline (PBS) at pH 7.4 and anti-GFP antibodies were added to the beads and reacted for 3 hours in room temperature. Excess antibodies were removed by centrifugation. The beads were resuspended in PBS along with 0.1% azide for storage purposes.

Preparation of Protein-Bead Complexes

GFP was fused to the N-terminus of the SRS – dynein MTBD chimeric construct (GFP-$SRS_{85:82}$). GFP was used for attachment to an anti-GFP antibody-coated bead and the MTBD stably binds to a MT [72, 85]. GFP-$SRS_{85:82}$ does not generate motility on its own [72, 85]. Saturating amount of GFP-$SRS_{85:82}$ was incubated with anti-GFP coated carboxyl beads (2 μm diameter) on ice for 10 minutes in dynein assay buffer (DLB; 80 mM HEPES pH7.4, 1 mM EGTA, 2 mM $MgCl_2$ and 10%

glycerol) containing 1 mg/ml casein. Excess SRS protein was removed by centrifugation at 15,000 g and the beads were resuspended in DLB.

Preparation of Flow Chambers

$SRS_{85:82}$ coated beads were nonspecifically adsorbed to the coverslip. After 10 minutes of incubation, unbound beads were removed by washing the chamber twice with 30 µL DLB + 1 mg/ml casein. Casein was used to pre-block nonspecific surface attachment of MTs and motor proteins. Next, fluorescently labeled MTs were flowed and incubated for 10 minutes. Free MT's were washed with 30 µL DLB+1 mg/ml casein buffer. We observed less than 20 bridges in 1,000 µm x 1,000 µm area. The bead density was kept low (4 beads on average in 20 µm x 20 µm area) and MT concentration was kept high to ensure that each bridge was formed by a single MT. Motor coated beads always moved unidirectionally without changing the direction of motion along the MT long axis during processive motility, excluding the possibility of bridges containing multiple MTs pointing in opposite directions. Finally, a solution containing dynein-coated 0.5 µm diameter beads in DLB buffer supplemented with 2.5 mM PCA (protocatechuic acid) and 50 nM PCD (protocatechuate-3,4-dioxygenase) oxygen scavenging system [92], 1mg/ml casein and 1 mM ATP were flowed to the chamber and sides of the chamber were sealed with nail polish to prevent evaporation of the assay solution.

Data Collection

The assays performed with a custom-built optical trapping microscope equipped with Nikon TiE microscope body, Nikon 100 X 1.49 NA plan apochromat objective and an electron multiplied charge coupled device (EM-CCD) camera (Andor, Ixon^{+}). HiLyte-labeled MTs were excited with 632 nm laser beam in epifluorescence mode and the fluorescent signal was detected by the EM-CCD camera with an effective pixel size of 160 nm. The movies were recorded at 100 ms frame rate. The surface of the flow chamber is scanned to find MT bridges between the two 2-µm-diameter beads. We performed our bead tracking assays on the bridges, in which MTs are 10-15 µm long between the beads, appear steady by the resolution of a fluorescence microscope (250 nm) at 10 Hz frame rate, and the entire MT fluorescence appears in focus.

A 0.5 µm cargo bead freely diffusing in solution was trapped by a focused 1064 nm laser beam. The trap is steered with a pair of acousto-optical deflectors (AA Opto-Electronic) and bead position was detected by a position sensitive detector using back-focal-plane interferometry. Leakage of the intense trapping beam to fluorescence detection was blocked by a 708/75 nm bandpass filter (Semrock).

A single MT bridge was used over the course of one experiment. The dynein-coated beads were captured with an optical trap and brought to the proximity of the MT. When the motors on the cargo bead attached to the MT and started to move, the optical trap was turned off. The movement of beads was recorded using bright-field microscopy. MT polarity was first tested by placing the bead on a MT at the center of the bridge. Once the directionality is determined, the bead was moved away from the MT and placed at the plus-end tip of the bridge to explore the motility throughout the entire length of the bridge. All of the beads moved towards the same direction on a single bridge, without any reversals in axial direction.

The movement of single quantum dots on MT bridges was determined by labeling GST-Dyn$_{331kD}$ motors at a C-terminus with a quantum dot 655 using HaloTag attachment [62]. Because side to side movements are smaller in the case of Q-dots (~50 nm) compared to beads (~500 nm), the MT fluctuation was subtracted from Quantum-dot labeled dynein data. To measure the oscillation of the MT bridges, the MTs were sparsely labeled with a quantum dot 585. The standard deviation of the position of 585 quantum dots was 35 nm in perpendicular direction and 17 nm in parallel direction to the long axis of the MTs. The position of 585 quantum dots was subtracted from the quantum dot 655 labeled dyneins to correct for MT oscillations.

Data Analysis

Cargo beads were tracked by using custom-written software, which utilizes Gaussian fitting to determine the *xy* position of the bead. The precision of bead tracking was 3 nm in *x* and 5 nm in *y* directions. *z* position of the bead was determined by the intensity of the bead center. To calibrate the bead intensity as a function of *z* position, the surface of a sample chamber was decorated with 0.5 μm diameter beads. The microscope objective was moved ±250 nm in the *z*-direction with 25 nm increments using PIFOC objective scanner (Physik Instrumente). Corresponding intensities of peaks at each frame were plotted with the z position relative to the microscope objective. This routine is repeated for 20 times to obtain a calibration curve shown in Figure 4c,d. The bead intensity profile was fitted with a third order polynomial function and the z position of the bead was calculated from the calibration curve. The bead image could not be well-fit by a Gaussian when the *z* position was between -25 nm and +25 nm. To avoid sample-to-sample variability in calibration procedures, the background was subtracted and the intensities were normalized in the bright-field images of the bead. Traces of bead motility were smoothed by the moving average filter of window of 5 data points.

The pitches of the helical motion of the beads are corrected for the 6,400 nm left-handed supertwist of GMP-CPP MTs. The corrected pitch is longer than the measured pitch for left-handed rotations and shorter for right-handed rotations. The corrected pitch is calculated by:

$$\frac{1}{pitch_{measured}} = \pm\frac{1}{pitch_{MT}} + \frac{1}{pitch_{corrected}}$$

Dynein's directionality is controlled by the angle and length of its stalk

The work presented in this chapter is accepted for publication as the following manuscript: Dynein's directionality is controlled by the angle and length of its stalk written by Sinan Can*, Samuel Lacey*, Mert Gur, Andrew P. Carter, Ahmet Yildiz. (* equal contribution, **Nature**, 2018)

Abstract

The ability of cytoskeletal motors to move unidirectionally along filamentous tracks is central to their role in cargo transport, motility and cell division. While kinesin and myosin motor families have members that move in opposite directions[5, 93, 94], all dyneins studied to date exclusively move towards the microtubule (MT) minus-end[8]. In order to understand the mechanism of dynein's directionality, we sought to engineer a plus-end-directed dynein guided by cryo-electron microscopy and molecular dynamics simulations. As shown by single-molecule assays, elongation or shortening of the coiled-coil stalk that connects the motor to the MT controls helical directionality of *S. cerevisiae* dynein around MTs. By changing the length and angle of the stalk, we successfully reversed the motility towards the MT plus-end. These modifications act by altering the direction dynein's linker swings relative to the MT, not by reversing the asymmetric unbinding of the motor from MT. Because the length and angle of dynein's stalk are fully conserved among species, our findings provide an explanation for why all dyneins move towards the MT minus-end.

Introduction

Dyneins are a family of AAA+ motors responsible for nearly all minus-end-directed motility and force generation functions along MTs [8, 64, 66]. Due to roles in intracellular transport, cell division and axonemal beating, defects in dynein motility are linked to many developmental and neurodegenerative disorders[95]. The dynein motor domain contains a catalytic ring of six AAA+ modules (AAA1-6) connected to a MT binding domain (MTBD) by an antiparallel coiled-coil stalk (Figure 10a)[96]. Motility is powered by conformational changes of a linker that resides on the face of the ring. ATP binding to AAA1 triggers MT release and moves the linker into a bent conformation, referred to as the priming stroke[8]. After ATP hydrolysis, dynein rebinds to the MT and the linker returns to its straight conformation[46, 47, 52, 53], which serves as the force-generating powerstroke of dynein's mechanochemical cycle[53].

There are two current models for the mechanism underlying dynein directionality. The linker swing vector (LSV) model suggests that the motor domain pivots around the linker and its stepping follows the direction the linker swings relative to the MT (Figure 10a)[52, 72, 97]. Because dynein has multiple flexible elements in its structure[98, 99], it remains unclear whether the LSV mechanism is capable of providing a net bias towards the minus-end during stepping. Alternatively, the asymmetric release model proposes that faster release of dynein when pulled towards the minus-end[66, 73, 74] creates a net bias in minus-end directionality. Consistent with this model, an engineering

study[75] that replaced dynein's MTBD with actin-binding proteins suggested that unidirectional motility can be facilitated by asymmetric release from the cytoskeletal track, regardless of which direction LSV is pointed.

Results

The stalk length is critical to align dynein motility along the MT long-axis

We tested the LSV model by altering the direction in which the linker swings and determining how this affects dynein motility. According to this model, pointing LSV sideways relative to the MT would create a net bias on helical directionality of dynein around the circumference of MTs. All-atom molecular dynamics (MD) simulations predicted that elongation or shortening of the stalk coiled-coils by 3 heptads ($Dyn_{\pm 3hep}$) rotates the AAA+ ring around the stalk axis and shifts the LSV rightward and leftward, respectively, along the MT short-axis (LSV_{short}, Figure 10b, Figure 11). We determined the helical directionality of dynein-driven beads on MT bridges[100]. As previously observed[62, 63], the beads driven by tail-truncated monomeric dynein (Dyn) moved in both clockwise and counterclockwise helical trajectories without a significant sideways bias ($p = 0.05$, Student's t-test, Figure 10c, d). In contrast, beads driven by Dyn_{+3hep} rotated mostly clockwise, while Dyn_{-3hep} rotated the beads counterclockwise around MTs, consistent with the predicted directions of their LSV_{short} (Figure 10c, d). We concluded that the stalk length of native dynein is critical for restricting sideways movement and directing motility primarily along the MT long-axis.

Dynein stalk angle is critical to align the linker swing vector towards minus end

Altering the stalk length, which rotates the AAA+ ring relative to the stalk axis, did not affect the minus-end directionality of dynein motility[72] (Figure 11). This could be because dynein's stalk is tilted ~45° towards the plus-end, which points the LSV long-axis component (LSV_{long}) to the minus-end (Figure 12, Figure 13a)[72, 98, 101]. To change the stalk angle, we shifted the positions of two fully-conserved proline residues at the base of MTBD along the stalk coiled-coils. MD simulations indicated that a dynein mutant with a two-residue shift of both prolines ("reverse kink", Dyn_{RK}, Figure 12) can fold properly into a well-ordered structure in which the stalk is tilted in the reverse direction (Figure 13b). Simulations also predicted that pointing LSV_{long} towards the plus-end requires not only tilting of the stalk towards the minus-end, but also reversal of the ring relative to the stalk axis with +7hep insertion ($Dyn_{RK+7hep}$, Figure 13b,c,d).

To test the structural predictions of the MD simulations, we imaged monomeric Dyn and $Dyn_{RK+7hep}$ bound to MTs using cryo-electron microscopy (cryoEM). Two-dimensional classification of $Dyn_{RK+7hep}$ showed that the stalk length was extended to 18.5 ± 1.9 nm, compared to 12.7 ± 1.2 nm for Dyn, compatible with the predicted ~7 nm elongation of the stalk due to +7hep insertion (Figure 14). Centered on a pivot at the base of the stalk, a broad range of stalk angles was observed for both Dyn and $Dyn_{RK+7hep}$. The average Dyn stalk angle was measured as 55 ± 26° (Figure 13e,f) [72, 98, 101]. $Dyn_{RK+7hep}$ had a wider distribution of stalk angles and the majority of the molecules had their stalk tilted towards the opposite direction to Dyn (111 ± 35°, mean ± s.d.). Density for the linker remains below the ring for $Dyn_{RK+7hep}$ (Figure 13e), showing that the ring is

rotated relative to its stalk axis. These results confirm our prediction that RK+7hep modifications reverse the stalk angle and rotate the ring relative to the stalk axis.

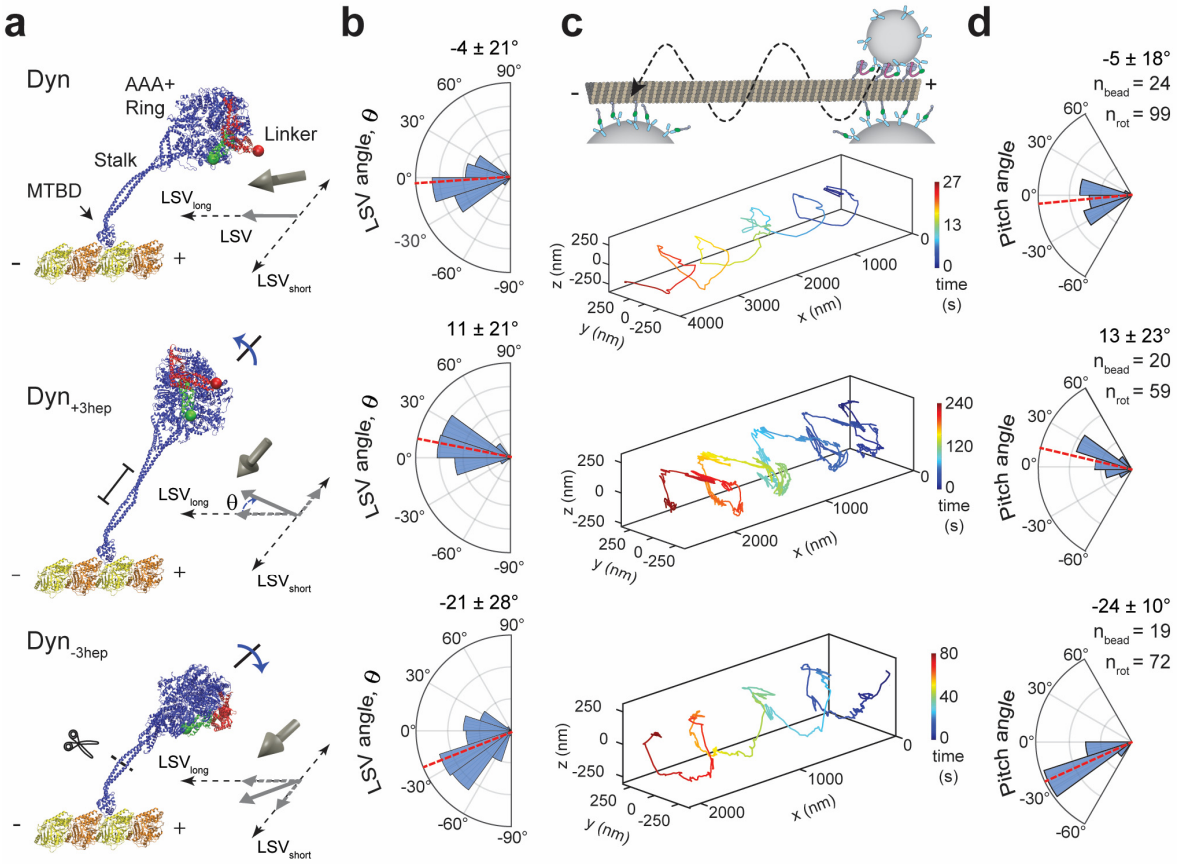

Figure 10: The stalk length is critical to align dynein motility along the MT long-axis. a, *A dynein head is superimposed onto an MT and the linker is highlighted in its pre- (red) and post-powerstroke (green) conformation (Protein Data Bank (PDB) accession numbers 3VKG, 4RH7, 3J1T). The LSV (grey arrow) is defined as the displacement of the linker from the pre- (red bead) to post-powerstroke (green bead) conformation. The projection of LSV to MT long axis is pointed towards the minus-end for Dyn (see Methods). Dyn$_{+3hep}$ and Dyn$_{-3hep}$ were modeled by +3hep insertion and -3hep deletion of the stalk and re-alignment of the stalk coiled-coils in Dyn conformations obtained from MD simulations. Changing the stalk length is expected to rotate the ring and project LSV sideways (θ).* ***b,*** *Calculated LSV angles from MD simulations (mean ± s.d., n > 1,000). p <0.0001 for Dyn vs. Dyn$_{-3hep}$ and Dyn vs. Dyn$_{+3hep}$.* ***c,*** *(Top) A schematic represents helical motility of 0.5 μm diameter cargo beads driven by monomeric dyneins around a MT bridge. (Bottom) Example trajectories of beads driven by Dyn, Dyn$_{+3hep}$ and Dyn$_{-3hep}$. Cargo beads carried by Dyn$_{+3hep}$ and Dyn$_{-3hep}$ rotate clockwise and counterclockwise around a MT, respectively.* ***d,*** *The histogram of the pitch angles (mean ± s.d.). Helical directionality of dynein motility follows the direction of LSV$_{short}$. p <0.0001 for Dyn vs. Dyn$_{-3hep}$ and Dyn vs. Dyn$_{+3hep}$. p >0.3 for comparisons of Dyn, Dyn$_{+3hep}$ and Dyn$_{-3hep}$ histograms in b and d (t-test).*

We next tested whether mutations to the Dyn$_{RK+7hep}$ stalk disrupt the mechanical properties crucial for robust dynein motility[51, 85]. MT affinity of monomeric Dyn$_{RK+7hep}$ was similar to Dyn under different nucleotide conditions (Figure 15a). Dyn$_{RK+7hep}$ showed robust MT-stimulated ATPase activity, albeit with an elevated basal ATPase and slightly lower catalytic rate compared to Dyn (Figure 15b).

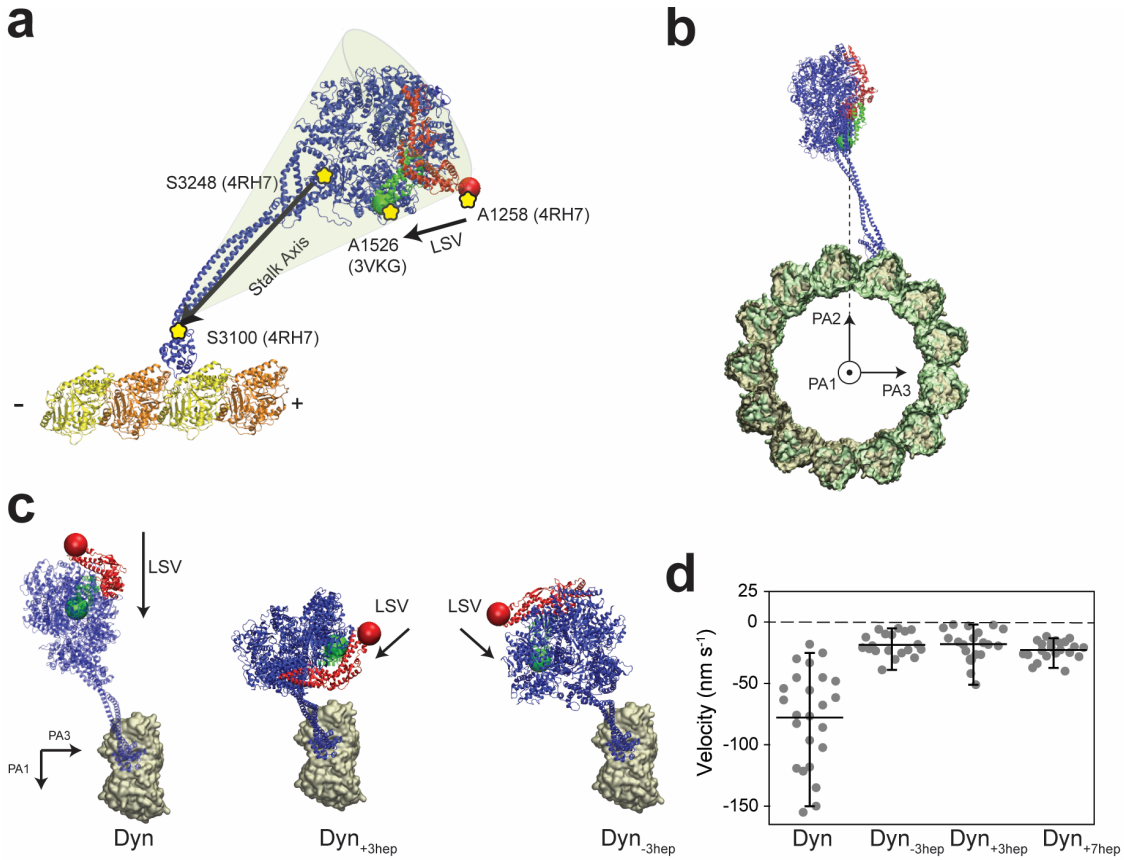

Figure 11: Estimated orientation of LSV relative to a MT as a function of stalk length. a, *A tail truncated yeast cytoplasmic dynein monomer (Dyn) was manually docked onto a tubulin dimer (pdb# 3VKG[46], 4RH7[53], 3J6G[102] and 5SYF[103]). LSV was defined as the displacement vector of the N-terminus of the linker from pre- (V1258 of pdb# 4RH7, red bead) to post-powerstroke (A1526 of pdb# 3VKG, green bead) conformation. The stalk axis was defined as the vector that connects S3100 to S3248 (pdb# 4RH7), which lies in the same plane with LSV of Dyn.* ***b,*** *Definition of the principle axes (PAs). Dyn was manually docked onto a MT. The longitudinal axis (PA1) is directed towards the minus end of the MT long axis. The radial axis (PA2) is directed from the MT center of mass towards the pre-powerstroke conformation of the linker (V1258 of pdb# 4RH7, red bead). The tangential axis (PA3) is perpendicular to PA1 and PA2, as shown.* ***c,*** *LSV (black arrow) of Dyn is aligned with the MT axis and parallel to PA1. Expected orientations of Dyn$_{+3hep}$ and Dyn-$_{3hep}$ were modeled by alignment of the coiled coils after insertions and deletions to the stalk. Insertion of 3 heptads to the stalk (Dyn$_{+3hep}$) is expected to reorient the ring and rotate LSV$_{short}$ clockwise with respect to MT minus-end. Shortening the stalk by 3 heptads (Dyn$_{-3hep}$) is expected to rotate LSV$_{short}$ counterclockwise.* ***d,*** *Velocity analysis of dynein-driven beads around MT bridges. All of the beads moved towards the MT minus-end. n = 24, 20, 19 and 22 beads from left to right. Center line and error bars represent the mean and 5-95% confidence intervals ($p < 0.001$ for Dyn$_{+3hep}$, Dyn-$_{3hep}$ and Dyn$_{+7hep}$ vs. Dyn). Molecular dynamics simulations and analysis were performed by Mert Gur.*

We also determined how external load affects the velocity and MT release of Dyn$_{RK+7hep}$ using an optical trap. Similar to Dyn[65], a full-length Dyn$_{RK+7hep}$ moved processively towards the direction of applied load in the absence of nucleotide. Velocity increased continuously when the motor was pulled towards the minus-end, whereas the motility was slow when pulled towards the plus-end (Figure 15c,d). A Dyn$_{RK+7hep}$ monomer has similar force-induced MT release rates to Dyn, rapidly releasing from MTs when pulled towards the minus-end and resisting a plus-end-directed pull of

the optical trap (Figure 15e,f). Therefore, the mutations we introduced in Dyn$_{RK+7hep}$ do not disrupt nucleotide-dependent communication between the ring and MTBD or the asymmetric release from MT.

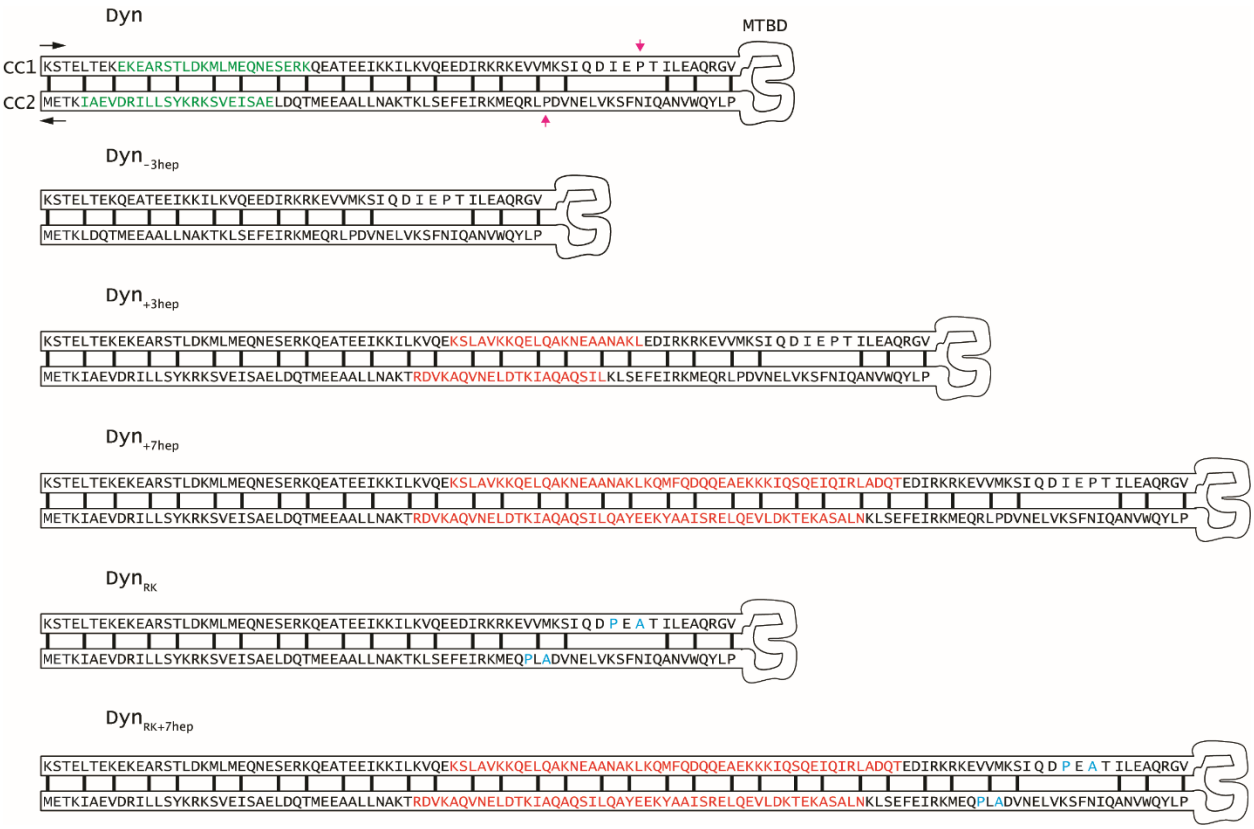

Figure 12: Engineering the directionality of dynein motility. *Schematic diagram of the helices (CC1 and CC2) at the stalk of yeast cytoplasmic dynein shows the heptad repeat hydrophobic contacts (black lines) in the core of the coiled-coil when dynein is at low MT affinity (β) state. Conserved proline residues at the base of Dyn's stalk are highlighted with magenta arrows. 3 heptads deleted from the stalk of Dyn$_{-3hep}$ are highlighted with green in Dyn. 3 and 7 heptad repeats inserted to Dyn$_{+3hep}$, Dyn$_{+7hep}$ and Dyn$_{RK+7hep}$ are highlighted in red. The inserted sequences were taken from the Drosophila melanogaster cytoplasmic dynein[72]. Point mutations inserted to Dyn$_{RK}$ and Dyn$_{RK+7hep}$ are highlighted in cyan*

Dynein's directionality is reversed by altering the length and the angle of its stalk

We inserted these mutations into tail-truncated, GST-dimerized dynein[64] and tested the directionality of their motility in MT gliding assays (Figure 16a). Dyn$_{RK}$ motors exhibited very slow motility towards the minus-end consistent with the predicted direction of its LSV (Figure 13). In contrast, Dyn$_{RK+7hep}$ glided all MTs towards the plus-end (Figure 16b), demonstrating that modifications in this construct successfully reverse dynein direction. Increasing the ionic strength resulted in faster gliding velocity of both Dyn and Dyn$_{RK+7hep}$ without affecting their directionality.

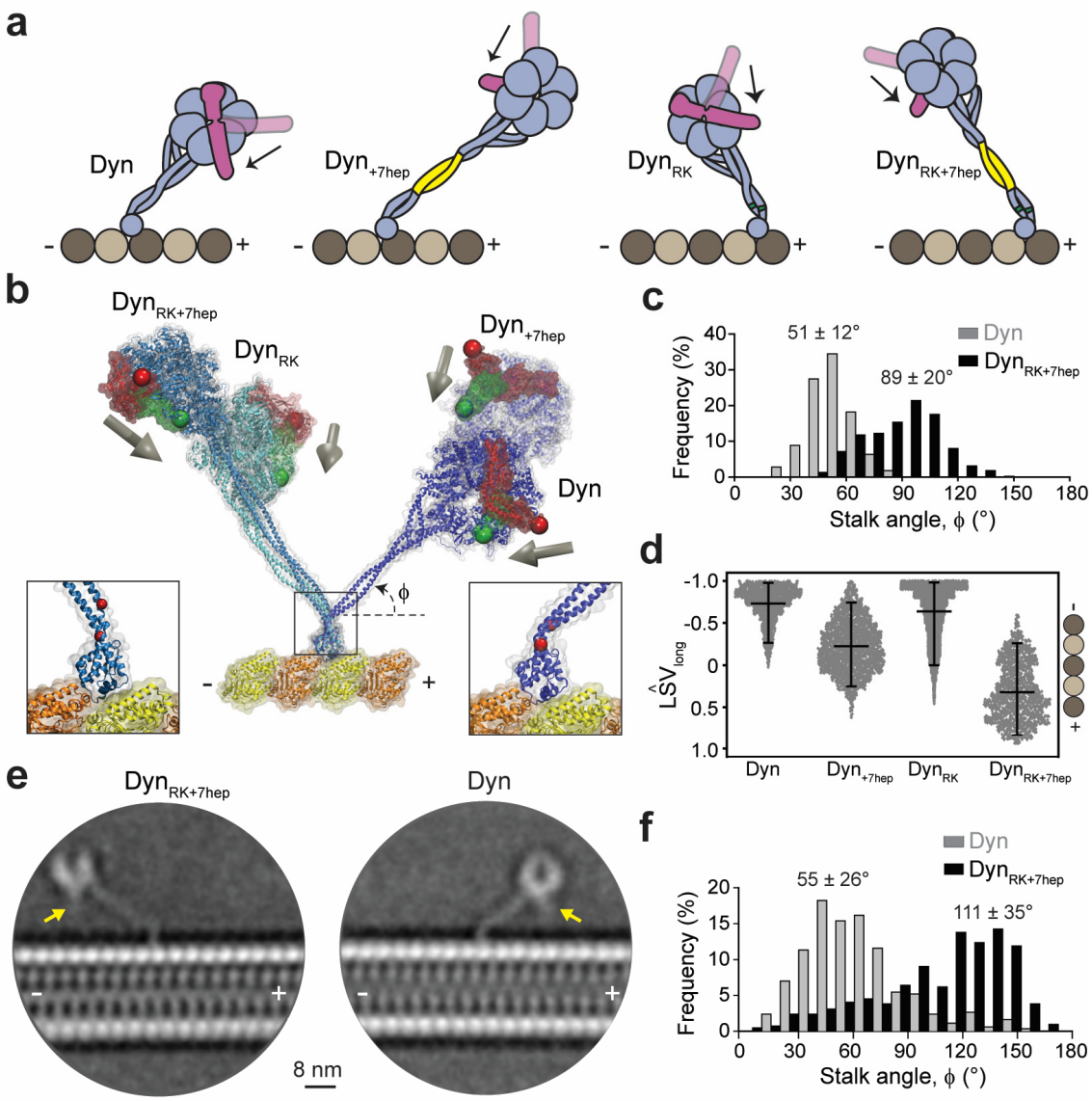

Figure 13: The stalk angle is reversed by shifting the position of two conserved prolines. a, *Expected LSV_{long} orientation (black arrow) in Dyn, Dyn_{+7hep}, Dyn_{RK} and $Dyn_{RK+7hep}$. Altering both the angle and length of the stalk in $Dyn_{RK+7hep}$ is expected to direct LSV_{long} towards the MT plus-end.* ***b,*** *Example snapshots from all-atom MD simulations for an N-terminal truncated dynein monomer in the pre-powerstroke conformation docked onto MT. Post-powerstroke conformation of the linker was superimposed to calculate the LSV orientation (grey arrows). (Right insert) Simulations confirmed plus-end directed tilt of Dyn's stalk due to two conserved proline residues (red) at its base. (Left insert) Dyn_{RK} and $Dyn_{RK+7hep}$ can fold into a reverse kink structure by shifting the positions of the proline residues two positions away from MTBD.* ***c,*** *Stalk angle (ϕ) distributions from Dyn and $Dyn_{RK+7hep}$ simulations (mean ± s.d., $p < 0.001$).* ***d,*** *The length of the LSV unit vector projected onto the MT long axis measured by MD simulations (mean ± s.d.). -1 corresponds to LSV pointed towards the minus-end. The center line and edges represent mean and 5-95%, respectively. Each pair of distribution is statistically different from each other ($p < 0.001$, t-test).* ***e,*** *CryoEM 2D class averages of Dyn and $Dyn_{RK+7hep}$ monomers bound to a MT show different orientations of their stalk. Arrows point to the N-terminus of the linker.* ***f,*** *The histogram of the stalk angles for Dyn ($n = 392$) and $Dyn_{RK+7hep}$ ($n = 421$) relative to the MT long-axis (mean ± s.d., $p < 0.001$). 180° represents tilting of the stalk towards the MT minus-end. CryoEM imaging and analysis were performed by Samuel Lacey.*

In single molecule motility assays, 90% of full-length $Dyn_{RK+7hep}$ dimers walked processively towards the plus-end by taking nanometer-sized steps (Figure 16c,d). The average step size of $Dyn_{RK+7hep}$ in the plus-end direction was slightly higher (14.1 ± 7.7 nm) than Dyn step size towards the minus end (13.0 ± 6.7 nm, p = 0.026, t-test), suggesting that lengthening the stalk causes a modest increase in step size (Figure 16e). We also observed a robust plus-end directionality of multiple monomeric $Dyn_{RK+7hep}$ in MT gliding and bead motility assays (Figure 17). These results provide direct evidence that dynein's direction is reversed when the LSV points towards the plus-end.

Backward stepping of $Dyn_{RK+7hep}$ was more frequent than backward stepping of Dyn (35% vs 16%, $p < 0.001$). This might result from the asymmetric release of both $Dyn_{RK+7hep}$ and Dyn when pulled towards the minus-end (Figure 15f). While tension-induced stepping contributes to forward movement of the lagging head in Dyn[62, 63, 73, 74], this mechanism is expected to favor stepping backwards during the plus-end directed movement of $Dyn_{RK+7hep}$. Overall, $Dyn_{RK+7hep}$ moves towards the plus-end even though it releases faster and moves towards the minus-end under tension. We, therefore, conclude that the direction of the LSV, rather than of tension-induced release, is the primary mechanism of dynein directionality.

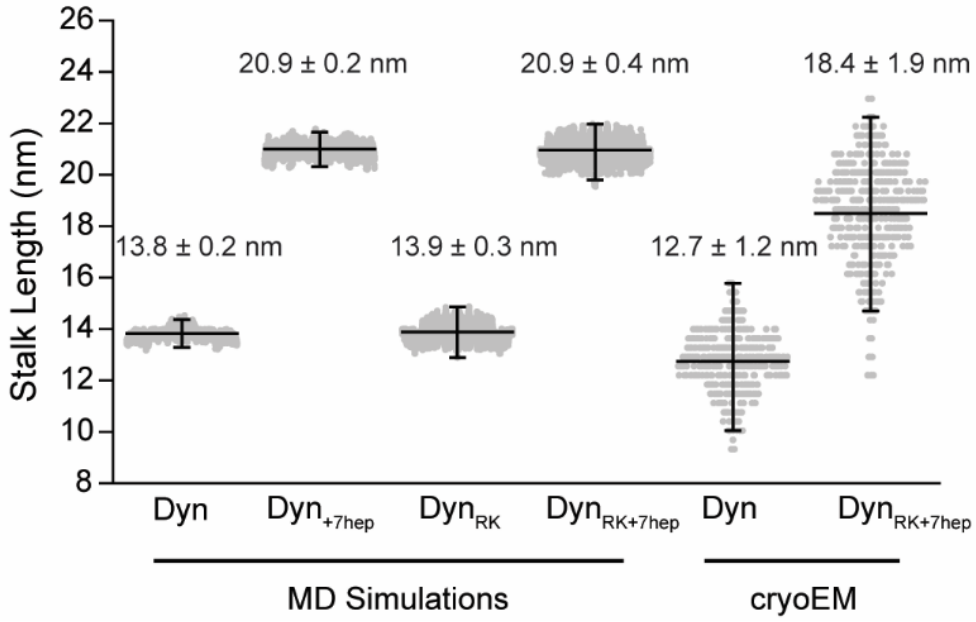

Figure 14: Stalk length distributions from MD simulations and cryo-EM experiments. *Centerline and error bars represent the mean and 5-95% confidence intervals ($p < 0.001$ between $Dyn_{RK+7hep}$ vs. Dyn in both MD and cryoEM data, t-test).*

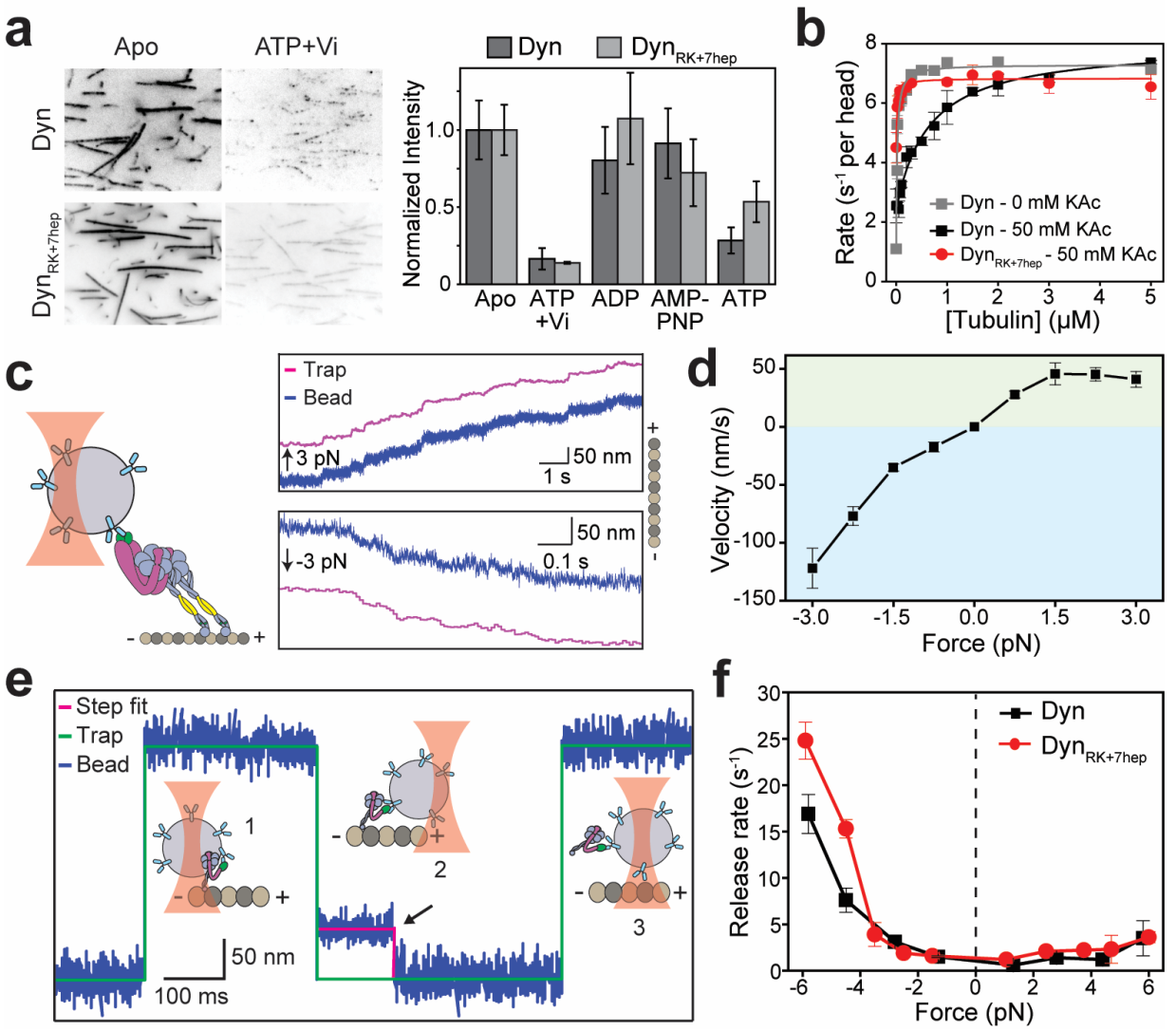

Figure 15: Reversal of the stalk angle does not disrupt nucleotide- and force-induced release of dynein from MT. a, *(Left) Representative images and (Right) normalized intensity of 100 nM GFP-tagged Dyn and Dyn$_{RK+7hep}$ monomers on sea urchin axonemes under given nucleotide conditions. Similar to Dyn, Dyn$_{RK+7hep}$ released from MTs in the ADP-Pi state, mimicked by ATP and vanadate (Vi). Error bars represent s.d. of 40 axonemes from three independent measurements ($p > 0.07$ for pairwise comparisons between Dyn and Dyn$_{RK+7hep}$ under the same nucleotide conditions, $p < 0.0001$ between apo and ADP.Vi).* ***b,*** *MT-stimulated ATPase activity of dynein in 2 mM ATP (mean ± s.d. from three independent measurements) under different salt concentrations. Solid curves represent fit to the Michaelis-Menten kinetics.* ***c,*** *(Left) Full-length Dyn$_{RK+7hep}$ was attached to a polystyrene bead and pulled by constant load using optical trap (not to scale). (Right) Representative trajectories of single Dyn$_{RK+7hep}$ when pulled by 3 pN towards the plus- (positive forces) and minus-end (negative forces) of a MT.* ***d,*** *Force-velocity relationship of Dyn$_{RK+7hep}$ in the apo condition (mean ± s.e.m., n = 20, 21, 19, 16, 15, 23, 15, 15, 20 from left to right).* ***e,*** *Dynein monomers were attached to a polystyrene bead through their linker and oscillated ±150 nm along the MT long-axis by the optical trap (1). When a molecule binds to the MT (2), the movement of the bead to the next trap position is restricted and the trap exerts a constant force until the motor releases from the MT (the black arrow, 3).* ***f,*** *Similar to Dyn, Dyn$_{RK+7hep}$ favors faster release from a MT when pulled towards the minus-end. Each bin contains a minimum 50 data points from two measurements. Errors are calculated from an exponential decay fit to the dwell time histograms.*

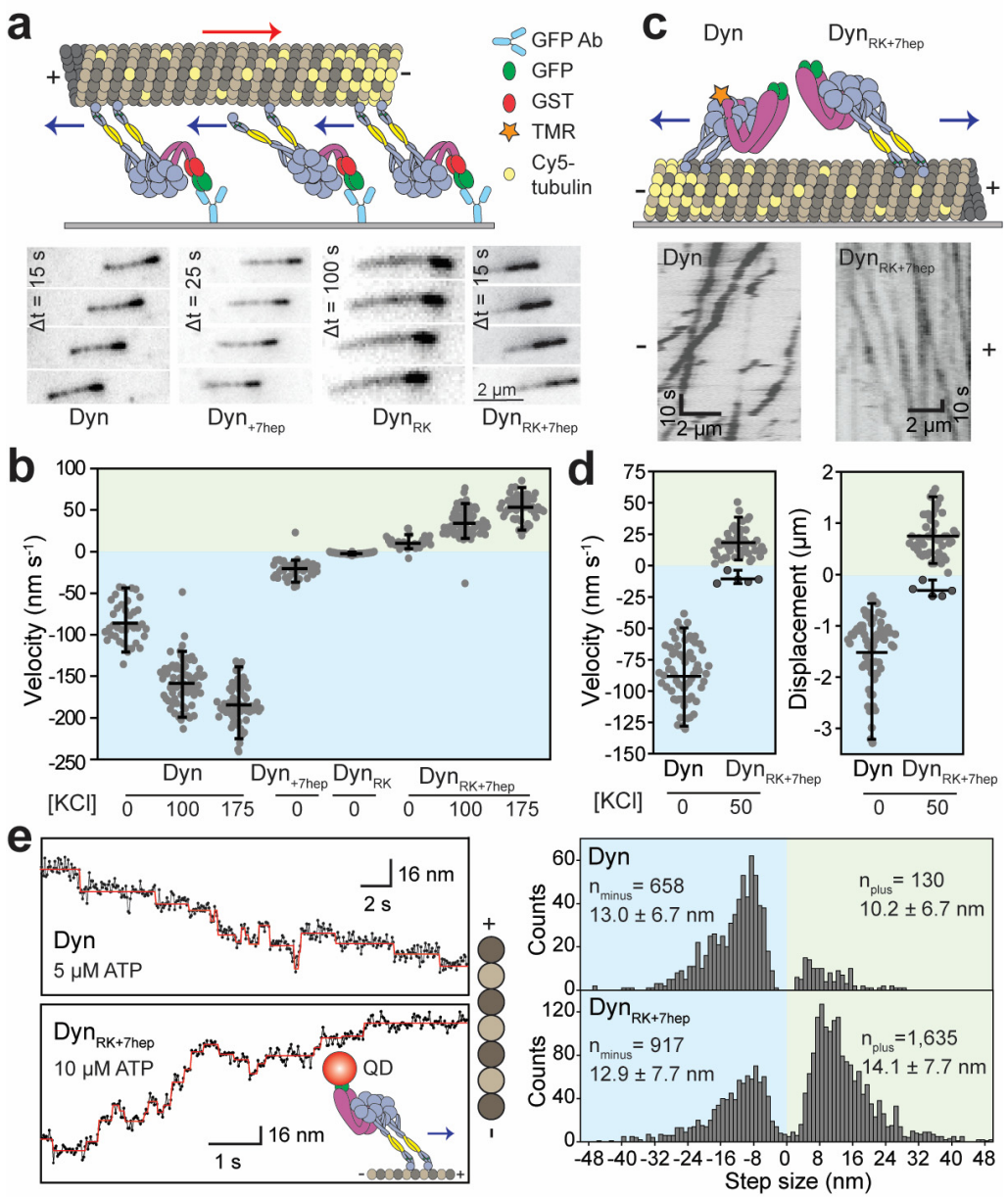

Figure 16: Dynein's directionality is reversed by altering the length and the angle of its stalk. a, *(Top) The schematic represents the MT gliding activity of surface-immobilized dyneins. (Bottom) Time-lapse recordings show that Dyn, Dyn$_{+7hep}$ and Dyn$_{RK}$ glide MTs with the plus-end in the lead, whereas Dyn$_{RK+7hep}$ glides MTs towards the opposite direction.* ***b,*** *MT gliding velocity and directionality of dynein mutants at given salt concentrations. Negative velocities correspond to minus-ended directed motility. n = 38, 69, 60, 49, 59, 49, 83 and 53 from left to right ($p < 0.001$ for Dyn$_{RK}$ and Dyn$_{RK+7hep}$ vs Dyn).* ***c,*** *(Top) Schematic representing single molecule motility assays. (Bottom) Example kymographs show processive motility of Dyn and Dyn$_{RK+7hep}$ dimers.* ***d,*** *Velocity and run length of Dyn and Dyn$_{RK+7hep}$ dimers. n = 67 and 58 from left to right ($p < 0.001$, t-test).* ***e,*** *(Left) Example trajectories QD-labeled Dyn and Dyn$_{RK+7hep}$ stepping along MTs at 20 ms temporal resolution. The QD position (solid dots) was fit by a step-finding algorithm (red lines). (Right) Histogram of step size distribution (mean ± s.d.). In b, d and e, yellow and cyan shaded regions represent plus- and minus-end directed motility, respectively. In b and d, the center line and edges represent mean and 5-95%, respectively. In d and e, mean values for plus- and minus-end directed runs and steps are calculated separately.*

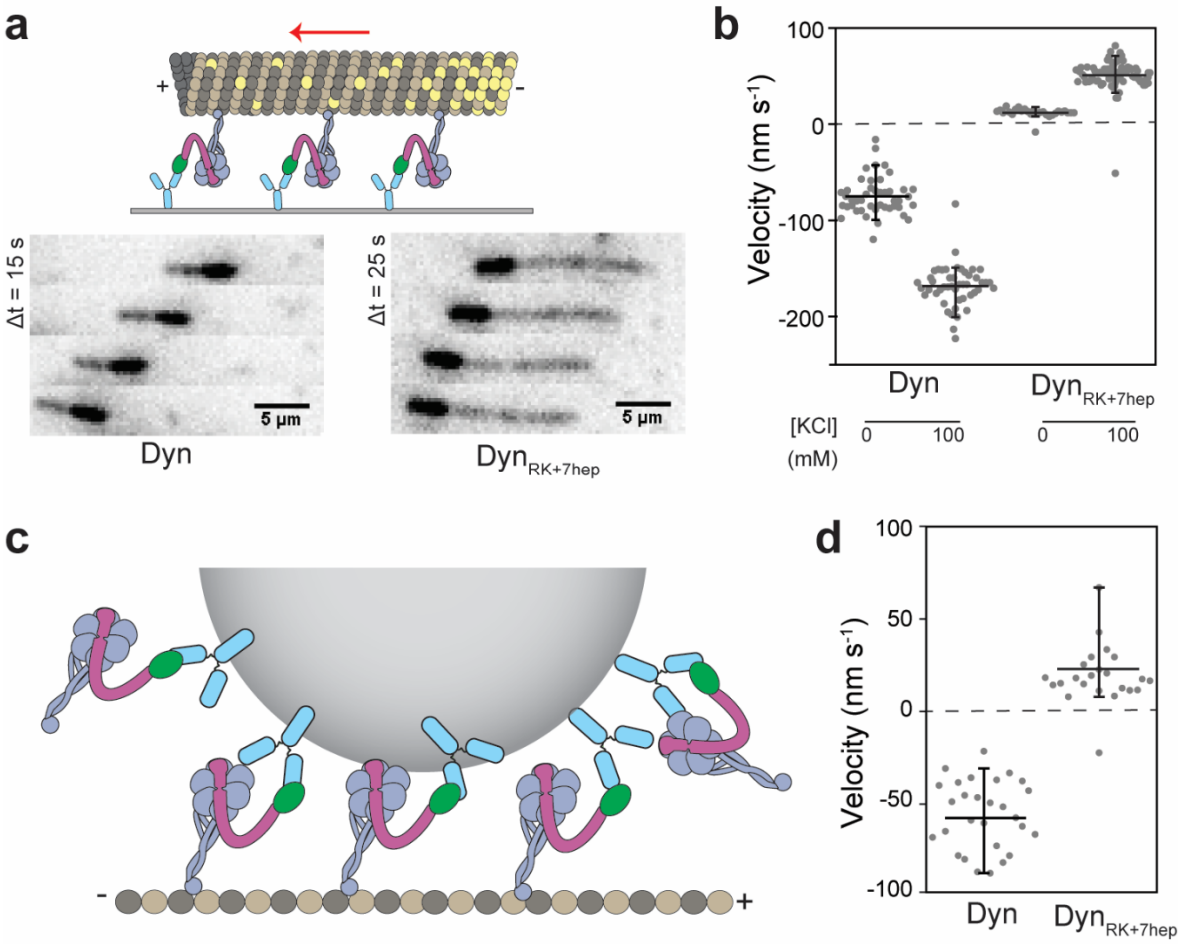

Figure 17: DynRK+7hep monomers exhibit robust plus-end directionality in MT gliding and bead motility assays. a, *(Top) The schematic represents the MT gliding assay with monomeric dynein. (Bottom) Images from time-lapse recordings show gliding of polarity marked MTs by Dyn and DynRK+7hep monomers. While Dyn glides MTs with their plus-end in the lead, DynRK+7hep glides MTs towards the opposite direction.* ***b,*** *MT gliding velocity and directionality of Dyn and DynRK+7hep in the presence and absence of 100 mM KCl. Negative velocities correspond to minus-end directionality. n = 45, 47, 27 and 70 from left to right from two independent measurements ($p < 0.001$ for comparison between DynRK+7hep and Dyn for 0 and 100 mM KCl conditions).* ***c,*** *The schematic of the bead motility assay with monomeric dynein (not to scale). N-terminal GFP-tagged monomers are attached to 860-nm diameter GFP-antibody coated beads from their tail.* ***d,*** *Velocities of the beads driven by Dyn and DynRK+7hep monomers. n = 29 and 24 from left to right from three independent measurements ($p < 0.001$). In b and d, the center line and edges represent mean and 5%-95%, respectively.*

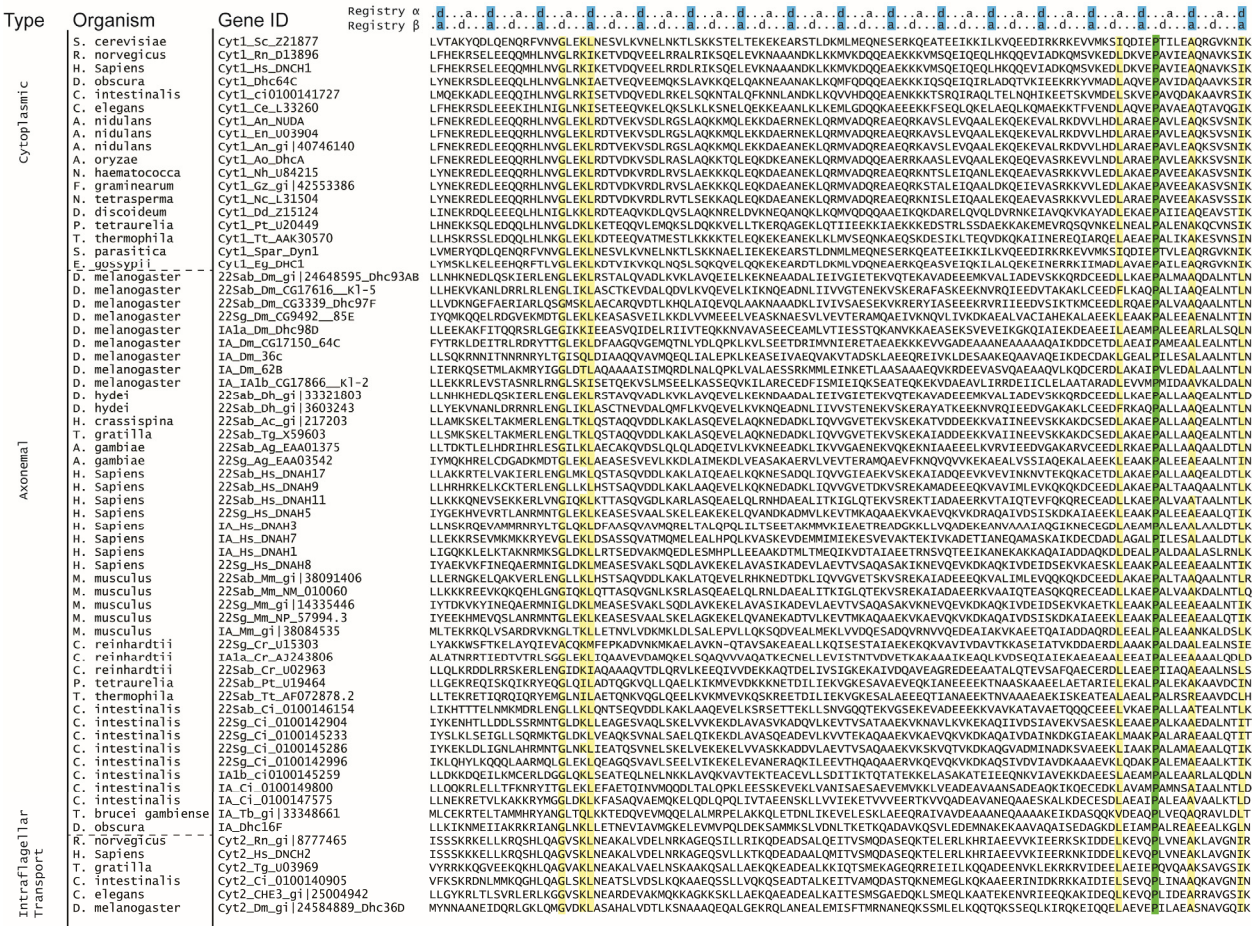

Figure 18: Alignment of the stalk region in 67 dynein heavy chains. a*, Alignment of CC1 sequences. The sequences are oriented from N-terminus to C terminus in these alignments. Isoforms of dynein used in the alignment were grouped based on the type and the organism (cytoplasmic (cyt1), axonemal outer arm (22Sab, 22Sg), axonemal inner arm (IA) and intra-flagellar transport (cyt2) dyneins). α and β registry of the stalk coiled coils are shown on top. Stalk length is conserved among dyneins. Fully conserved proline residues at the base of MTBD that cause tilting of the stalk coiled-coils towards the MT plus-end are highlighted in green. Other residues that are conserved over 90% are highlighted in yellow.*

Discussion

In this study, we successfully directed dynein motility leftward, rightward and backward by altering the direction of LSV. Two critical features of dynein's stalk, the length of its antiparallel coiled-coils and the sharp angle it makes relative to the MT, direct LSV in a plane parallel to the MT towards the minus-end. Both of these features are fully conserved in cytoplasmic and ciliary dyneins across species[104] (Figure 18, Figure 19**Error! Reference source not found.**), suggesting that all dyneins are minus-end directed motors. Inner-arm dyneins typically have additional proline residues in their stalk, which may alter the LSV for generating the ciliary waveform[76].

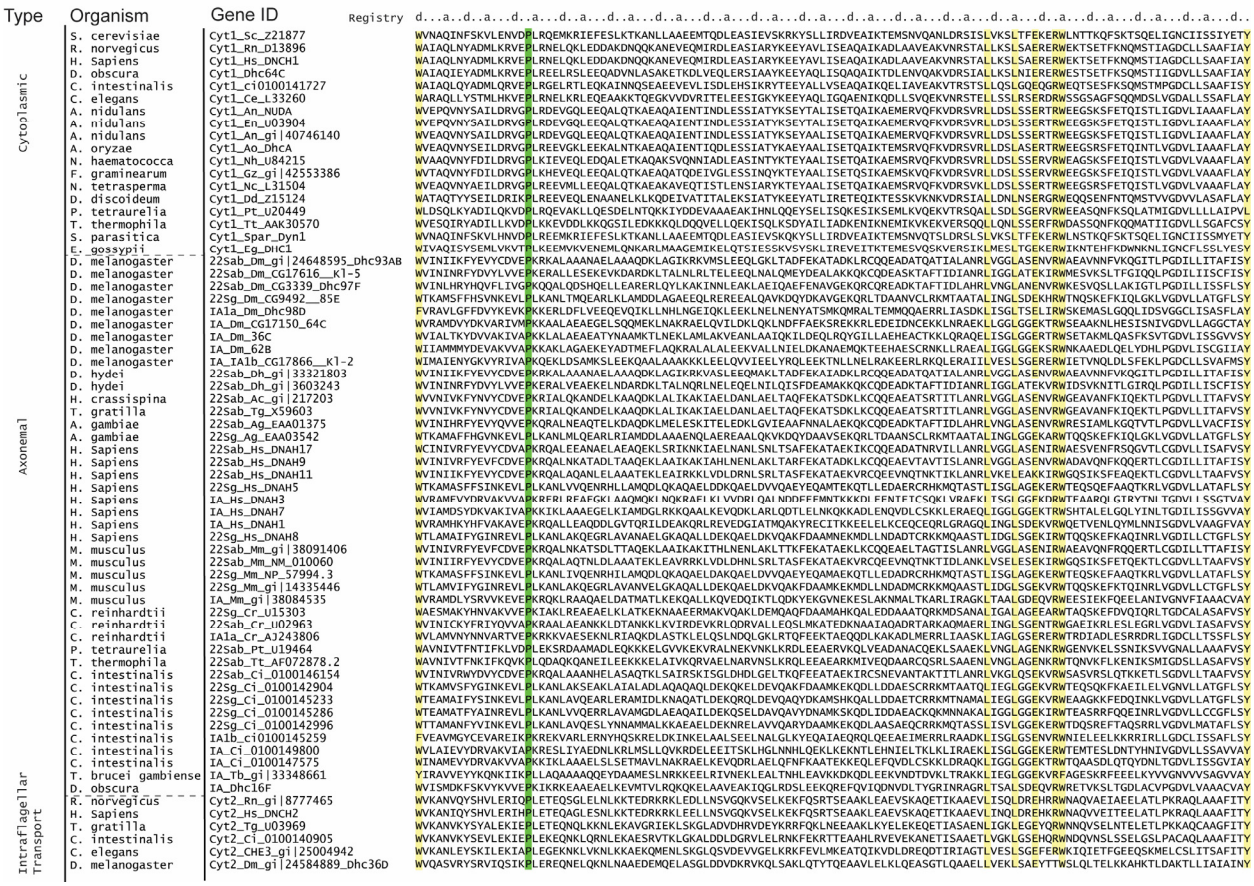

Figure 19: Alignment of the stalk region in 67 dynein heavy chains. a*, Alignment of CC2 sequences. The sequences are oriented from N-terminus to C terminus in these alignments. Isoforms of dynein used in the alignment were grouped based on the type and the organism (cytoplasmic (cyt1), axonemal outer arm (22Sab, 22Sg), axonemal inner arm (IA) and intra-flagellar transport (cyt2) dyneins). α and β registry of the stalk coiled coils are shown on top. Stalk length is conserved among dyneins. Fully conserved proline residues at the base of MTBD that cause tilting of the stalk coiled-coils towards the MT plus-end are highlighted in green. Other residues that are conserved over 90% are highlighted in yellow.*

Which step of the mechanochemical cycle provides a net bias for unidirectional motility? Because dynein heads step independent of each other[62, 63], a single head of a dynein dimer must be able to release from MT, move forward and rebind MT without a need for pulling or pushing of its partner head[62, 73]. We propose that the stepping head remains tethered to its MT-bound partner from the linker after it releases from MT, and the priming stroke of its linker provides a minus-end directed bias when it searches for a new tubulin site. After the head rebinds to MT, the powerstroke of its linker pulls the cargo towards the minus-end[52, 97]. This tethered excursion mechanism is fundamentally distinct from the directionality of kinesin-1 and myosin V, in which the powerstroke of the head in the leading position pulls the lagging head forward[54]

Methods

Construct Design, Protein Expression, and Labeling

An N-terminal truncated *S. cerevisiae* cytoplasmic dynein gene (*DYN1*) encoding amino acids 1219–4093 (predicted molecular weight 331 kD, referred to as Dyn) was used as a template for mutagenesis. Constructs were prepared by gene synthesis of the stalk region. DNA fragments were inserted into the genome of haploid yeast cells by homologous recombination to replace a URA3 cassette (Extended Data Fig. 2). A ZZ affinity tag and a TEV protease cleavage site were inserted to the N-terminus for purification and a DHA tag was inserted at the N- or C-termini for labeling (Extended Data Table 2)[64]. The constructs were purified by binding the cell lysate to IgG beads and cleaving the protein from the beads with Tev protease[64]. Motors were labeled with 10 μM fluorescent dyes functionalized with alkyl chloride when bound to IgG beads and the excess dye was removed before Tev cleavage.

EM Sample Preparation

Lyophilized porcine brain tubulin (Cytoskeleton) was resuspended to 10 mg ml^{-1} in MES-MT buffer (30 mM MES pH 6.5, 70 mM NaCl, 1 mM $MgCl_2$, 1 mM DTT) and aliquoted. For polymerization, aliquots were diluted 2-fold in MES-MT buffer supplemented with 6 mM GTP (Sigma), followed by incubation at 37 °C for 90 min. A further 2-fold dilution in MES-MT buffer supplemented with 20 μM taxol was made, and the MTs were left at room temperature overnight. Monomeric Dyn or $Dyn_{RK+7hep}$ was diluted 5-fold into cold BRB10 (10 mM PIPES pH7.0, 1 mM EGTA, 1 mM $MgCl_2$, 1 mM DTT, 0.1% Tween-20), and concentrated to the original volume in an Amicon 100 MWCO 0.5 ml centrifugal concentrator. Complete buffer exchange was achieved through two further cycles of dilution and concentration, resulting in a total dilution factor of 125. MTs were pelleted at 20,000 rcf for 10 min and resuspended in room temperature BRB10. 3 min prior to grid freezing, a mixture containing 1 μM MT and 150 nM dynein was made up in room temperature BRB10. 4 μL of this sample was applied to Quantifoil Au300 R1.2/1.3 grids held in a FEI Vitrobot III chamber set to 100% humidity, 22°C. Following 4-4.5 s blotting, the grid was plunged into liquid ethane and stored in liquid nitrogen until imaging.

EM Imaging and Data Analysis

Grids were loaded into a Gatan 626 cryo-holder and imaged in an FEI F20 TEM operating at 200 kV, equipped with a Falcon II detector reading out a single integrated average. Images were semi-automatically acquired with EPU, at a defocus of -4 μm, a flux of 50 e $Å^{-2}$ s^{-1}, an exposure of 1.5 s and a pixel size of 2.06 $Å^2$. Analysis of dynein on MTs was performed as described previously[98]. Contrast transfer function was determined using GCTF, and micrographs were phase-flipped accordingly in Relion. MT polarity was determined in FIJI (Extended Fig. 5c-g[105]), and the MTs were boxed out into new images such that their plus-end point towards the right of the image. The MT was duplicated and reflected through the long axis to ensure all unique particles were on the top edge. Monomeric dyneins were picked manually in Relion, centered at the point the stalk reaches the top edge of the MT. Particles were disregarded if the kink at the

base of the stalk was not observed, or if any neighboring particles overlapped. 2D classification into a single class each for Dyn and $Dyn_{RK+7hep}$ aligned the particles to each other. The angle of the stalk relative to the MT long-axis and stalk length was measured for each particle in FIJI (Figure 20).

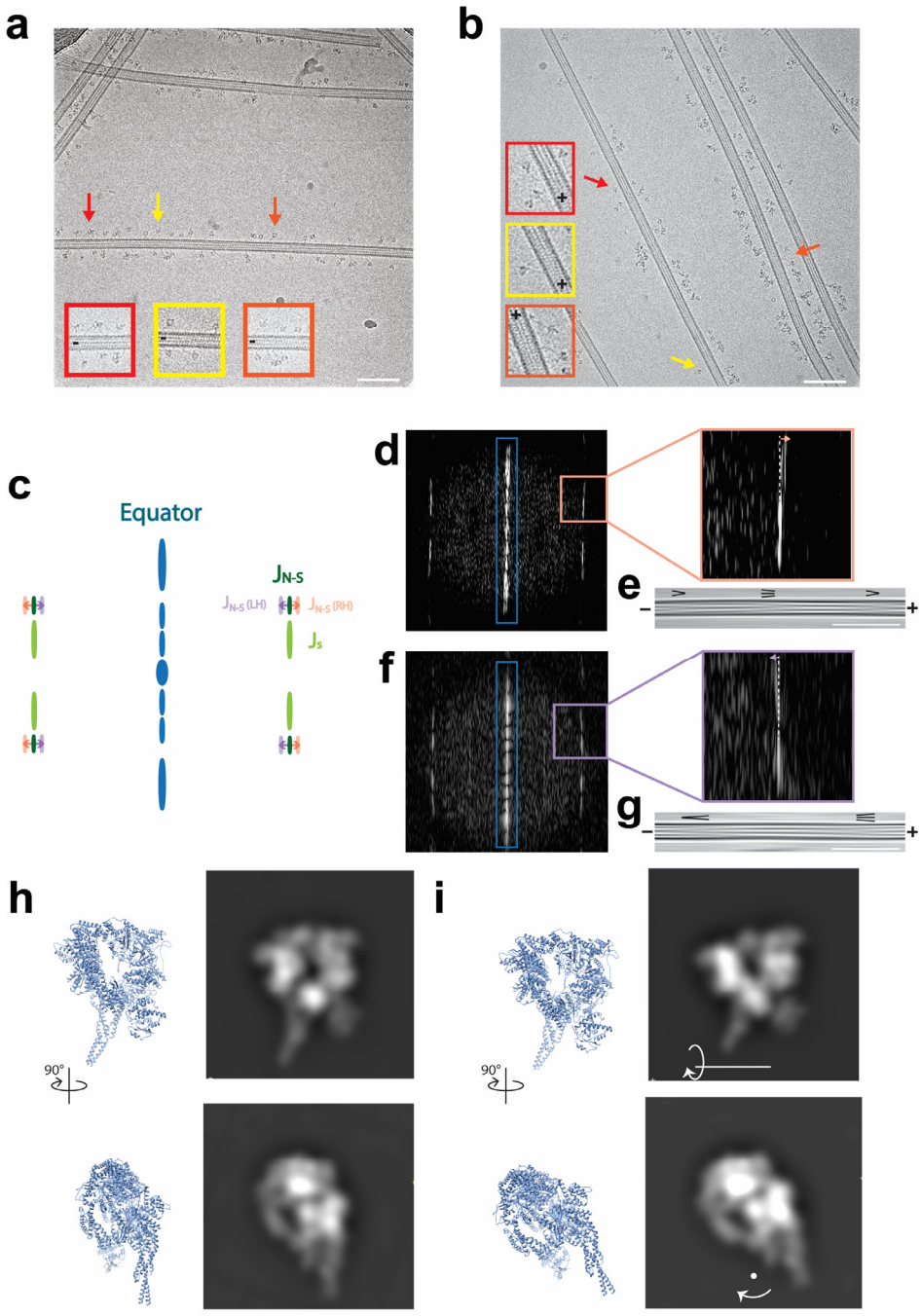

Figure 20: CryoEM image analysis of dynein monomers on MTs. a, *A representative cryoelectron micrograph of Dyn monomers bound to MTs with single monomers indicated with arrows and enlarged*

inset (Scale bar = 100 nm). ***b,*** *A representative cryoelectron micrograph of $Dyn_{RK+7hep}$ monomers bound to MTs with single monomers indicated with arrows and enlarged inset (Scale bar = 100 nm).* ***c,*** *A simplified depiction of the power spectrum of a MT, to demonstrate the method of polarity determination as previously shown[105]. MTs with different numbers of protofilaments have different degrees of protofilament skew around the long-axis. This causes differences in the Moiré patterns produced in cryoEM images. These visual changes result in changes to the position of certain reflections in the MT power spectrum. As a result, right- and left-handed helix architectures can be differentiated by the relative positions of the J_S (light green) and J_{S-N} (dark green) reflections. For right-handed helices, the J_{S-N} (RH, pink) reflection is further from the equator (blue) than the J_S reflection, whereas for left-handed helices the J_{S-N} (LH, purple) reflection is closer to the equator than the J_S reflection. When the MT is Fourier-filtered to only include information from the equator (blue), a characteristic arrowhead pattern is formed from the Moiré patterns. For right-handed helix architectures, this points towards the plus-end, and for left-handed helix architectures, this points towards the minus-end.* ***d,*** *An example power spectrum of an MT determined to be a right handed-helix. Enlargement on the right shows that the J_S reflection is closer to the equator than the J_{S-N} reflection.* ***e,*** *A Fourier-filtered image produced from the equatorial reflections from the power spectrum in d (blue box). For right-handed helix architectures, the arrowheads point towards the plus end (Scale bar = 100 nm).* ***f,*** *An example power spectrum of an MT determined to be a left handed-helix. Enlargement on the right shows that the J_S reflection is further from the equator than the J_{S-N} reflection.* ***g,*** *A Fourier-filtered image produced from the equatorial reflections from the power spectrum in f (blue box). For left-handed helix architectures, the arrowheads point towards the minus end (Scale bar = 100 nm).* ***h,*** *Orthogonal views of an atomic model of a dynein motor in an arrangement corresponding to the "wild-type view", and synthetic projections produced from them. In this arrangement, the motor appears as an even ring.* ***i,*** *As in h, but with the model tilted 30° around the indicated axis. In this arrangement, the projection creates a crescent shape similar to that seen in the $Dyn_{RK+7hep}$ class, albeit with the ring and stalk unflipped, suggesting that the ring of $Dyn_{RK+7hep}$ is slightly tilted in relation to the MT.*

To simulate projections of the motor on a MT the following PDB entries were used: 3VKG[46] (for the stalk) and 4AI6[53] (for the ADP-bound state of the ring and linker). The coordinates were converted into a simulated electron density volume with the EMAN program "pdb2mrc". The volume was bandpass filtered between 30 Å and 500 Å using "bfilter" and projected in different orientations in Relion.

Fluorescence Microscopy

Assays were performed on a custom-built objective-type total internal reflection fluorescence (TIRF) microscope, equipped with Nikon Ti-Eclipse inverted microscope body, the perfect focusing system, and a 1.49 NA 100X oil immersion objective (Nikon). The fluorophores were excited with 488 nm (for GFP and QDs) and 561 nm (for TMR and Cy3) and 633 nm (for Cy5) lasers and the fluorescent signal was detected by the EM-CCD camera (Ixon, Andor) with an effective pixel size of 106 nm. The videos were recorded at 1 Hz. For dual color imaging, fluorescence emission was separated into two channels on a CCD camera using Optosplit II (Cairn) image splitter.

MT-Bridge Assays

Bead motility assays on MT bridges were performed as previously described[100]. Briefly, 2 μm diameter polystyrene beads were coated with an anti-GFP antibody (Covance) using EDC-NHS crosslinking. The beads were incubated with 0.5 μM $SRS_{85:82}$-GFP[85] and excess protein was removed by pelleting the beads. The beads were non-specifically adsorbed to the surface of the

flow chamber and the surface was pre-blocked with 30 µL DLBC (DLB buffer (30 mM HEPES pH 7.4, 1 mM EGTA, 2 mM $MgCl_2$, and 10% glycerol) supplemented with 1 mg ml^{-1} casein). 15 µg ml^{-1} Cy3-labeled MTs were flown into the chamber. After 10 min, unbound MTs were removed by a 30 µL DLBC wash. 0.5 µm diameter anti-GFP antibody-coated beads were incubated on ice with 5-10 nM GFP-dynein for 10 min and flown into the chamber in the imaging buffer. The sample was placed on a brightfield microscope equipped with Nikon Ti-E Eclipse microscope body, a Nikon 100× 1.49 NA oil immersion objective, Nikon 1.4 NA oil condenser and LED white-light illuminator (Sutter). The sample was scanned for a MT bridge that is longer than 10 µm and oscillates less than 2 pixels. Spontaneous attachment of freely diffusing dynein-coated beads and their processive motility along the MT bridges were captured with the CMOS camera (Hamamatsu) at 10 Hz with an effective pixel size of 57 nm. Cargo beads were tracked using a Gaussian fitting algorithm in MATLAB. The helical pitch (λ) was calculated from the periodicity of the x-y projection of the traces between peak to peak positions[100]. The distance between the center of the MT cylinder and pivoting point of dynein's at their linker domain (*r*) was estimated to be 27 nm. The pitch angle was defined as $\tan^{-1}(2\pi r/\lambda)$. The z position of a bead was calibrated by measuring the intensity of surface immobilized 0.5 µm beads while the microscope objective was moved ±250 nm in the z-direction with 25 nm increments using a piezoelectric objective scanner (Physik Instrumente).

Gliding Assays

In order to polarity-mark the MTs, N-ethylmaleimide (NEM) modified tubulin was prepared by mixing 10 mg ml^{-1} unlabeled tubulin (purified from porcine brain[106]) in BRB80 [80 mM PIPES pH 6.8, 1 mM EGTA, 2 mM $MgCl_2$] with 1 mM NEM and 0.5 mM GTP for 10 min on ice. The reaction is quenched with 8 mM β-mercaptoethanol (βME) for 30 min on ice. Brightly labeled MT seeds were polymerized by incubating 0.4 mg ml^{-1} Cy3-labeled tubulin, 0.5 mg ml^{-1} unlabeled tubulin, 1 mM GMP-CPP (Jena BioSciences) and 1 mM DTT in BRB80 for 15 min at 37 °C. 1.5 µl seed was added to a mixture containing 0.1 mg ml^{-1} Cy3-tubulin, 1 mg ml^{-1} unlabeled tubulin, 1 mg ml^{-1} NEM-modified tubulin, 1 mM GTP and 1 mM DTT in BRB80 and incubated at 37 °C. Immediately after mixing, 2 µL of 2 µM, 20 µM, and 200 µM taxol was added with 10 min breaks. After an additional 15 min incubation at 37°C, MTs were pelleted over 300 µL 30% glycerol cushion at 65,000 g for 10 min. The pellet was resuspended in BRB80 with 20 µM taxol and 1 mM DTT and stored in dark at room temperature. Polarity-marked MTs were prepared fresh daily for the gliding assays.

For MT gliding assays[64], rabbit monoclonal anti-GFP antibody (~0.4 mg ml^{-1}, Covance) was flown to an assay chamber and incubated for 5 min. The chamber was washed with 60 µl of buffer DLBCT (DLBC supplemented with 20 µM taxol). 10 µl of 20 nM GFP-tagged motor in DLBCT was added to the chamber. After 3 min incubation, unbound motor was removed by 30 µl DLBCT wash. 10 µL 200 nM freshly polymerized polarity-marked MTs were flown to the chamber and allowed to bind dynein for 2 min. The chamber was washed with 100 µl of DLBCT. 30 µl of imaging buffer (DLBCT supplemented with 2.5 mM PCA (protocatechuic acid), 50 nM PCD (protocatechuate-3,4-dioxygenase) and 1 mM ATP) containing the desired KCl concentration was flown to the chamber.

Single-Molecule Motility Assays

Sea urchin axonemes were immobilized on a glass coverslip in a flow chamber. The chamber was washed with 50 µl DLBC. 200 pM GFP-tagged mutant dynein and TMR-tagged wild-type dynein were added into the chamber in DLBC and allowed to bind MTs for 3 min. The chamber was then washed with 100 µl DLBC and 20 µl imaging buffer. Two fluorescent channels were overlaid, and the velocity and directionality of the constructs were determined with kymograph analysis using ImageJ.

For high resolution tracking assays, 655 nm amine-labeled quantum dots (QDs, Invitrogen) were coated with anti-GFP antibody by using sulfo-SMCC (sulfosuccinimidyl 4-(N-maleimidomethyl) cyclohexane-1-carboxylate) as a cross-linking reagent. 100 nM QD was mixed with 25 µM sulfo-SMCC (~250-fold molar excess) and incubated for 1 h. Excess sulfo-SMCC was removed by using 30k MWCO spin-concentrator with 3 consecutive dilutions into DLB. 0.4 mg ml^{-1} anti-GFP antibodies were reduced with 4 mM TCEP (tris (2-carboxyethyl) phosphine) for 30 min and mixed with QDs. After 1 h, excess antibody was removed by using a spin filter for 3 consecutive dilutions into 25 mM sodium borate buffer pH 8.0 and concentrated to 5 µM for storage. All reactions were performed at room temperature.

5 µM anti-GFP antibody labeled QDs was mixed with 100 nM GFP-tagged dynein with 1:1 ratio and incubated 15 min on ice. Polarity-marked and biotinylated MTs were immobilized on the coverslips using biotinylated-BSA and streptavidin. Dynein-QD mixture was diluted 100-fold and was flown into the chamber. After 3 min incubation, the chamber was washed with 100 µl DLBC and 20 µl imaging buffer containing 5-10 µM ATP. Two fluorescent channels of Cy3-labeled MTs and QDs were overlaid to determine the directionality of the motility at 20 ms temporal resolution. Comparison of the number of GFP versus QD spots that moved along MTs suggested that ~10% of dyneins were labeled with a QD under these conditions.

The QD position was tracked by Fluorescence Imaging with One Nanometer Accuracy (FIONA)[107] using a two-dimensional Gaussian fitting algorithm in ImageJ. Obtained traces were fit using a custom written step finding algorithm with a least-squares minimization[65]. All of the traces were visually checked for the goodness of the fit and manual adjustments were implemented in less than 5% of the analyzed steps.

Optical Trapping Assay

Sea urchin axonemes were immobilized on a glass coverslip in a flow chamber. The chamber was washed with 50 µl DLBC. MT polarity of surface-immobilized axonemes was determined by adding ~2 nM TMR-labeled dynein into the chamber in DLBC with 10 µM ATP, waiting for 4 min to allow accumulation of TMR-dynein at the MT minus end and washing the chamber with 150 µL DLBC supplemented with 0.5 U ml^{-1} apyrase to consume the left-over ATP in the assay chamber[73]. TMR signal on axonemes was visualized with a CMOS camera (Hamamatsu) under 532 nm TIRF excitation. N-terminal GFP tagged motors were mixed with GFP-antibody coated polystyrene beads (0.86 µm diameter, Invitrogen)[100]. The motor-bead mixture was diluted 10-fold in DLBC supplemented with the PCA/PCD oxygen scavenging system and 0.5 U ml^{-1} apyrase and flown into the chamber. The motor:bead ratio was adjusted to a level in which 5-15% of the

trapped beads that are brought near an axoneme bind to within 1 min. >90% of the MT-binding events were terminated with a single release step, indicative of binding of a single dynein monomer to a MT.

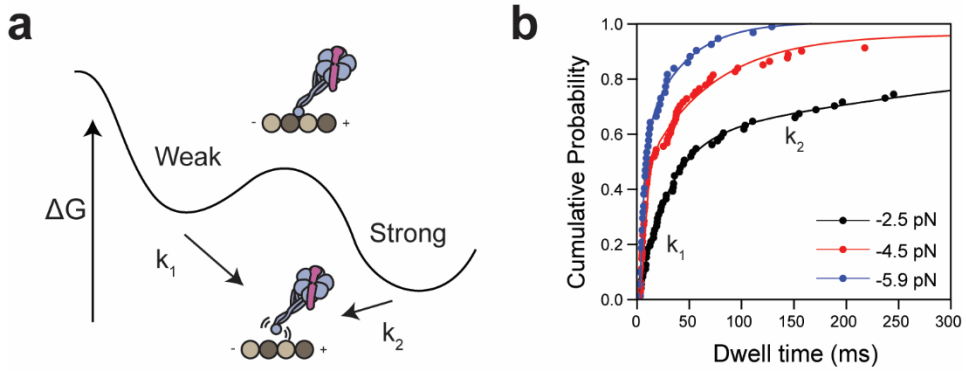

Figure 21: Force-induced release of Dyn and Dyn$_{RK+7hep}$ monomers from MTs. a, *A model of the dynein-MT interaction shows two distinct binding modes in the apo state, with k_1 and k_2 representing force-induced release rates from the weak and strong states, respectively. The slow rate (k_2) represents strong binding of the motor to its tubulin binding site, whereas the fast rate (k_1) represents transient or nonspecific interactions of the motor with the MT.* ***b,*** *Cumulative probability distributions (solid circles) of the MT-bound time of Dyn monomers at given force ranges. The release rates (k_1 and k_2) were calculated by a two-exponential-decay fit (solid curves).* ***c,*** *k_1 of Dyn$_{RK+7hep}$ (red) has similar force-dependence to Dyn (black). Error bars correspond to 5-95% confidence intervals. Each bin contains minimum 50 data points from two independent measurements.*

A custom-built optical trap consisting of a 2 W 1064 nm continuous wave laser (Coherent), a Nikon Ti-Eclipse microscope body and a Nikon 100x 1.49 NA oil immersion objective was used to determine the force-induced release of dynein monomers. The beads were trapped by a ~50 mW 1064 nm laser beam to achieve a spring constant of ~0.05 pN nm^{-1}. The trapping beam was steered by a two-axis acousto-optical deflector (AOD, AA Electronics) to capture floating monodisperse beads, position them over surface-immobilized axonemes and oscillate the bead between two positions (±150 nm) along the long-axis of the axoneme with 0.5 s periodicity. Trap stiffness was calibrated for each sample by fitting the windowed power spectrum of a bead trapped 3 µm above the surface of the coverslip to a Lorentzian curve[108]. A position sensitive detector (PSD, First Sensor) was located at the back focal plane to detect bead displacement. The PSD data was recorded at 20 kHz for calibration and 5 kHz for data acquisition. The PSD response was calibrated by rapidly scanning the laser across a trapped bead in both x and y directions using the AODs and fitting the resulting curve to a cubic polynomial. This calibration was repeated at the surface and 3 µm into the solution to avoid systematic errors in either experimental data or stiffness calibrations. Bead-trap separation was monitored in real time to prevent trap oscillations during a binding event. MT release events were determined with the use of a custom step-finding algorithm written in MATLAB[109]. Dwell times were sorted by applied force and binned. The cumulative distribution function of every bin was calculated and fitted into a two-exponential decay function (Figure 21).

For force-feedback assays, beads were sparsely coated with full-length GFP-Dyn$_{RK+7hep}$ and brought to the proximity of the axonemes. The trap was moved ±500 nm along the length of axonemes. When the bead-trap separation reaches 100 nm after dynein binds to a MT, force-feedback control was activated and trap position was updated at 100 Hz to keep the applied force constant. Trap stiffness was adjusted to exert constant forces between 0.75 and 3 pN. The velocity of the movement was calculated by the slope of the bead trajectories. Runs shorter than 0.6 s were excluded from data analysis.

ATPase Assays

The MT-stimulated ATPase assays were performed using an EnzCheck Phosphate Assay Kit (Life Technologies) and a 96-well plate reader (μQuant, BioTek Instruments). A typical reaction has 2 nM dynein, 200 nM methylthioguanosine, 1 U ml^{-1} purine nucleoside phosphorylase, 2 mM DTT, 1 mM ATP, 0 or 50 mM KCl and varying concentration of taxol-stabilized MTs in DLB. Absorbances at 360 nm were measured with 60 s intervals for 30 min, blanked with buffer only solution and calibrated against a P_i absorbance calibration curve. k_{basal} and k_{cat} were determined by fitting the data to the Michaelis-Menten equation in Origin.

Statistical Analysis

Chi-square test was used to determine the p-values for comparing the backward stepping probability in stepping analysis. Two-sample t-test was used for the rest of the comparisons. All were calculated in Mathworks MATLAB.

Atomic Model Building

The pre-powerstroke conformation of human dynein-2 in the presence of Mg.ADP.Vi (pdb# 4RH7[53]) was selected for the starting point of the Dyn MD simulations. Mutations in the crystal structure were reversed (R1413K, Q2871R and V3680A) with the mutator plugin in VMD. An additional valine residue at the C-terminus was removed. Missing residues (2584A-2586A, 2827T-2846S, 3596V-3611R, and 3954D-3963S) were constructed using VMD's Molefacture Plugin and geometrically optimized via MD simulations to fit the missing regions to obtain structurally complete Dyn. Dyn$_{RK}$ was constructed upon insertions of V2981P, P2983A, P3108A, and E3110P mutations to the Dyn structure. Dyn$_{RK+7hep}$ was modeled by extending residues V2964-V2965 on coiled-coil 1 (CC1) and K3122-T3123 on CC2 using the conformation of residues R2916-V2964 on CC1 and T3123-A3171 on CC2 (see Supplementary methods for details).

Molecular Dynamics Simulations

Each dynein structure was solvated in a water box having at least a 15Å cushion of water in each direction from the exposed atoms. 1 mM $MgCl_2$ and 150 mM KCl were added via the Autoionize Plugin in VMD to neutralize the system. The procedure was repeated for each system to generate non-identical starting conformations. Dyn, Dyn$_{RK}$ and Dyn$_{RK+7hep}$ systems were composed of 781,332, 781,319 and 946,159 atoms, respectively. MD simulations were performed in NAMD 2.11[110] with NVIDIA CUDA acceleration using the CHARMM36 force field[111]. A cutoff distance of 12 Å was used for van der Waals (vdW) interactions, with a switching function starting at 10 Å and reaching zero at 12 Å. Long-range electrostatic forces were computed using the particle-mesh

Ewald method. A time step of 2 fs was used. All simulations were performed under NPT ensemble conditions; temperature and pressure were kept constant at 310 K and 1 atm, respectively. A damping coefficient of 1 ps^{-1} for Langevin dynamics was used to maintain isothermal conditions. Langevin Nosé-Hoover method was performed using an oscillation period of 100 fs and damping time scale of 50 fs to maintain the pressure constant. First, 10,000 steps of minimization followed by 2 ns of equilibration was performed by keeping the protein fixed. Subsequently, the complete system was minimized for an additional 10,000 steps without any constrains/restrains on the protein. The resulting conformer was equilibrated for 6 ns. During the first 2 ns of simulations, harmonic constraints having force constants of 2 kcal mol^{-1} $Å^{-2}$ were applied to the backbone atoms. Three separate MD simulations were performed for Dyn and Dyn_{RK} and one simulation was performed for $Dyn_{RK+7hep}$. Total simulation time was 1.7 µs. Starting conformations for $Dyn_{RK\_1\text{-}3}$ were constructed based on the final conformations of $Dyn_{1\text{-}3}$ simulations. Similarly, $Dyn_{RK+7hep}$ was modeled based on the final conformations obtained in Dyn_1 simulation. The conformations of Dyn_{+3hep} were estimated by elongating each MD conformation of Dyn with the conformation of residues R2916-V2964 between V2964-V2965 on CC1 and with residues T3123-A3171 between K3122-T3123 on CC2. Dyn_{-3hep} conformations were estimated by shortening R2916-V2964 on CC1 and T3123-A3171 on CC2.

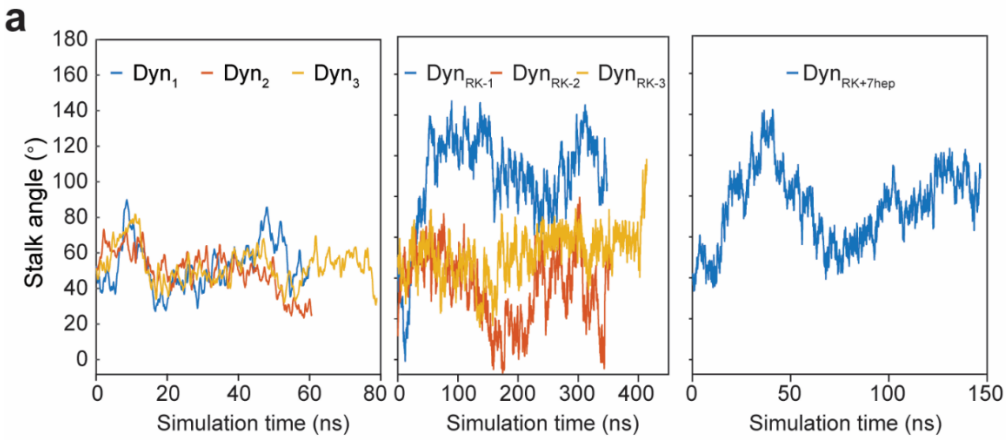

Figure 22: Calculation of stalk and LSV angles by MD simulations. *a, Changes of the stalk angle in three independent MD simulations of Dyn, and DynRK and one simulation of DynRK+7hep. In DynRK-1 and DynRK-3 simulations, the stalk angle sharply increases around 50 ns and 400 ns, respectively and remains pointed towards the minus-end after its reversal. 180° represents tilting of the stalk towards the minus end*

Stalk Angle Calculations

The dynein crystal structure (pdb# 4RH7[53]) and each of the Dyn, Dyn_{RK} and $Dyn_{RK+7hep}$ conformations sampled during MD simulations were docked onto tubulin by aligning with the alpha carbon atoms of the MT-MTBD contact residues in the high-affinity *M. musculus* dynein MTBD - tubulin complex (pdb# 3J1T[101]); corresponding to residues L3300-D3307, A3313-I3325, E3333-R3341 and P3377-A3383 in 3J1T and E2998-S3005, D3011-L3023, W3031-A3039, P3076-A3082 in 4RH7. Principal axes (PA) of MT was obtained via the orient tool in VMD. PA1 (longitudinal axis) corresponds to the longitudinal axis of tubulin. PA2 (radial axis) passes through the center of mass of the Q2982 and Q3098 alpha carbons at the stalk-MTBD intersection of 4RH7

(Figure 22). PA3 (tangential axis) is perpendicular to PA1 and PA2. The stalk vector (pointing from S3248 alpha carbon to S3100 alpha carbon) was projected on the plane constructed by PA1 and PA2. The angle between the projected vector and PA2 was defined as stalk angle.

LSV Angle Calculations

The post-powerstroke conformation of the linker of *Dictyostelium discoideum* cytoplasmic dynein (pdb# 3VKG[46]) was superimposed onto MD conformers by aligning CC2 between the residues V3174-L3214 on both conformations. LSV was defined as the displacement vector between the alpha carbon atoms of the N-terminus residue V1258 of the pre-powerstroke conformer and A1526 of the post-powerstroke conformation. Dynein-tubulin complexes were superimposed onto the MT structure (pdb# 5SYF[103]) by aligning alpha carbon atoms of the tubulin α-1B chain. PA1 (longitudinal axis) of LSV corresponds to the longitudinal axis of the MT. PA2 (radial axis) is perpendicular to PA1 and passes through the alpha carbon of V1258 of pdb# 4RH7. PA3 (tangential axis) is perpendicular to both PA1 and PA2. LSV was projected onto the plane defined by PA1 and PA3, and the angle that the projected vector makes with PA1 was defined as the LSV angle.

Kinesin's Front Head is Gated by the Backward Orientation of its Neck Linker

During my studies in the Yildiz Lab, I have learned the cutting-edge single molecule techniques that are applicable to a wide variety of problems. Especially optical trapping and fluorescent imaging are indispensable techniques for the study of motor proteins. Considering the common features of motor protein motility and force generation, even though my focus was on the mechanism of dynein motility, I have collaborated with other members in the lab to work on the kinesin gating mechanism for stepping. The work presented in this chapter was published on: Kinesin's Front Head is Gated by the Orientation of its Neck Linker written by Yusra Satoglu-Dogan*, **Sinan Can***, Frank B. Cleary, Vedud Purde and Ahmet Yildiz. (* equal contribution, Cell Reports, 2015) and the methods used in the study are published as a book chapter on: Measurement of Force-Dependent Release Rates of Cytoskeletal Motors. Optical Tweezers: Methods and Protocols, edited by A. Gennerich, written by **Sinan Can**, Ahmet Yildiz. (Methods in Molecular Biology**,** 2017)

Abstract

Kinesin-1 is a two-headed motor that takes processive 8-nm hand-over-hand steps and transports intracellular cargos towards the plus-end of microtubules. Processive motility requires a gating mechanism to coordinate the mechanochemical cycles of the two heads. Kinesin gating involves the neck-linker (NL), a short peptide that interconnects the heads, but it remains unclear whether gating is facilitated by NL orientation or tension. Using optical trapping, we measured the force-dependent microtubule release rate of kinesin monomers under different nucleotide conditions and pulling geometries. We found that pulling NL in the backward direction inhibits nucleotide binding and subsequent release from the microtubule. This inhibition was independent from the magnitude of tension (2-8 pN) exerted on NL. Our results provide evidence that the front head of a kinesin dimer is gated by the backward orientation of its NL until the rear head releases from the microtubule.

Introduction

Motor proteins play crucial roles in cargo transport, organelle positioning, and cell division by generating force and motility along cytoskeletal tracks[5, 48, 112]. A comprehensive understanding of these major cellular functions requires a detailed understanding of the molecular mechanisms of individual motors' motility and force generation *in vitro*. Optical trapping studies have had a tremendous impact in the cytoskeletal motor field by determining the piconewton forces and nanometer-scale displacements that molecular motors generate along their associated filaments. Optical tweezers have the capability to apply calibrated forces to specific domains of a motor and put different geometrical constraints on a motor's conformation for a deeper understanding of its mode of action.

One of the pressing questions in the motor field is how a dimeric motor can walk processively without dissociating from its track[113, 114]. Recent studies have shown that the mechano-chemical cycles of the motor domains (heads) of kinesin-1 are highly coordinated through 14-amino acid long "neck linkers" (NL) that interconnect the two heads[57, 59, 115]. The NL of the front and rear heads create the required asymmetry to coordinate the movement of the two heads in a two-head-bound state[116, 117]. In this state, the NL of the front head is pointed backward and the NL of the rear head is pointed toward the motor's natural direction of motion (Figure 23). In addition, the NL has been proposed to function as a tension sensor for communication between the heads[118].

To investigate the NL's role in the coordination of motor movement, it is essential to mimic the NL orientation of a head in front and rear positions of the dimer. Here we discuss an optical trapping approach that points NL in a particular direction and exerts different amounts of force on NL of a single head[73] (Figure 24a,b). Kinesin monomers are attached to micron-sized polystyrene beads via a DNA handle connected to the C-terminal end of NL[70]. The beads are then moved ±150 nm between two positions above the microtubule track in a square wave pattern. When a monomer binds to the MT, the bead is unable to follow the trap to the next position. In this state, the trap exerts a constant force on the motor, the magnitude of which depends only on the bead-trap separation until the motor releases from the MT. The assay directly measures the release rate of a head over a large range of forces (0.5-12 pN) exerted toward either the plus or minus end of the MT. MT residence times as short as 1 millisecond can be reliably detected.

Previously, several approaches have been developed to measure motor rupture-forces. These assays apply linearly increasing forces to the motor and measure loading rate-dependent unbinding forces. These rupture force measurements can be transformed into force-dependent release rates by using theoretical models[119]. Our constant-load assay allows direct measurement of motor-filament unbinding rates as a function of force. Because a motor can, in principle, bind any available tubulin binding site when the bead is moved back and forth between the two user-defined positions, the release rate of a motor can be measured for the entire force range in a single experiment without adjusting the parameters of the assay. This "constant load" assay also represents the situation in a walking dimeric motor where the heads are likely to experience a constant force before releasing from the MT.

Using our square wave unbinding experiment, we measured the force-dependent release rates of kinesin monomers from MTs under different nucleotide conditions and pulling geometries to decipher the underlying principles of how NL facilitates the motor's coordinated motility. We found that pulling NL in the backward direction inhibits nucleotide binding and subsequent release from the MT. This inhibition was independent of the magnitude of tension (2-8 pN) exerted on NL. Our results provide evidence that the front head of a kinesin dimer is gated by the backward orientation of its NL until the rear head releases from the microtubule. Similar approaches have also been used to study force-dependent release properties of myosin[120] and dynein motors[73, 74].

Results

Force-dependent release rate of kinesin from MTs

To test the predictions of the front and rear head gating models, we pull on the NL to mimic its orientations in the front and rear head positions using an optical trap. Polystyrene beads sparsely were coated with human kinesin monomers truncated at the C-terminus of the NL (hK349). To label kinesin at the head, we used a cysteine-light kinesin construct, with a single cysteine introduced at E215C [121]. This surface-exposed residue was chosen for DNA attachment because it is positioned away from the NL, ATP binding cleft and MT binding surface, and E215C mutation has no detectable effect on kinesin speed, stepping pattern and force production. The 74 basepair DNA tether was covalently linked to a surface-exposed cysteine [70]. Kinesin was labeled with a DNA tether at NL by fusing a HaloTag, a 26 kDa protein tag, to the C-terminus of hK349 (Experimental Procedures). 15% of kinesin motors were labeled with a DNA tether in our reaction conditions. The other end of the DNA tether was functionalized with biotin and attached to streptavidin-coated polystyrene beads.

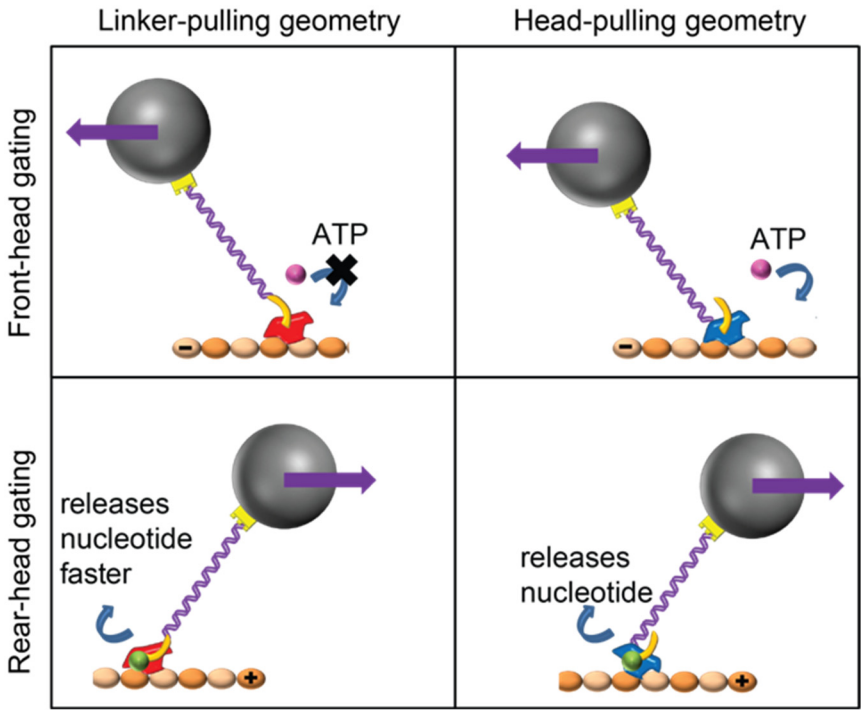

Figure 23: Gating models for kinesin. *In the front-head-gating model, kinesin cannot bind to a nucleotide when its NL is forced to orient backward. This state is mimicked by attaching a DNA tether to a kinesin NL, pulling monomers toward the MT minus end in the presence of ADP. When pulled through the head domain, the NL is free and the monomer is allowed to bind nucleotide. The rear-head-gating model suggests that nucleotide hydrolysis of a MT-bound head accelerates when NL is oriented forward. This state is mimicked by pulling the NL of kinesin monomers towards the plus end in the presence of ATP. When pulled from the head, NL is free and monomers are not expected to hydrolyze the bound ATP faster.*

The MT release rate of a head was measured under variable forces and nucleotide conditions. Motor-coated beads were moved ±125 nm in a square wave pattern on polarity marked MTs (Figure 24c)[73]. When a single kinesin monomer was bound to the MT, it restricted the movement of the bead to a new position of the trap. As a result, the trap exerted forces ranging from 0.5 pN to 10 pN on the motor as a function of the bead-trap separation, until it released from the MT. Previous kinesin rupture force measurements were performed by moving a trapped bead along MTs under constantly-increasing force[122]. Our assay better represents the situation in a kinesin dimer, where the heads are under constant tension in 2HB state before MT release.

To calculate the force-dependent release rate of kinesin monomers, MT dwell time data were sorted by an applied force. We defined positive and negative forces as forces assisting and opposing kinesin's natural direction of motion (plus end), respectively. Cumulative frequency distributions of 200 dwells in a given force range were fitted by two exponential decays. The data could not be fitted well with a single exponential decay ($p < 0.001$, F-test). The MT release rates were defined as the decay constants of the fit (k_1 and k_2). The results support a conventional model that kinesin has strong and weak binding modes to MT surface and indicate that k_1 and k_2 represent force-induced exit from these weak and strong binding states, respectively (Figure 24d,e).

We first established baseline release rates by pulling kinesin monomers under the nucleotide-free (apo) state. A kinesin motor has strong affinity to MT in the apo state. Figure 25a shows that linker-pulled kinesins have similar release properties to those of head-pulled kinesins in the apo state. k_1 was an order of magnitude faster than k_2, and represented ~60-80% of the release events under a wide range of applied forces (Figure 26). In both head- and linker-pulled kinesin, k_1, and k_2 approached to 0 s^{-1} at low forces (±1.4 pN) and increased gradually with load in both forward (MT plus end) and backward (MT minus end) directions. At high forces, k_1 and k_2 were on the order of 100 s^{-1} and 10 s^{-1}, respectively. Release under positive forces was ~20% faster through a wide range of applied forces, consistent with a weak net preference to release towards its natural direction of motion (plus-end) under load[123]. This is in contrast to cytoplasmic dynein, which prefers to release towards the minus-end in a force-dependent manner, while the release towards the plus end is slow and force-independent[73].

Tension on the NL is not critical for nucleotide hydrolysis

We next tested gating models based on the NL orientation and tension by pulling monomers from the NL and the head under different nucleotide conditions. To test the rear-head-gating model, we measured release rates at saturating (1 mM) ATP. Under this condition, kinesin can release from MT due to tension exerted by the trap either in the apo state or in different nucleotide states following the hydrolysis of the bound ATP. If ATP hydrolysis at the rear head is accelerated in a 2HB state[124], kinesin monomers would release faster when NL is pulled in the forward direction. Figure 25b shows that ATP addition leads to an increase in both k_1 and k_2. Force-dependent increase in k_1 and k_2 is steeper in ATP compared to the apo condition, because force accelerates the detachment of kinesin from MT in nucleotide-bound states. At high (2-8 pN) forces, k_2 was ~2-fold faster than that of apo condition and its force-dependent increase was symmetric between

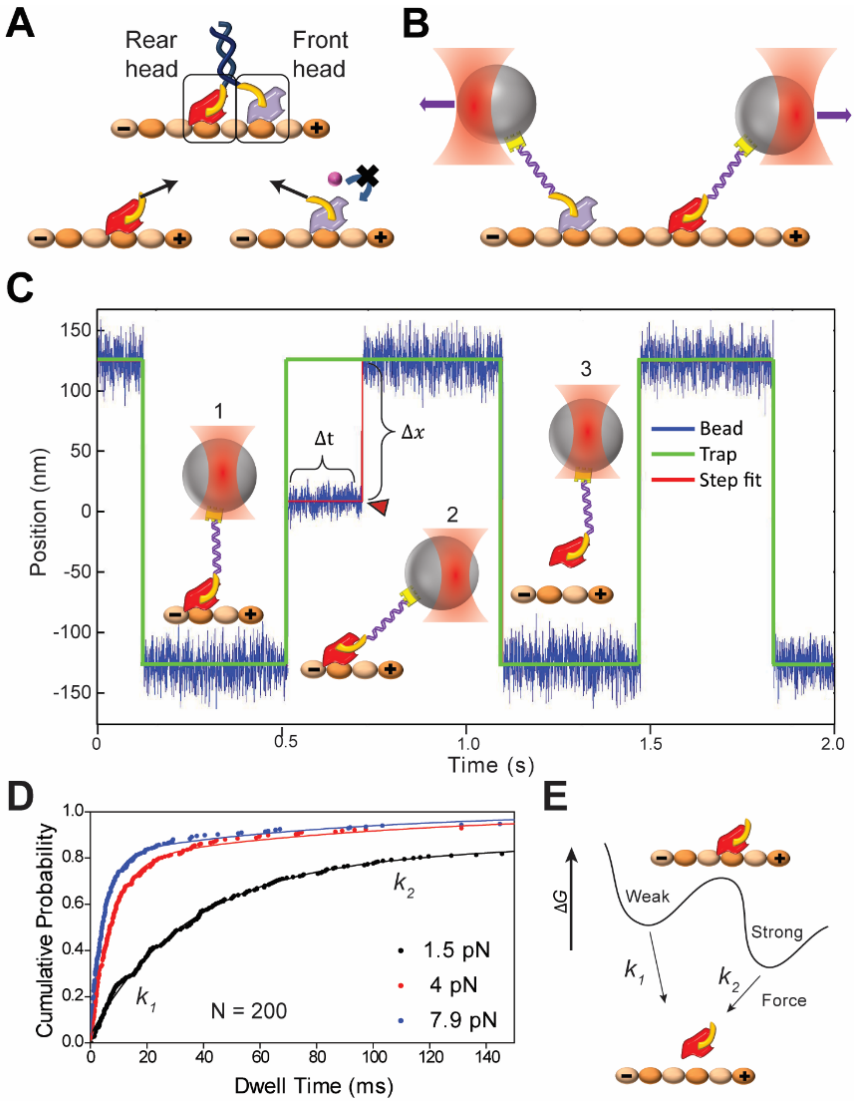

Figure 24: Force-dependent release of kinesin from MTs. ***(A)*** *(Top) Schematic of a kinesin dimer in a 2HB state. The NL (yellow) of the front head is oriented backward and that of the rear head is oriented forward. (Bottom) The orientation of the NLs or tension between them (black arrows) may prevent ATP binding to the front head, or accelerate the nucleotide hydrolysis and subsequent MT release of the rear head to facilitate coordinated movement.* ***(B)*** *NL orientation of the front and rear heads can be mimicked by pulling a kinesin monomer from its NL with an optical trap. Monomers are attached to a large polystyrene bead via short DNA tether through the N-terminal linker (not to scale).* ***(C)*** *A trapped bead is oscillated between two positions 250 nm apart along the MT long axis. (1) When a monomer binds to the MT, (2) the movement of the bead to the next trap position is restricted. In this state, the trap exerts a constant force as a function of bead-trap separation (Δx) on the motor until it releases from the MT (Δt). (3) When the monomer releases from the MT (red arrowhead), the bead resumes following the trap.* ***(D)*** *Cumulative frequency distributions (solid circles) represent the dwell time data for kinesin monomers pulled from the head towards the plus end in the absence of nucleotide at different force ranges. N = 200 for each histogram. The release rates (k_1 and k_2) at a given force range were calculated by two-exponential fits (solid curves) to the dwell time histogram.* ***(E)*** *Model of kinesin-MT interaction shows two distinct binding modes in the apo state. k_1 and k_2 are force-induced release rates from the weak and strong states, respectively.*

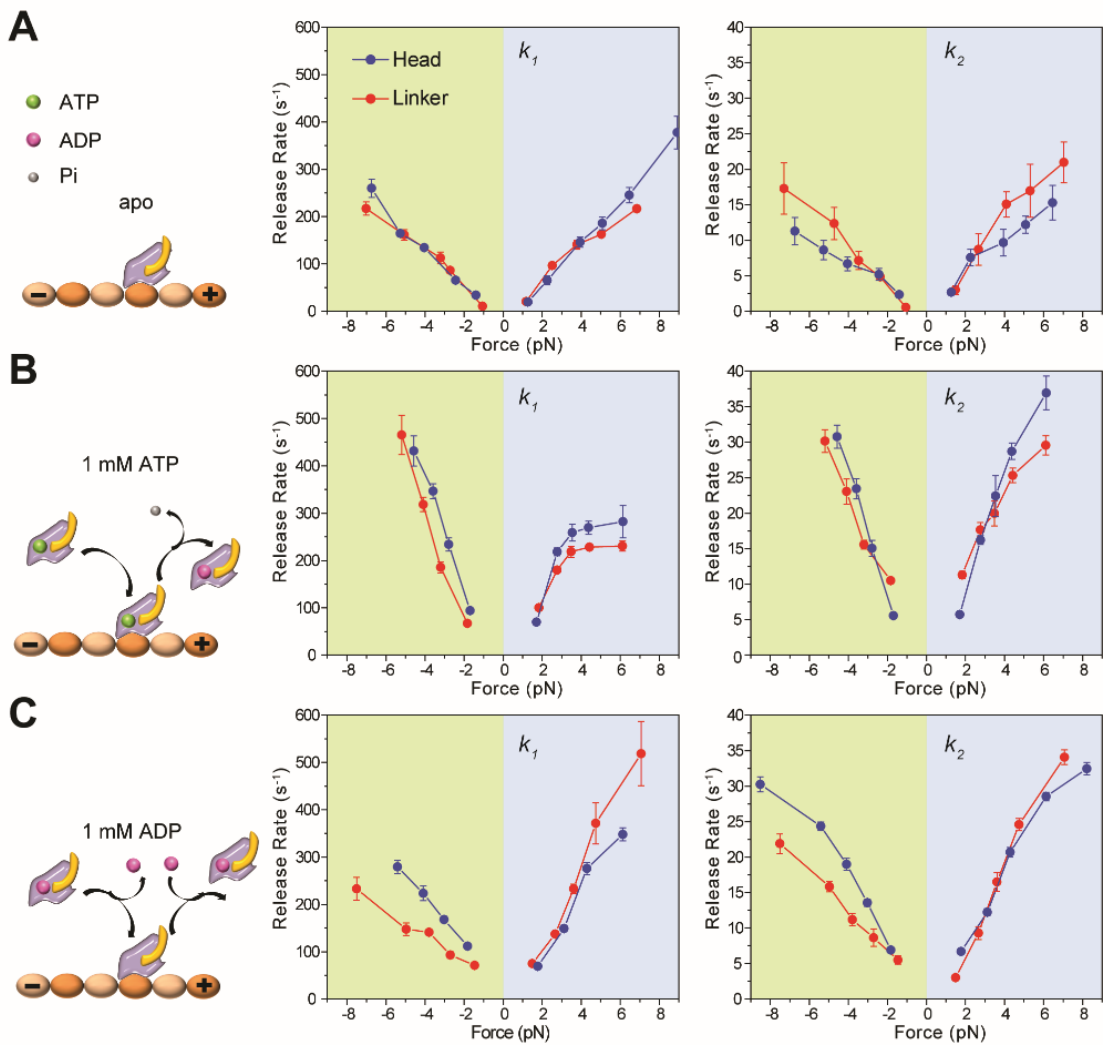

Figure 25: MT release rates of head- and linker-pulled kinesins under different nucleotide conditions. ***(A)*** *Without nucleotide, monomers release in response to external force (left). MT release rates (k_1: middle and k_2: right) of kinesin monomers pulled from the head and linker increases with force in both forward (positive forces) and backward directions.* ***(B)*** *With 1 mM ATP in solution, kinesin can release by force or hydrolysis of the bound nucleotide (left). MT release rates of the head- and linker-pulled kinesins increase several folds compared to the apo condition.* ***(C)*** *At 1 mM ADP, kinesin can release from MTs by force or ADP binding (left). Kinesins pulled from the linker show slower release under backward forces. Error bars represent 95% confidence intervals.*

positive and negative forces. In comparison, k_1 was also ~2-fold faster than that of apo conditions under negative forces. Linker and head-pulled kinesin have similar release rates and we did not observe linker-pulled kinesins to release faster than head-pulled kinesins under positive forces. These results disfavor the rear head gating model and indicate that nucleotide hydrolysis of the rear head is not accelerated when NL is pulled forward.

Unlike the apo condition, in which k_1 and k_2 were approaching to 0 s^{-1} at low (±1.4 pN) forces, k_1 and k_2 were are accelerated by nucleotide addition in 1 mM ATP. At ±1.5 pN forces, k_1 and k_2 were 60s^{-1} and 5 s^{-1} for head-pulled and 42 s^{-1} and 710 s^{-1} for linker-pulled motors, respectively.

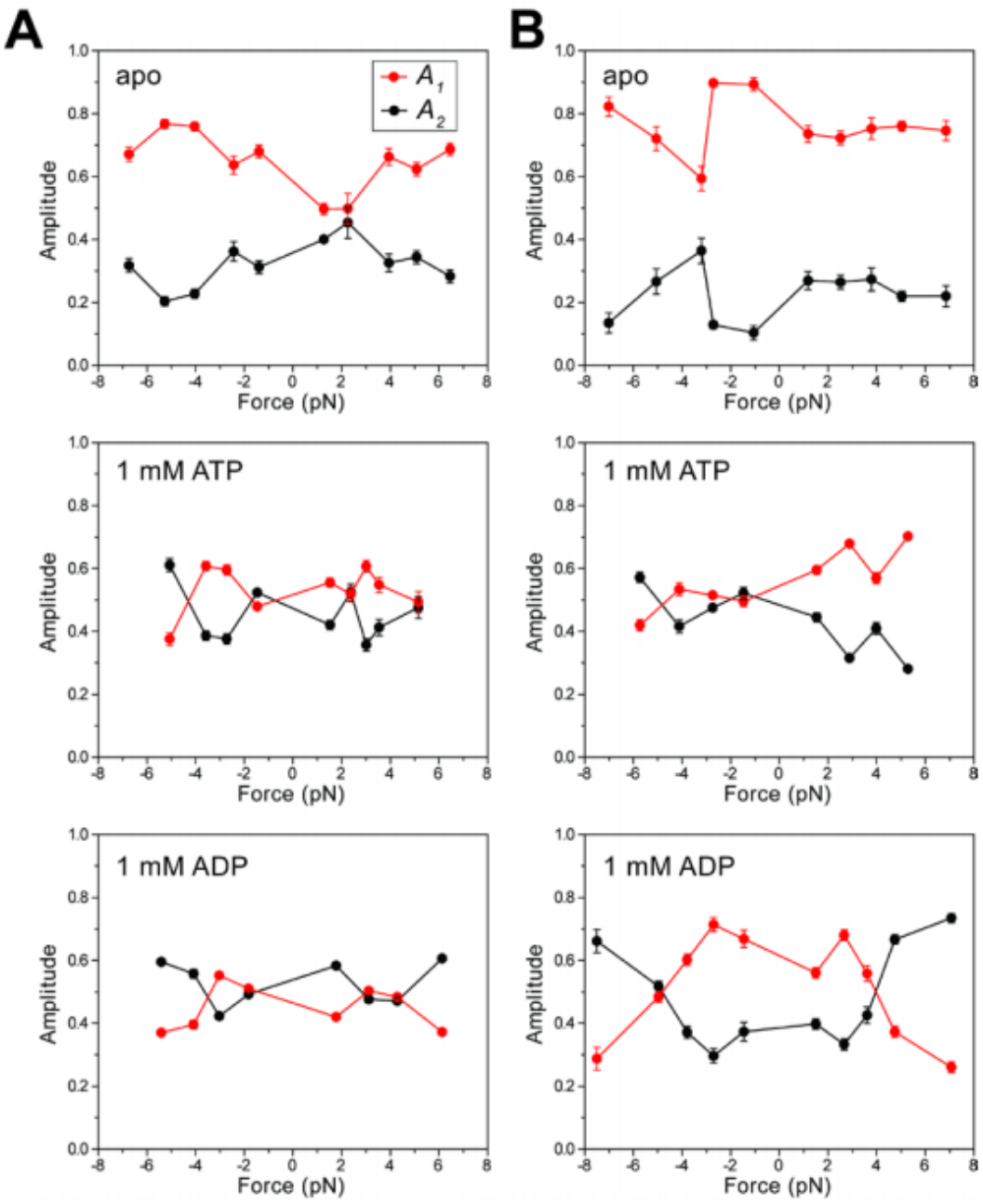

Figure 26: Amplitudes of fast and slowly releasing populations under different nucleotide conditions A) *Amplitudes of fast and slow populations for head-pulled kinesin monomers as a function of applied force. A_1 and A_2 represent the amplitudes of exponential decay with k_1 and k_2 rates, respectively. While A_1 and A_2 are within 30% of each other in ATP and ADP conditions, A_1 is approximately two-fold higher than A_2 in the apo condition.* ***B)*** *Amplitudes of fast and slow populations for linker-pulled kinesin monomers as a function of applied force. A_1 is approximately four-fold higher than A_2 in the apo condition.*

While k_1 values at low forces agree well with rapid (50 s^{-1} in ATP and 70 s^{-1} in ADP) MT detachment measured in bulk, k_2 is more consistent with slow (3-5 s^{-1}) release of the monomer-coated beads from MT in unloaded conditions. The discrepancy between the results of the previous measurements could be explained by the fact that bulk measurements reflect the average release

rate, whereas bead-release assays are unable to detect fast MT-bead interactions due to limited temporal resolution. Unlike apo conditions, fast and slow release events were nearly equal under a wide range of forces (Figure 26), presumably due to the changes in kinesin's affinity to MT as a function of its nucleotide state.

ADP binding is inhibited by backward orientation of the NL

We next tested force-dependent MT release of kinesin monomers from MT in ADP. Kinesin interacts weakly with the MT in the ADP state[123] and an unbound head must release its ADP before MT attachment[125]. Therefore, MT-bound monomers release from the MT either by external tension in the apo state or in the ADP-bound state. Previous unbinding force measurements on a kinesin dimer in ADP conditions indicated that kinesin's affinity for ADP is enhanced by external load exerted on kinesin along the direction of motility and weakened by backward load[126]. However, the nucleotide-binding rate, not the dissociation constant, is critical to the front head gating mechanism, because kinesin is gated at both limited and saturating nucleotide concentrations[57, 127]. In addition, these experiments do not distinguish between ADP binding to the front and rear heads, because the dimers sample both one- and two-heads bound states on a MT in the presence of ADP.

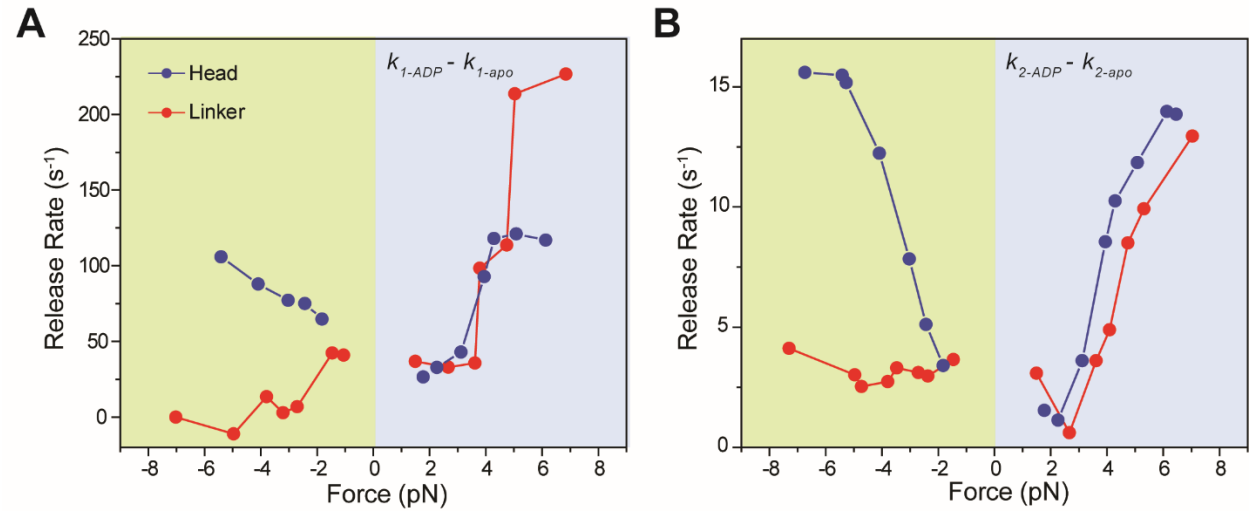

Figure 27: Nucleotide binding to a kinesin head is inhibited when the NL is oriented backward. *Nucleotide-binding induced MT release rates were estimated by subtracting the force-dependent release rates of head- and linker-pulled kinesin monomers under apo conditions from that of 1 mM ADP. Nucleotide-dependent release occurs more slowly when the linker is pulled towards the minus-end (negative forces) relative to the head-pulled motors. The rate of release is nearly independent of the magnitude of tension exerted on the linker when it is pulled towards the minus-end.*

The front-head gating model predicts that a head is unable to bind to a nucleotide when a kinesin monomer is pulled backward from its NL. We measured the effect of nucleotide binding to a kinesin head in both front and rear head orientations of the NL using the trap assay at saturating (1 mM) ADP. In head-pulled kinesins, the addition of 1 mM ADP resulted in a ~1.5 -fold increase in k_1 and k_2 under both positive and negative forces compared to the apo condition (Figure 25c). k_1 and k_2 were 72 s^{-1} and 7 s^{-1}, respectively, at ±1.8 pN. The increase in both rates as a function of applied force was comparable to that of 1 mM ATP (Figure 25b,c). Remarkably, we observed a

clear asymmetry in the release rates when kinesin was pulled from its NL. Under positive forces, both k_1 and k_2 were similar to that of head-pulled motors. However, k_1 and k_2 of linker-pulled motors were significantly lower than of head-pulled motors over a wide range of negative forces.

To estimate the degree to which negative forces exerted on NL slow down the rate of ADP-binding induced MT release, we subtracted k_1 and k_2 values in 1 mM ADP from that of the apo condition (Figure 27). In contrast to the previously proposed enhancement of ADP binding affinity to kinesin under forward load[126], we observed that $k_{1\text{-}ADP} - k_{1\text{-}apo}$ and $k_{2\text{-}ADP} - k_{2\text{-}apo}$ were within 20% to those of the head-pulled condition when NL is pulled forward (Figure 27). Therefore, increase in $k_{1\text{-}ADP} - k_{1\text{-}apo}$ and $k_{2\text{-}ADP} - k_{2\text{-}apo}$ under positive forces are due to the faster release of the motors in the ADP-bound state under increased load, not by increased ADP binding affinity in the forward orientation of NL.

When NL is pulled backward, nucleotide-binding induced release of kinesin occurs at a significantly slower rate than when it is pulled from the head (Figure 27). $k_{1\text{-}ADP} - k_{1\text{-}apo}$ of linker-pulled kinesins was 35 s^{-1} at -1.5 pN, and decreased to 0 ± 25 s^{-1} under higher negative forces. In comparison, $k_{1\text{-}ADP} - k_{1\text{-}apo}$ of head-pulled kinesins was remained constant around 45 s^{-1}. Furthermore, $k_{2\text{-}ADP} - k_{2\text{-}apo}$ of linker-pulled kinesins remained largely constant at 3 s^{-1} from -1.5 pN to -7.3 pN, whereas $k_{2\text{-}ADP} - k_{2\text{-}apo}$ of head-pulled kinesins increased from 3.4 s^{-1} at -1.8 pN to 14.2 s^{-1} at -6.7 pN. We concluded that reduction in nucleotide-binding induced MT release of linker-pulled kinesins is independent on the magnitude of tension between -1.5 to 8 pN.

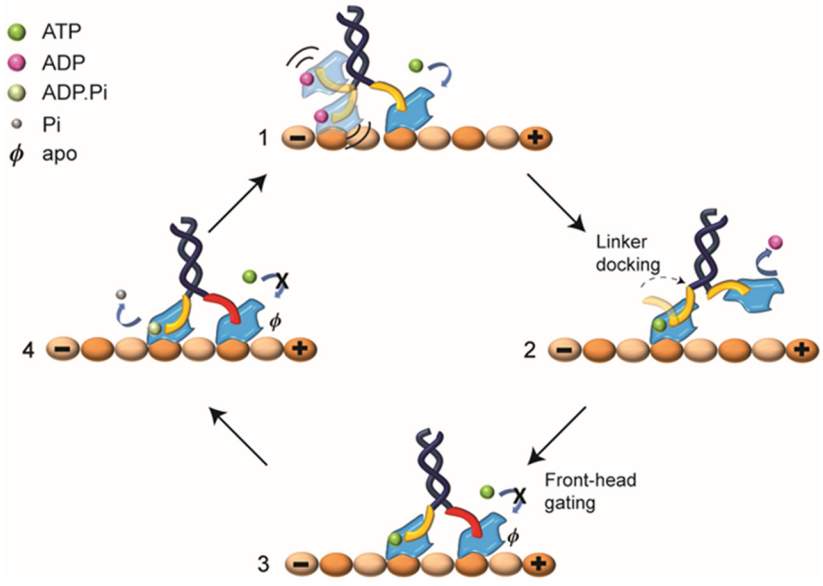

Figure 28: Front head gating model for kinesin. *(1) In the ATP waiting state, the rear head is ADP-bound and weakly interacting with MT. (2) ATP binding to the front head triggers NL docking that pulls the rear head forward. (3) The unbound head releases ADP and rebinds MT ahead of its partner head. (3-4) In 2HB state, the NL of the front head (red) is oriented backward and ATP binding to this head is inhibited until the rear head hydrolyzes ATP and releases from MT.*

Discussion

Our results strongly support the front-head gating model (*Figure 28*) for coordination of the processive motility of a kinesin dimer. When kinesin waits for an ATP molecule, the front head remains tightly attached and the rear head is either weakly interacting with or unbound from the MT. ATP binding to the front head triggers NL docking, moving the rear head towards its next tubulin binding site in the plus-end direction. Kinesin motility is gated when both heads are attached to MT. In this state, NL of the rear head orients forward and is free to dock, but NL of the front head is restricted from docking because it is oriented backward by the trailing head. The rear head remains attached to the MT until it releases the phosphate, which triggers subsequent MT release[128]. This is the rate-limiting step in kinesin's ATPase cycle[129] and the processivity would be ended prematurely if the front head binds and hydrolyzes ATP during this process. As a result, the rear head hydrolyzes ATP and releases the inorganic phosphate while the front head remains strongly attached to the MT. Consistent with this scheme, our results showed that pulling NL in the backward direction greatly reduces the nucleotide-binding induced detachment rate of a head from MT. At high negative forces, $k_{1\text{-ADP}}$–$k_{1\text{-apo}}$ of head-pulled motors was 4-fold faster than that of NL-pulled motors. In addition, $k_{2\text{-ADP}}$–$k_{2\text{-apo}}$ of head-pulled kinesins was at 45 ± 2 s^{-1}, whereas that of NL-pulled kinesins remained constant at 0 ± 5 s^{-1}. The observed reduction in k_1 agrees with the estimation that ATP unbinding to the front head is 6-fold faster than that to the rear head of a walking kinesin dimer.

Kinesin heads experience up to 15 pN tension in a 2HB state[118]. When tension between the heads is reduced by extending NLs, the rear head strongly binds to a MT in the ATP-waiting state[116], and as a result, kinesin loses its ability to convert ATP hydrolysis to a mechanical step and undergoes futile cycles of ATP hydrolysis. While high intramolecular tension is crucial for the energetic efficiency of the kinesin motor, our results showed that it is not critical for the interhead coordination. Nucleotide binding to a head can be inhibited at as low as 2 pN backward tension, and independent of the magnitude of tension exerted on the NL (Figure 27). On the basis of this result, we propose that kinesin gating is facilitated by the backward orientation of NL of the front head. This gating mechanism does not require substantial tension between the heads and is mainly facilitated by restricting NL of the front head to orient backward by the rear head in a 2HB state. Consistent with our model, kinesin maintains its gating mechanism with reduced tension on NLs[116].

A possible clue for how ATP binding to the front head may be suppressed by the inability of its NL to dock onto the catalytic core comes from structural studies[130-132]. The kinesin motor domain contains two hydrophobic pockets on opposite sides, "the switch pocket" and "the docking pocket" that facilitate nucleotide binding and NL docking, respectively[133]. ATP binding to the switch pocket triggers the opening of the docking pocket and leads to NL docking. When the rear head is strongly attached to the MT, it prevents forward extension of the NL of the front head and occupation of its docking pocket. Under this conformation, the switch pocket remains closed and ATP binding to the front head is disfavored because the nucleotide sensing loops cannot interact with γ-phosphate of ATP[133].

Our results have broader implications for how the individual heads of dimeric motors communicate during processive motility. A similar tension sensing mechanism has been proposed to affect

nucleotide binding to catalytic domains of myosin V [134]. In cytoplasmic dynein, the linker domain makes multiple contacts with the catalytic ring and disruption of these contacts significantly reduces the ATPase activity[46, 135]. Tension on the linker domain was shown to gate ATP-dependent MT release[73]. These observations suggest that while the nucleotide hydrolysis of the catalytic core drives the conformational change of a mechanical element (referred to as a lever arm in myosins, a linker in dyneins and an NL in kinesins) to power motility, the asymmetric conformation of these structures in the front and rear heads of a walking dimer plays a major role in achieving processivity.

Methods

Preparation and labeling of kinesin constructs

The plasmid for human kinesin-1 monomers, which contain the first 349 amino acids from the N-terminus (K349) was generously provided by Ronald D. Vale. The construct has the entire motor domain and the neck linker and a short region of the neck coiled coil. In order to label the kinesin head specifically with biotin maleimide (Figure 29), we used cysteine-light kinesin, where all surface exposed cysteines were changed to alanines [130]. We next introduced the E215C mutation for specifically labeling kinesin from its head. To label kinesin at the distal end of the NL, HaloTag (HT, Promega Inc.) was inserted to the C-terminus of K349. Kinesin monomers were expressed in E.coli and purified by affinity chromatography. Active monomers were purified by a MT bind and release assay.

To form a DNA tether, we used 74 base long complementary DNA oligomers. One of the DNA strands has been modified with biotin at the 5'-end and the complementary strand has been modified with a free amine at the 5'-end. The DNA oligos were hybridized and the free amine on the DNA terminus was conjugated to the free sulfhydryl of cysteine by Sulfo-SMCC (Pierce). Biotin at the other end of the duplex DNA was used to attach DNA-tethered kinesin monomer to streptavidin-coated polystyrene beads. For conjugation, 40x excess Sulfo-SMCC was incubated with the DNA solution for 90 minutes at 37 ºC. Excess crosslinker was removed by desalting through G-25 columns. The resulting DNA-SMCC has been mixed with kinesin K349-E215 in 1:1 DNA to kinesin ratio, and reacted 2 hours at 4 ºC.

To label K349-HT monomers with DNA, the free amine at the 5'-end of the DNA tether was conjugated with a 40x excess HT-succinimidyl ester ligand at room temperature for 6 hours. The reaction was quenched by adding 1 mM glycine and excess ligand was removed by desalting through G-25 columns. The resulting DNA-HT ligand was then mixed with K349-HT and reacted for 5 hours at 4˚C.

Biotin at the 5' end was replaced with Cy3 to verify the conjugation of DNA and kinesin. Colocalization of kinesin and Cy3-labeled DNA was confirmed by fluorescence imaging of a denaturing gel, and testing the localization of Cy3-DNA labeled motors on MTs in a total internal reflection fluorescence microscope.

Optical trapping assay

DNA labeled kinesin monomers were diluted between 100,000 to 1,000,000 fold in BRBC (BRB80 with 2.5 mg/ml casein, BRB80 = 80 mM PIPES, 1 mM $MgCl_2$, 1 mM EGTA, pH 6.8). Motors were incubated with streptavidin-coated polystyrene beads (860 nm, Invitrogen) on ice for 10 minutes. The residual ATP in kinesin solution from the purification steps was removed by further diluting the motor-bead mixture in 200 µl of BRBC and pelleting the beads at 13,000 rcf for 90 seconds and discarding the supernatant. The beads were further diluted 10 fold in BRB80, containing a PCD/PCA oxygen scavenging system, 2 mM DTT and 1 mg/ml casein). For no-nucleotide condition, 0.5 U/ml apyrase was added to consume leftover ATP in the chamber. For 1 mM ADP condition, 2 U/ml hexokinase and 0.4% glucose was added to convert leftover ATP to ADP.

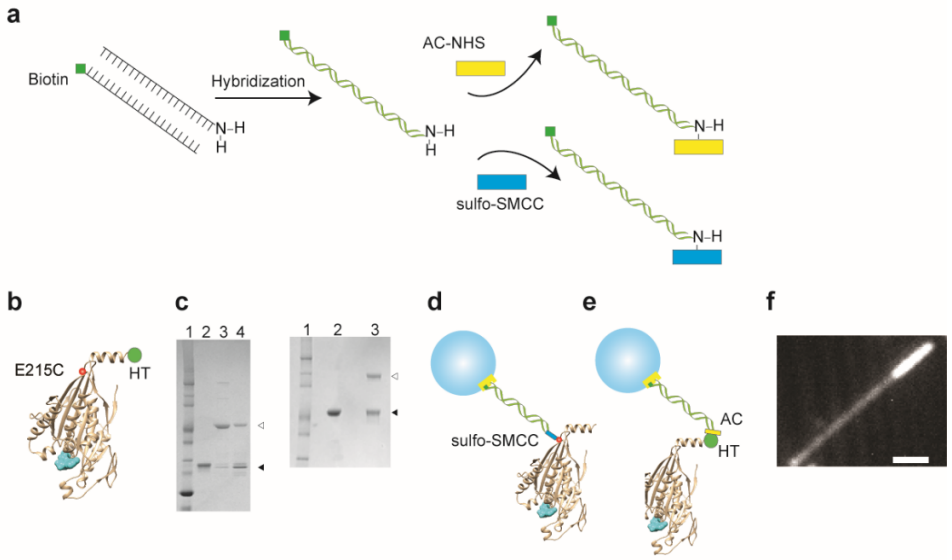

Figure 29: Labeling of human kinesin monomers with a DNA tether at the head and the NL. *(a) Two complementary 74 nt-long ssDNA oligos with functional groups at the 5' end (biotin and amine) are hybridized. The 5'amine group reacts with either a HaloTag ligand (alkyl chloride - AC) or sulfo-SMCC using the NHS chemistry. (b) The atomic structure of rat kinesin monomer in the ADP-bound state (PDB entry 2KIN), numbered as in human kinesin. The protein is truncated at the C-terminus, containing amino acids 1-349 (hK349). A cysteine is introduced at the plus-end tip of the cysteine-light kinesin (E215C, red sphere) for the labeling with sulfo-SMCC. Cyan space-fill represents ADP. (c) hK349 E215C was labeled at the head with the DNA tether functionalized with sulfo-SMCC. (d) To label kinesin at the C-terminus of the NL, a 26 kDa HaloTag was fused to hK349 at the C-terminus (hK349-HT). The HT tag was labeled with the DNA tether functionalized with AC. (e) (Left) A denaturing protein gel shows that hK349-E215C was labeled with the DNA tether. The lanes represent the molecular weight marker (1), kinesin (2), kinesin + Biotinylated DNA (3-4). (Right) hK349-HT was labeled with the DNA tether functionalized with AC. Lanes represent molecular weight marker (1), kinesin (2), kinesin + biotinylated DNA (3). The labeling efficiencies can be calculated from the intensity ratio of labeled (white arrowhead) and unlabeled (black arrowhead) motors. (f) The MT minus end was labeled with Cy5. Polarity marked MTs are used to determine the direction of the release events (scale bar, 2 µm).*

Cy5-labeled sea urchin axonemes were immobilized on a glass surface and washed with 30 µl dynein loading buffer (DLB = 30 mM HEPES, 2 mM $MgCl_2$, 1 mM EDTA, 10% glycerol, pH

7.2). Alexa-488 labeled *S. cerevisiae* cytoplasmic dyneins were diluted in DLBC and introduced into the channel. After one minute of incubation, unbound motors were rinsed with 20 µl DLBC. 20 µl of 20 µM ATP in DBLC was flown in to set dyneins into motion towards the MT minus end where they accumulate and serve as polarity markers. ATP was then rinsed out five times with 20 µl DLBC and once with 30 µl BRBC. The final motor-bead mixture was then added to the sample chamber.

A freely diffusing monodisperse bead was trapped and positioned over an axoneme oriented parallel to detection axis with predetermined MT polarity. The bead was oscillated ±125 nm along the axoneme in a square wave pattern and held for 0.375 seconds in each position. The traces of the bead and trap centers are recorded at 5 kHz. The force exerted on a motor during a binding event is calculated according to trap stiffness and bead-trap separation.

Data Analysis

A graphical overview of the important steps in data analysis is shown in Figure 30.

1. The release of each monomeric head from the MT is a single step process if there is one motor bound. To record data from single monomers, motors are diluted to a level where the probability of motor binding to MTs is reduced to 5–15% during the oscillation of the beads. Under these conditions, less than 10% of the release events occur in multiple steps. At a tenfold higher motor concentration, a significant increase in multiple release events can be observed. To rule out non-specific interactions, confirm that no events are detectable in the absence of motor.
2. Use the Schwartz information criterion step-finding algorithm[136] to determine release events that occur between ± 150 nm dwell locations of the beads.
3. Visually confirm that the release of a bead from the MT is a single step process, making sure that a single motor was bound to MT. The bead rapidly snaps back to the trap center after the release of the motor from MT.
4. Discard the multiple release events in one period of oscillation, which correspond to the release of multiple motors from MT. 90% of the binding events terminated with a single release step, indicative of binding of a single kinesin monomer.
5. Discard events in which the bead is stalled at a position different than the trap center In these cases, release forces are overestimated because the exerted force is shared between two monomers and dwell time is not clear for each monomer.
6. Discard MT dwell times shorter than 1 ms. Shorter dwells are discarded because the corner frequency of the bead (~ 700-800 Hz) limits the measurement of faster events.
7. Calculate the magnitude of the force exerted on a motor during binding by multiplying the trap stiffness and the bead-trap separation.
8. Determine the force direction from the bead-trap separation vector. Assign positive and negative signs for forces directed toward the MT plus and minus ends, respectively.

9. Sort the MT dwell-time data by applied force and bin under different forces for equal number of data points. Assign the average force for each bin. Because the method has no bias toward detecting release events under low or high forces, the distribution of release events is nearly uniform over a wide range of forces. This enables the determination of the force-dependent release profile of a motor for each nucleotide and pulling condition in a single experiment without adjusting the parameters of the trapping assay.

10. Plot the cumulative distribution of the each binned data set. Cumulative distribution functions are built to eliminate the bias on the rates when different bin sizes are used for making histograms.

11. Fit the resulting cumulative distributions to an exponential decay in MATLAB. Resulting decay constants were assigned as the force-dependent release rate of kinesin monomers. It is crucial to run an F-test to verify whether the addition of a second exponential is statistically justified. Two distinct release rates under the same force regime may result from strong and weak binding modes of a motor to MT.

12. Plot the release rate as a function of the average force in the bin.

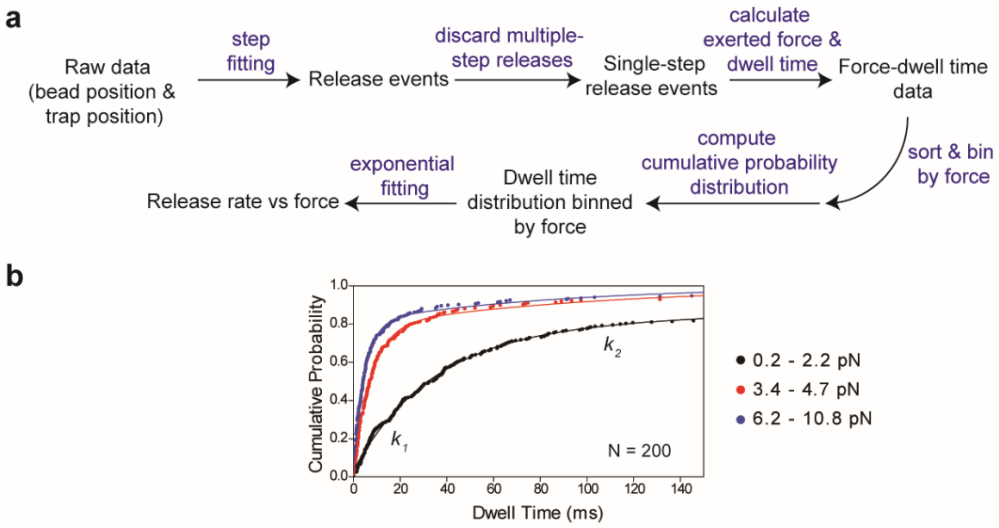

Figure 30: Data analysis for force-dependent release rate measurements (a) *Graphical overview of the data analysis routine for force-dependent directional release of kinesin monomers.* ***(b)*** *Cumulative probability distributions (solid circles) represent the dwell time data for kinesin monomers pulled on the head toward the plus-end in the absence of nucleotide at different force ranges; n = 200 for each histogram. The release rates (k_1 and k_2) at a given force range were calculated by a two-exponential-decay fit (solid curves).* ***(c)*** *MT release rates of head- and NL-pulled kinesins under 1 mM ADP. The kinesin release rate increases with increasing force in both directions. The release of NL-pulled kinesins was slower than head-pulled kinesins under backward forces. Error bars represent 95% confidence intervals.*

Tables

	Dyn - 0 mM KAc	Dyn - 50 mM KAc	$Dyn_{RK+7hep}$ - 50 mM KAc	$Dyn_{RK+7hep}$ - 150 mM KAc
k_{cat} (s^{-1} per head)	7.3 ± 0.1	7.9 ± 0.1	6.8 ± 0.2	8.5 ± 0.2
k_{basal} (s^{-1} per head)	1.1 ± 0.1	2.4 ± 0.1	4.6 ± 0.6	6.6 ± 0.3
K_M (nM)	19 ± 3.4	630 ± 65	19 ± 5.1	75 ± 4.3
+ Runs (nm/s)	N.A.	N.A.	18.2 ± 10.9	23.9 ± 13.8
- Runs (nm/s)	88.2 ± 30.2	95.5 ± 51.5	10.6 ± 3.6	-33.3 ± 11.1
+ Runs (%)	0	0	81	83
- Runs (%)	100	100	8	6
Diffusive (%)	0	0	10	11

Table 1: MT stimulated ATPase activity and velocity analysis of Dyn and $Dyn_{RK+7hep}$ under different salt conditions*. An increase in salt concentration reduces the MT affinity (K_{M-MT}) of Dyn and $Dyn_{RK+7hep}$, but it does not alter their directionality. K_{M-MT} of Dyn without added salt is similar to that of $Dyn_{RK+7hep}$ under 50 mM KAc (p >0.05, t-test). ATPase data was collected from three independent experiments (mean ± s.d.). n is larger than 50 molecules for single molecule motility assays.*

References

1. Schliwa, M. Myosin steps backwards. *Nature* **401**, 431-432 (1999).
2. Wells, A.L. *et al.* Myosin VI is an actin-based motor that moves backwards. *Nature* **401**, 505-508 (1999).
3. Vale, R.D., Reese, T.S. & Sheetz, M.P. Identification of a novel force-generating protein, kinesin, involved in microtubule-based motility. *Cell* **42**, 39-50 (1985).
4. Brady, S.T. A novel brain ATPase with properties expected for the fast axonal transport motor. *Nature* **317**, 73-75 (1985).
5. Hirokawa, N., Noda, Y., Tanaka, Y. & Niwa, S. Kinesin superfamily motor proteins and intracellular transport. *Nature reviews. Molecular cell biology* **10**, 682-696 (2009).
6. Yamada, M., Tanaka-Takiguchi, Y., Hayashi, M., Nishina, M. & Goshima, G. Multiple kinesin-14 family members drive microtubule minus end-directed transport in plant cells. *J Cell Biol* **216**, 1705-1714 (2017).
7. Paschal, B.M. *et al.* Isolated flagellar outer arm dynein translocates brain microtubules in vitro. *Nature* **330**, 672-674 (1987).
8. Roberts, A.J., Kon, T., Knight, P.J., Sutoh, K. & Burgess, S.A. Functions and mechanics of dynein motor proteins. *Nat Rev Mol Cell Biol* **14**, 713-726 (2013).
9. Driskell, O.J., Mironov, A., Allan, V.J. & Woodman, P.G. Dynein is required for receptor sorting and the morphogenesis of early endosomes. *Nat Cell Biol* **9**, 113-120 (2007).
10. Jordens, I. *et al.* The Rab7 effector protein RILP controls lysosomal transport by inducing the recruitment of dynein-dynactin motors. *Curr Biol* **11**, 1680-1685 (2001).
11. Blocker, A. *et al.* Molecular requirements for bi-directional movement of phagosomes along microtubules. *J Cell Biol* **137**, 113-129 (1997).
12. Gross, S.P. *et al.* Interactions and regulation of molecular motors in Xenopus melanophores. *J Cell Biol* **156**, 855-865 (2002).
13. Kural, C. *et al.* Kinesin and dynein move a peroxisome in vivo: a tug-of-war or coordinated movement? *Science* **308**, 1469-1472 (2005).
14. Gross, S.P., Welte, M.A., Block, S.M. & Wieschaus, E.F. Dynein-mediated cargo transport in vivo. A switch controls travel distance. *J Cell Biol* **148**, 945-956 (2000).
15. Pilling, A.D., Horiuchi, D., Lively, C.M. & Saxton, W.M. Kinesin-1 and Dynein are the primary motors for fast transport of mitochondria in Drosophila motor axons. *Mol Biol Cell* **17**, 2057-2068 (2006).
16. Presley, J.F. *et al.* ER-to-Golgi transport visualized in living cells. *Nature* **389**, 81-85 (1997).
17. Dodding, M.P. & Way, M. Coupling viruses to dynein and kinesin-1. *The EMBO journal* **30**, 3527-3539 (2011).
18. Harrell, J.M. *et al.* Evidence for glucocorticoid receptor transport on microtubules by dynein. *The Journal of biological chemistry* **279**, 54647-54654 (2004).
19. Johnston, J.A., Illing, M.E. & Kopito, R.R. Cytoplasmic dynein/dynactin mediates the assembly of aggresomes. *Cell motility and the cytoskeleton* **53**, 26-38 (2002).
20. Bullock, S.L., Nicol, A., Gross, S.P. & Zicha, D. Guidance of bidirectional motor complexes by mRNA cargoes through control of dynein number and activity. *Current biology : CB* **16**, 1447-1452 (2006).
21. Sasaki, S. *et al.* A LIS1/NUDEL/cytoplasmic dynein heavy chain complex in the developing and adult nervous system. *Neuron* **28**, 681-696 (2000).
22. Barakat-Walter, I. & Riederer, B.M. Triiodothyronine and nerve growth factor are required to induce cytoplasmic dynein expression in rat dorsal root ganglion cultures. *Brain Res Dev Brain Res* **96**, 109-119 (1996).

23. Cheng, H.H. *et al.* Heavy chain of cytoplasmic dynein is a major component of the postsynaptic density fraction. *J Neurosci Res* **84**, 244-254 (2006).
24. Schnapp, B.J. & Reese, T.S. Dynein is the motor for retrograde axonal transport of organelles. *Proceedings of the National Academy of Sciences of the United States of America* **86**, 1548-1552 (1989).
25. Hafezparast, M. *et al.* Mutations in dynein link motor neuron degeneration to defects in retrograde transport. *Science* **300**, 808-812 (2003).
26. El-Kadi, A.M., Soura, V. & Hafezparast, M. Defective axonal transport in motor neuron disease. *J Neurosci Res* **85**, 2557-2566 (2007).
27. Ligon, L.A., Tokito, M., Finklestein, J.M., Grossman, F.E. & Holzbaur, E.L. A direct interaction between cytoplasmic dynein and kinesin I may coordinate motor activity. *The Journal of biological chemistry* **279**, 19201-19208 (2004).
28. Gerdes, J.M. & Katsanis, N. Microtubule transport defects in neurological and ciliary disease. *Cell Mol Life Sci* **62**, 1556-1570 (2005).
29. Busson, S., Dujardin, D., Moreau, A., Dompierre, J. & De Mey, J.R. Dynein and dynactin are localized to astral microtubules and at cortical sites in mitotic epithelial cells. *Current biology : CB* **8**, 541-544 (1998).
30. Sharp, D.J., Rogers, G.C. & Scholey, J.M. Microtubule motors in mitosis. *Nature* **407**, 41-47 (2000).
31. Gaetz, J. & Kapoor, T.M. Dynein/dynactin regulate metaphase spindle length by targeting depolymerizing activities to spindle poles. *J Cell Biol* **166**, 465-471 (2004).
32. Tanenbaum, M.E., Macurek, L., Galjart, N. & Medema, R.H. Dynein, Lis1 and CLIP-170 counteract Eg5-dependent centrosome separation during bipolar spindle assembly. *The EMBO journal* **27**, 3235-3245 (2008).
33. Elting, M.W., Hueschen, C.L., Udy, D.B. & Dumont, S. Force on spindle microtubule minus ends moves chromosomes. *J Cell Biol* **206**, 245-256 (2014).
34. Heald, R. *et al.* Self-organization of microtubules into bipolar spindles around artificial chromosomes in Xenopus egg extracts. *Nature* **382**, 420-425 (1996).
35. Merdes, A., Heald, R., Samejima, K., Earnshaw, W.C. & Cleveland, D.W. Formation of spindle poles by dynein/dynactin-dependent transport of NuMA. *J Cell Biol* **149**, 851-862 (2000).
36. Quintyne, N.J., Reing, J.E., Hoffelder, D.R., Gollin, S.M. & Saunders, W.S. Spindle multipolarity is prevented by centrosomal clustering. *Science* **307**, 127-129 (2005).
37. Howell, B.J. *et al.* Cytoplasmic dynein/dynactin drives kinetochore protein transport to the spindle poles and has a role in mitotic spindle checkpoint inactivation. *J Cell Biol* **155**, 1159-1172 (2001).
38. Wojcik, E. *et al.* Kinetochore dynein: its dynamics and role in the transport of the Rough deal checkpoint protein. *Nature cell biology* **3**, 1001-1007 (2001).
39. Perrone, C.A. *et al.* A novel dynein light intermediate chain colocalizes with the retrograde motor for intraflagellar transport at sites of axoneme assembly in chlamydomonas and Mammalian cells. *Molecular biology of the cell* **14**, 2041-2056 (2003).
40. Kon, T., Nishiura, M., Ohkura, R., Toyoshima, Y.Y. & Sutoh, K. Distinct functions of nucleotide-binding/hydrolysis sites in the four AAA modules of cytoplasmic dynein. *Biochemistry* **43**, 11266-11274 (2004).
41. Cho, C., Reck-Peterson, S.L. & Vale, R.D. Regulatory ATPase sites of cytoplasmic dynein affect processivity and force generation. *The Journal of biological chemistry* **283**, 25839-25845 (2008).
42. DeWitt, M.A., Cypranowska, C.A., Cleary, F.B., Belyy, V. & Yildiz, A. The AAA3 domain of cytoplasmic dynein acts as a switch to facilitate microtubule release. *Nat Struct Mol Biol* **22**, 73-80 (2015).
43. Bhabha, G. *et al.* Allosteric communication in the dynein motor domain. *Cell* **159**, 857-868 (2014).

44. Nicholas, M.P. *et al.* Control of cytoplasmic dynein force production and processivity by its C-terminal domain. *Nature communications* **6**, 6206 (2015).
45. Carter, A.P., Cho, C., Jin, L. & Vale, R.D. Crystal structure of the dynein motor domain. *Science* **331**, 1159-1165 (2011).
46. Kon, T. *et al.* The 2.8 A crystal structure of the dynein motor domain. *Nature* **484**, 345-350 (2012).
47. Schmidt, H., Gleave, E.S. & Carter, A.P. Insights into dynein motor domain function from a 3.3-A crystal structure. *Nat Struct Mol Biol* **19**, 492-497, S491 (2012).
48. Vallee, R.B., Williams, J.C., Varma, D. & Barnhart, L.E. Dynein: An ancient motor protein involved in multiple modes of transport. *J Neurobiol* **58**, 189-200 (2004).
49. Bingham, J.B., King, S.J. & Schroer, T.A. Purification of dynactin and dynein from brain tissue. *Methods in enzymology* **298**, 171-184 (1998).
50. Burgess, S.A., Walker, M.L., Sakakibara, H., Knight, P.J. & Oiwa, K. Dynein structure and power stroke. *Nature* **421**, 715-718 (2003).
51. Kon, T. *et al.* Helix sliding in the stalk coiled coil of dynein couples ATPase and microtubule binding. *Nat Struct Mol Biol* **16**, 325-333 (2009).
52. Roberts, A.J. *et al.* AAA+ Ring and linker swing mechanism in the dynein motor. *Cell* **136**, 485-495 (2009).
53. Schmidt, H., Zalyte, R., Urnavicius, L. & Carter, A.P. Structure of human cytoplasmic dynein-2 primed for its power stroke. *Nature* **518**, 435-438 (2015).
54. Block, S.M. Kinesin motor mechanics: binding, stepping, tracking, gating, and limping. *Biophys J* **92**, 2986-2995 (2007).
55. Spudich, J.A. Molecular motors take tension in stride. *Cell* **126**, 242-244 (2006).
56. Altman, D., Sweeney, H.L. & Spudich, J.A. The mechanism of myosin VI translocation and its load-induced anchoring. *Cell* **116**, 737-749 (2004).
57. Guydosh, N.R. & Block, S.M. Backsteps induced by nucleotide analogs suggest the front head of kinesin is gated by strain. *Proc Natl Acad Sci U S A* **103**, 8054-8059 (2006).
58. Bryant, Z., Altman, D. & Spudich, J.A. The power stroke of myosin VI and the basis of reverse directionality. *Proceedings of the National Academy of Sciences of the United States of America* **104**, 772-777 (2007).
59. Yildiz, A., Tomishige, M., Gennerich, A. & Vale, R.D. Intramolecular strain coordinates kinesin stepping behavior along microtubules. *Cell* **134**, 1030-1041 (2008).
60. Mehta, A. Myosin learns to walk. *Journal of cell science* **114**, 1981-1998. (2001).
61. Yildiz, A. GE Prize winner. How molecular motors move. *Science* **311**, 792-793 (2006).
62. DeWitt, M.A., Chang, A.Y., Combs, P.A. & Yildiz, A. Cytoplasmic dynein moves through uncoordinated stepping of the AAA+ ring domains. *Science* **335**, 221-225 (2012).
63. Qiu, W. *et al.* Dynein achieves processive motion using both stochastic and coordinated stepping. *Nat Struct Mol Biol* **19**, 193-200 (2012).
64. Reck-Peterson, S.L. *et al.* Single-molecule analysis of dynein processivity and stepping behavior. *Cell* **126**, 335-348 (2006).
65. Belyy, V., Hendel, N.L., Chien, A. & Yildiz, A. Cytoplasmic dynein transports cargos via load-sharing between the heads. *Nature communications* **5**, 5544 (2014).
66. Gennerich, A., Carter, A.P., Reck-Peterson, S.L. & Vale, R.D. Force-induced bidirectional stepping of cytoplasmic dynein. *Cell* **131**, 952-965 (2007).
67. Svoboda, K. & Block, S.M. Force and velocity measured for single kinesin molecules. *Cell* **77**, 773-784 (1994).
68. Belyy, V. *et al.* The mammalian dynein-dynactin complex is a strong opponent to kinesin in a tug-of-war competition. *Nat Cell Biol* **18**, 1018-1024 (2016).
69. Gebhardt, J.C., Clemen, A.E., Jaud, J. & Rief, M. Myosin-V is a mechanical ratchet. *Proc Natl Acad Sci U S A* **103**, 8680-8685 (2006).

70. Guydosh, N.R. & Block, S.M. Direct observation of the binding state of the kinesin head to the microtubule. *Nature* **461**, 125-128 (2009).
71. Nicastro, D. *et al.* The molecular architecture of axonemes revealed by cryoelectron tomography. *Science* **313**, 944-948 (2006).
72. Carter, A.P. *et al.* Structure and functional role of dynein's microtubule-binding domain. *Science* **322**, 1691-1695 (2008).
73. Cleary, F.B. *et al.* Tension on the linker gates the ATP-dependent release of dynein from microtubules. *Nature communications* **5**, 4587 (2014).
74. Nicholas, M.P. *et al.* Cytoplasmic dynein regulates its attachment to microtubules via nucleotide state-switched mechanosensing at multiple AAA domains. *Proc Natl Acad Sci U S A* **112**, 6371-6376 (2015).
75. Furuta, A. *et al.* Creating biomolecular motors based on dynein and actin-binding proteins. *Nat Nanotechnol* **12**, 233-237 (2017).
76. Vale, R.D. & Toyoshima, Y.Y. Rotation and translocation of microtubules in vitro induced by dyneins from Tetrahymena cilia. *Cell* **52**, 459-469 (1988).
77. Nishizaka, T., Yagi, T., Tanaka, Y. & Ishiwata, S. Right-handed rotation of an actin filament in an in vitro motile system. *Nature* **361**, 269-271 (1993).
78. Yajima, J., Mizutani, K. & Nishizaka, T. A torque component present in mitotic kinesin Eg5 revealed by three-dimensional tracking. *Nat Struct Mol Biol* **15**, 1119-1121 (2008).
79. Nitzsche, B., Ruhnow, F. & Diez, S. Quantum-dot-assisted characterization of microtubule rotations during cargo transport. *Nat Nanotechnol* **3**, 552-556 (2008).
80. Brunnbauer, M. *et al.* Torque generation of kinesin motors is governed by the stability of the neck domain. *Molecular cell* **46**, 147-158 (2012).
81. Bormuth, V. *et al.* The highly processive kinesin-8, Kip3, switches microtubule protofilaments with a bias toward the left. *Biophysical journal* **103**, L4-6 (2012).
82. Roberts, A.J., Kon, T., Knight, P.J., Sutoh, K. & Burgess, S.A. Functions and mechanics of dynein motor proteins. *Nat Rev Mol Cell Biol* (2013).
83. Ray, S., Meyhofer, E., Milligan, R.A. & Howard, J. Kinesin follows the microtubule's protofilament axis. *J Cell Biol* **121**, 1083-1093 (1993).
84. Yajima, J. & Cross, R.A. A torque component in the kinesin-1 power stroke. *Nature chemical biology* **1**, 338-341 (2005).
85. Gibbons, I.R. *et al.* The affinity of the dynein microtubule-binding domain is modulated by the conformation of its coiled-coil stalk. *J Biol Chem* **280**, 23960-23965 (2005).
86. Hyman, A.A., Chretien, D., Arnal, I. & Wade, R.H. Structural changes accompanying GTP hydrolysis in microtubules: information from a slowly hydrolyzable analogue guanylyl-(alpha,beta)-methylene-diphosphonate. *J Cell Biol* **128**, 117-125 (1995).
87. Nitzsche, B. *et al.* Studying kinesin motors by optical 3D-nanometry in gliding motility assays. *Methods in cell biology* **95**, 247-271 (2010).
88. Kamei, T., Kakuta, S. & Higuchi, H. Biased binding of single molecules and continuous movement of multiple molecules of truncated single-headed kinesin. *Biophys J* **88**, 2068-2077 (2005).
89. Furuta, K. *et al.* Measuring collective transport by defined numbers of processive and nonprocessive kinesin motors. *Proceedings of the National Academy of Sciences of the United States of America* **110**, 501-506 (2013).
90. Stamer, K., Vogel, R., Thies, E., Mandelkow, E. & Mandelkow, E.M. Tau blocks traffic of organelles, neurofilaments, and APP vesicles in neurons and enhances oxidative stress. *J Cell Biol* **156**, 1051-1063 (2002).
91. Dixit, R., Ross, J.L., Goldman, Y.E. & Holzbaur, E.L. Differential Regulation of Dynein and Kinesin Motor Proteins by Tau. *Science* (2008).
92. Aitken, C.E., Marshall, R.A. & Puglisi, J.D. An oxygen scavenging system for improvement of dye stability in single-molecule fluorescence experiments. *Biophys J* **94**, 1826-1835 (2008).

93. Homma, K., Yoshimura, M., Saito, J., Ikebe, R. & Ikebe, M. The core of the motor domain determines the direction of myosin movement. *Nature* **412**, 831-834 (2001).
94. Sablin, E.P. *et al.* Direction determination in the minus-end-directed kinesin motor ncd. *Nature* **395**, 813-816 (1998).
95. Dyneins, Dynein Mechanics, Dysfunction, and Disease, Vol. 2, Edn. 2. (ed. S.M. King) 215-474 (Academic Press, 2017).
96. Gee, M.A., Heuser, J.E. & Vallee, R.B. An extended microtubule-binding structure within the dynein motor domain. *Nature* **390**, 636-639 (1997).
97. Lin, J., Okada, K., Raytchev, M., Smith, M.C. & Nicastro, D. Structural mechanism of the dynein power stroke. *Nature cell biology* **16**, 479-485 (2014).
98. Imai, H. *et al.* Direct observation shows superposition and large scale flexibility within cytoplasmic dynein motors moving along microtubules. *Nat Commun* **6**, 8179 (2015).
99. Lippert, L.G. *et al.* Angular measurements of the dynein ring reveal a stepping mechanism dependent on a flexible stalk. *Proc Natl Acad Sci U S A* **114**, E4564-E4573 (2017).
100. Can, S., Dewitt, M.A. & Yildiz, A. Bidirectional helical motility of cytoplasmic dynein around microtubules. *Elife* **3**, e03205 (2014).
101. Redwine, W.B. *et al.* Structural basis for microtubule binding and release by dynein. *Science* **337**, 1532-1536 (2012).
102. Alushin, G.M. *et al.* High-resolution microtubule structures reveal the structural transitions in alphabeta-tubulin upon GTP hydrolysis. *Cell* **157**, 1117-1129 (2014).
103. Kellogg, E.H. *et al.* Insights into the Distinct Mechanisms of Action of Taxane and Non-Taxane Microtubule Stabilizers from Cryo-EM Structures. *J Mol Biol* **429**, 633-646 (2017).
104. Niekamp, S., Coudray, N., Zhang, N., Vale, R.D. & Bhabha, G. Stalk-mediated communication in the dynein motor domain. *bioRxiv* (2018).
105. Chretien, D., Kenney, J.M., Fuller, S.D. & Wade, R.H. Determination of microtubule polarity by cryo-electron microscopy. *Structure* **4**, 1031-1040 (1996).
106. Gell, C. *et al.* Purification of tubulin from porcine brain. *Methods Mol Biol* **777**, 15-28 (2011).
107. Yildiz, A. *et al.* Myosin V walks hand-over-hand: single fluorophore imaging with 1.5-nm localization. *Science* **300**, 2061-2065 (2003).
108. Neuman, K.C. & Block, S.M. Optical trapping. *Rev Sci Instrum* **75**, 2787-2809 (2004).
109. Dogan, M.Y., Can, S., Cleary, F.B., Purde, V. & Yildiz, A. Kinesin's front head is gated by the backward orientation of its neck linker. *Cell Rep* **10**, 1967-1973 (2015).
110. Phillips, J.C. *et al.* Scalable molecular dynamics with NAMD. *Journal of computational chemistry* **26**, 1781-1802 (2005).
111. Best, R.B. *et al.* Optimization of the additive CHARMM all-atom protein force field targeting improved sampling of the backbone ϕ, ψ and side-chain $\chi 1$ and $\chi 2$ dihedral angles. *Journal of chemical theory and computation* **8**, 3257-3273 (2012).
112. Belyy, V. & Yildiz, A. Processive cytoskeletal motors studied with single-molecule fluorescence techniques. *FEBS Lett* **588**, 3520-3525 (2014).
113. Hua, W., Young, E.C., Fleming, M.L. & Gelles, J. Coupling of kinesin steps to ATP hydrolysis. *Nature* **388**, 390-393 (1997).
114. Schnitzer, M.J. & Block, S.M. Kinesin hydrolyses one ATP per 8-nm step. *Nature* **388**, 386-390 (1997).
115. Shastry, S. & Hancock, W.O. Neck linker length determines the degree of processivity in kinesin-1 and kinesin-2 motors. *Curr Biol* **20**, 939-943 (2010).
116. Clancy, B.E., Behnke-Parks, W.M., Andreasson, J.O., Rosenfeld, S.S. & Block, S.M. A universal pathway for kinesin stepping. *Nature structural & molecular biology* **18**, 1020-1027 (2011).
117. Rosenfeld, S.S., Jefferson, G.M. & King, P.H. ATP reorients the neck linker of kinesin in two sequential steps. *J Biol Chem* **276**, 40167-40174 (2001).

118. Hyeon, C. & Onuchic, J.N. Internal strain regulates the nucleotide binding site of the kinesin leading head. *Proceedings of the National Academy of Sciences of the United States of America* **104**, 2175-2180 (2007).
119. Dudko, O.K., Hummer, G. & Szabo, A. Theory, analysis, and interpretation of single-molecule force spectroscopy experiments. *Proc Natl Acad Sci U S A* **105**, 15755-15760 (2008).
120. Capitanio, M. *et al.* Ultrafast force-clamp spectroscopy of single molecules reveals load dependence of myosin working stroke. *Nat Methods* **9**, 1013-1019 (2012).
121. Tomishige, M., Stuurman, N. & Vale, R.D. Single-molecule observations of neck linker conformational changes in the kinesin motor protein. *Nature structural & molecular biology* **13**, 887-894 (2006).
122. Kawaguchi, K. & Ishiwata, S. Nucleotide-dependent single- to double-headed binding of kinesin. *Science* **291**, 667-669. (2001).
123. Uemura, S. *et al.* Kinesin-microtubule binding depends on both nucleotide state and loading direction. *Proceedings of the National Academy of Sciences of the United States of America* **99**, 5977-5981 (2002).
124. Hancock, W.O. & Howard, J. Kinesin's processivity results from mechanical and chemical coordination between the ATP hydrolysis cycles of the two motor domains. *Proceedings of the National Academy of Sciences of the United States of America* **96**, 13147-13152 (1999).
125. Hackney, D.D. The rate-limiting step in microtubule-stimulated ATP hydrolysis by dimeric kinesin head domains occurs while bound to the microtubule. *The Journal of biological chemistry* **269**, 16508-16511 (1994).
126. Uemura, S. & Ishiwata, S. Loading direction regulates the affinity of ADP for kinesin. *Nature structural biology* **10**, 308-311 (2003).
127. Toprak, E., Yildiz, A., Hoffman, M.T., Rosenfeld, S.S. & Selvin, P.R. Why kinesin is so processive. *Proceedings of the National Academy of Sciences of the United States of America* **106**, 12717-12722 (2009).
128. Milic, B., Andreasson, J.O., Hancock, W.O. & Block, S.M. Kinesin processivity is gated by phosphate release. *Proc Natl Acad Sci U S A* (2014).
129. Ma, Y.Z. & Taylor, E.W. Interacting head mechanism of microtubule-kinesin ATPase. *The Journal of biological chemistry* **272**, 724-730 (1997).
130. Rice, S. *et al.* A structural change in the kinesin motor protein that drives motility. *Nature* **402**, 778-784 (1999).
131. Kikkawa, M. *et al.* Switch-based mechanism of kinesin motors. *Nature* **411**, 439-445 (2001).
132. Sindelar, C.V. & Downing, K.H. An atomic-level mechanism for activation of the kinesin molecular motors. *Proceedings of the National Academy of Sciences of the United States of America* **107**, 4111-4116 (2010).
133. Sindelar, C.V. A seesaw model for intermolecular gating in the kinesin motor protein. *Biophysical reviews* **3**, 85-100 (2011).
134. Dunn, A.R., Chuan, P., Bryant, Z. & Spudich, J.A. Contribution of the myosin VI tail domain to processive stepping and intramolecular tension sensing. *Proceedings of the National Academy of Sciences of the United States of America* **107**, 7746-7750 (2010).
135. Schmidt, H., Gleave, E.S. & Carter, A.P. Insights into dynein motor domain function from a 3.3-A crystal structure. *Nat Struct Mol Biol* (2012).
136. Behrendt, F.F. *et al.* Introduction of a dedicated circulation phantom for comprehensive in vitro analysis of intravascular contrast material application. *Invest Radiol* **43**, 729-736 (2008).